Flocking Modeling, Control, and Optimization of Connected and Automated

Vehicles for Safe and Efficient Mobility

by

Fengchen Wang

A Dissertation Presented in Partial Fulfillment
of the Requirements for the Degree
Doctor of Philosophy

Approved April 2020 by the
Graduate Supervisory Committee:

Yan Chen, Chair
Changho Nam
Wenlong Zhang

ARIZONA STATE UNIVERSITY

May 2020

ABSTRACT

In large modern urban areas, traffic congestion and fatality have become two serious problems. To improve the safety and efficiency of ground mobility, one promising solution is the cooperative control of connected and automated vehicle (CAV) systems, which can avoid human drivers' incapability and errors. Taking advantage of two-dimensional (2D) vehicular control, this dissertation intends to conduct a thorough investigation of the modeling, control, and optimization of CAV systems with flocking control. Flocking is a dynamic swarm congregating behavior of a group of agents with self-organizing features, and flocking control of CAV systems attempts to achieve the maintenance of a small and nearly constant distance among vehicles, speed match, destination cohesion, and collision and obstacle avoidance.

Concerning artificial multi-agent systems, such as mobile robots and CAV systems, a set of engineering performance requirements should be considered in flocking theory for practical applications. In this dissertation, three novel flocking control protocols are studied, which consider convergence speed, permanent obstacle avoidance, and energy efficiency. Furthermore, considering nonlinear vehicle dynamics, a novel hierarchical flocking control framework is proposed for CAV systems to integrate high-level flocking coordination planning and low-level vehicle dynamics control together. On one hand, using 2D flocking theory, the decision making and motion planning of engaged vehicles are produced in a distributed manner based on shared information. On the other hand, using the proposed framework, many advanced vehicle dynamics control methods and tools are applicable. For instance, in the low-level vehicle dynamics control, in addition to path trajectory tracking, the maintenance of vehicle later/yaw stability and rollover propensity mitigation are achieved by using additional actuators, such

as all-wheel driving and four-wheel steering, to enhance vehicle safety and efficiency with over-actuated features.

Co-simulations using MATLAB/Simulink® and CarSim® are conducted to illustrate the performances of the proposed flocking framework and all controller designs proposed in this dissertation. Moreover, a scaled CAV system is developed, and field experiments are also completed to further demonstrate the feasibility of the proposed flocking framework. Consequently, the proposed flocking framework can successfully complete a 2D vehicular flocking coordination. The novel flocking control protocols are also able to accommodate the practical requirements of artificial multi-agent systems by enhancing convergence speed, saving energy consumption, and avoiding permanent obstacles. In addition, employing the proposed control methods, vehicle stability is guaranteed as expected.

To my mother, Xiaoqin, who loved me

ACKNOWLEDGMENTS

TABLE OF CONTENTS

LIST OF TABLES

LIST OF FIGURES

xiv

α_f Vehicle front tire sideslip angle

α_r Vehicle rear tire sideslip angle

β Vehicle sideslip angle

δ_f Vehicle front steering angle

δ_r Vehicle rear steering angle

ϕ Vehicle roll angle

ψ Vehicle heading angle

CG   Vehicle center of gravity

F_{cx} Vehicle corrective longitudinal force

F_{cy} Vehicle corrective lateral force

F_{re} Vehicle resistance force

F_{xf} Vehicle front longitudinal tire force

F_{xr} Vehicle rear longitudinal tire force

F_{yf} Vehicle front lateral tire force

F_{yr} Vehicle rear lateral tire force

I_z Moment of inertia of vehicle with respect to z-axis

L_f Distance from the CG to vehicle front wheel center

L_r Distance from the CG to vehicle rear wheel center

l_s Vehicle wheel track

M Vehicle mass

M_z Vehicle corrective yaw moment

r Vehicle yaw rate

V Vehicle global velocity

v_x Longitudinal vehicle speed

v_y Lateral vehicle speed

v_f Vehicle front wheel moving velocity

v_r Vehicle rear wheel moving velocity

Chapter 1

INTRODUCTION

1.1 Motivation: Why Connected and Automated Vehicle Systems?

In large modern urban areas, traffic congestion and fatality have become two serious problems. Statistically, in 2017, traffic jams resulted in 8.8 billion hours of delayed person-hours and $179 billion economic loss in the U.S., which is estimated to increase to $237 billion by 2025 (Schrank, Eisele, and Lomax 2019). Moreover, based on the data obtained from the World Health Organization, traffic accidents caused 1.35 million death worldwide in 2016, whilst it has become the eighth leading cause of death for people of all ages (World Health Organization 2018). In the U.S., the increase in traffic fatalities in 2016, 6%, even reached the highest point in nearly five decades (NHTSA's National Center for Statistics and Analysis 2016). One notable reason for those unexpected problems is that car drivers may not be able to give appropriate commands to avoid traffic congestion or fatality because of human's inattention and incapability to timely observe, predict, and react. It is also reported that 94% of car crashes in the US are due to human errors. Therefore, researchers and engineers propose connected and automated vehicle (CAV) systems as a new promising solution to tackle urban transportation problems by excluding human errors.

Before diving deep into the concept of CAV systems, I would like to define several terminologies used throughout this dissertation.

Autonomous driving technology: the technology drives vehicles only based on perception information and vehicle states acquired from onboard sensors without communication with other vehicles or infrastructures.

Automated vehicle: the vehicle uses mechatronics actuators and autonomous driving technologies to replace human driving.

Connected vehicles: the vehicles are connected together through wireless communication networks to share information.

Using the aforementioned terminologies, the CAV systems in this dissertation refer to a group of automated vehicles that are connected together for cooperative control purposes. Especially, the CAV systems can be explored in the context of vehicular cyber-physical systems (CPS). A general CPS, as a new generation embedded system, integrates a collection of real-time decision making, networking, and physical processing in a feedback loop (Lee 2008; Alur 2015; Lee and Seshia 2016). Specifically, the vehicular CPS is composed of multiple automated vehicles and vehicular wireless communication networks.

The autonomous driving technology is employed as the physical-processing and decision-making layers of vehicular CPS, which enables the autonomy of individual vehicles. On the one hand, the development of vehicle electrification including drive-by-wire technologies paves the way for autonomous driving, which uses electrified actuators to generate control efforts. In other words, the conventional mechanical control systems, such as pedals, steering columns, pumps, and belts, are substituted by electronic control systems. As a result, the drive-by-wire technologies make it possible to drive vehicles using electronic signals, instead of manipulating the mechanical control systems with human intervention. Besides, the drive-by-wire systems also inspire over-actuated vehicle controls, which provides extra control degrees of freedom to maintain

2

vehicle stability and save energy. On the other hand, powered by the advancement of onboard sensing, data processing, and real-time decision making, various autonomous driving control algorithms for individual vehicles have been prevalently investigated, such as lane-keeping control, pedestrians and obstacles detection, trajectory-tracking control, and adaptive cruise control (ACC) (Martínez-García, Zhang, and Gordon 2016; Sivaraman and Trivedi 2013; Desjardins and Chaib-Draa 2011; Potsaid et al. 2007). A notable success instance of individually autonomous driving was the winner, "Tartan Racing" team, led by Carnegie Mellon University, in the 2007 DARPA Urban Challenge (Darms et al. 2009). Moreover, Waymo LLC. has recently launched to test their fully self-driving cars on public roads in Arizona without a human backup driver, which could be considered as the first Level 4 automated driving car defined by the Society of Automobile Engineers on public roads in the world (Jones 2017).

While the individual automated vehicles are expected to handle most of the complex traffic scenarios, some inherent drawbacks appear. First, the onboard sensors of automated vehicles usually have inherent measurement delays, and it is also time-consuming to observe or estimate states of other vehicles. The time delays in perception not only significantly influence the real-time construction of vehicle surroundings but also jeopardize autonomous driving safety. Second, in some particular situations, the ranging sensors, such as radars, of individual automated vehicles sometimes fail to detect obstacles or other vehicles. For example, a vehicle cannot measure the inter-vehicle gap to its preceding vehicle during cornering as well as the states of the preceding vehicle. Such information absence of other vehicles may result in unexpected safety issues as well. Finally, the cooperative control among a group of automated vehicles is anticipated in intelligent transportation systems to improve safety and traffic capacity, whose objectives include the maintenance of a small and nearly

constant distance among vehicles, speed match, destination cohesion, and collision and obstacle avoidance. However, individual automated vehicles cannot complete those cooperative tasks with the absence of information sharing. Therefore, the vehicular wireless network is required as the communication layer of a vehicular CPS to connect individual automated vehicles together, so-called CAV systems.

Using vehicular wireless communication, the vehicle states and other perception information can be directly acquired without the limitations of sensor delays and state observation/estimation, whilst the perception capability of onboard sensors are also compensated without driving scenario limitations. In addition, the cooperative control can also be achieved based on the shared information and control protocol design. To sum up, the CAV systems have great potential to resolve traffic congestion and fatality issues benefited by vehicle autonomy and vehicular communication.

1.2 Literature Review

1.2.1 Cooperative Control in CAV Systems

Back in the late 1980s, research on the cooperative control of multi-vehicle systems was investigated to achieve consensus phenomena via centralized or distributed control protocols, which referred to dynamical coordination of a group of CAVs connected by wireless communication (Chen and Cheng 2010; Murray 2007; Cao et al. 2012). Benefited from the shared information and coordinated behaviors, the cooperative control of CAV systems has broad engineering applications in transportation systems, military systems, mobile sensor networks, robotic systems, and testbeds (Murray 2007). Recently, with the advancement of vehicular wireless communication, onboard

sensing and data processing, and control-by-wire actuation, the cooperative control of CAV systems is explored in the context of vehicular CPS (Cao et al. 2012).

In the literature, the cooperative control of CAV systems can be considered as a combination of four components, which are agent dynamics, communication topology, distributed controller, and formation geometry, respectively (Li et al. 2015). In addition, three different types of cooperative control of CAV systems can be roughly summarized. The interested readers may refer to (Siegel, Erb, and Sarma 2017; Rios-Torres and Malikopoulos 2016; Guanetti, Kim, and Borrelli 2018) for the detailed survey of CAV systems.

The first type is the cooperative adaptive cruise control (CACC), which is an extension of the ACC (Van Arem, Van Driel, and Visser 2006). The ACC aims to achieve constant distance or time gap among vehicles via automated speed control to release human driver burden (Vahidi and Eskandarian 2003). However, the ACC has issues resulted from inherent sensor delays and string instability. Thus, the CACC typically tries to maintain constant time gaps among multiple vehicles via wireless communication, through which the issues of the ACC are resolved (Milanes et al. 2014). While most of the CACC can control vehicle speeds automatically, the steering commands still need to be provided by human drivers.

The second type of cooperative control of CAV systems is vehicle platooning, which tries to improve transportation capacity, safety, and energy efficiency through a rigid vehicle platoon formation (Jia et al. 2016). Back in the 1980s, many fundamental theories and concepts in the vehicle platooning control were investigated in Partners for Advanced Transportation Technology (PATH) research program at the University of California, Berkeley (Hedrick, Tomizuka, and Varaiya 1994). Compared with the CACC, the platooning can provide additional active steering control and maintain

very short vehicle distances with a close coupling relationship among vehicles (Jia et al. 2016; Hedrick, Tomizuka, and Varaiya 1994). Moreover, the multiple platooning (multi-platooning) control was also proposed, which could consider multi-platoon joining and leaving maneuvers (Fernandes and Nunes 2015).

Nevertheless, both the CACC and the vehicle platooning control mainly involve a one-dimensional (1D) fluid model and a single-string communication topology within a single dedicated lane traffic flow. In other words, vehicle lateral dynamics and communication are not substantially discussed. Therefore, the CACC and the platooning cannot fully take advantage of multi-vehicle cooperation in two-dimensional (2D) traffic.

The third type is the flocking control of CAV systems, even though few research papers discuss the flocking application of CAV systems (Iftekhar and Olfati-Saber 2012; Xu et al. 2016; Liu and Xu 2015). The flocking is a swarm ubiquitous congregating phenomenon in groups of agents with self-organizing features, which can be modeled and analyzed by developing different flocking theories (Tanner, Jadbabaie, and Pappas 2003; Arcak 2007; Olfati-Saber 2006). More descriptions and details of flocking theories would be provided in sections 1.2.2 and 2.2. With the development of the flocking theory, while the concept "flocking" is still used, more factors are enclosed in the flocking theory, such as objective tracking, and obstacle avoidance (Olfati-Saber 2006; Tanner, Jadbabaie, and Pappas 2007; Su, Wang, and Lin 2009; R. Olfati-Saber and R. Murray 2004). Therefore, currently, most of flocking theories do not refer to a unique flocking behavior but the integration of flocking consensus, objective tracking, and obstacle avoidance. Considering various cooperative swarm behaviors for the multi-agent system, different swarm controls may have different global objectives (Siciliano and Khatib 2016). Theoretically, compared with other swarm controls,

the flocking theory is able to satisfy all aforementioned objectives of the cooperative control of CAV systems. Namely, the flocking theory has the closest control goals for the application of CAV systems.

The flocking control has a good fit to achieve the full 2D interaction in transportation systems, in which the cooperative behaviors are anticipated for CAV systems to improve the traffic energy efficiency, capacity, and safety. Besides, flocking control is suitable for implementations. The flocking control is usually achieved in a distributed manner without a centralized communication center, which shows vast advantages in terms of low cost, robustness, and strong scalability (Wang and Peng 2012). Moreover, communications among agents can be frequently connected or disconnected, which are represented by uncertain switching algebraic graphs instead of fixed and symmetrical topology (Olfati-Saber 2006). Therefore, flocking theories can be applied to a group of automated vehicles without the scalability issue, and only the local communication, computation, and sensing are required. Hence, the flocking theory processes great potential to deal with traffic congestion and fatalities problems.

Note that in this dissertation, the concept of "agent" is used in generous multi-agent systems, which can be replaced by "vehicle" or "CAV" for specific vehicular applications.

1.2.2 Flocking Control in Multi-Agent Systems

Flocking is a swarm dynamic coordination behavior of multi-agent systems with maintaining the constant inter-agent distance, matching the speed, and avoiding the collision. In nature, flocking phenomena prevalently exist in the migrations of a group of animals, such as birds, fishes, bees, and bacteria (Okubo 1986; Toner and Tu

1998). Featured by self-organizing characteristic, strong scalability, and uncertain interaction communication topology, flocking phenomena spur broad interdisciplinary engineering applications in the distributed cooperative control of artificial multi-agent systems over large-scale complex networks, such as intelligent transportation systems, military systems, mobile robots, and mobile sensor networks (Murray 2007; Motsch and Tadmor 2011; Tanner 2007; Turgut et al. 2008).

In past decades, to understand this fascinating and complicated motion pattern, scientists and researchers investigated the basic theory in three main aspects to model, animate, and analyze the flocking phenomena. First, a set of flocking rules was proposed to describe the working principles of natural flocks. For example, Reynolds proposed three well-known heuristic rules in the 1980s (Reynolds 1987), which consisted of cohesion, separation, and alignment. Other flocking rules such as virtual leader seeking of flocks (Su, Wang, and Lin 2009) and obstacle avoidance (R. Olfati-Saber and R. Murray 2003) were also investigated. For instance, Su et al. studied the goal-seeking of flocks with multiple virtual leaders (Su, Wang, and Yang 2008). Moreover, Tanner et al. discussed the flocking obstacle avoidance (Tanner, Jadbabaie, and Pappas 2003).

Second, many mathematical modeling methods of flocks were also studied. In 1987, Reynolds developed the Boid model to simulate flocking behaviors together with his three simple rules (Reynolds 1987). In 1995, the Vicsek model was proposed by simplifying the Boid model and achieving velocity synchronization and position stabilization (Vicsek et al. 1995). The Vicsek model was extended in 2002 to three-dimensional space with sensing zones, which is called the Couzin model (Couzin et al. 2002). The Couzin model can exhibit behaviors of torus and self-sorting. In

addition, the Cucker-Smale model is also a pioneering work to describe how agents interact to align with their neighbors (Cucker and Smale 2007).

Third, regarding different agent dynamics, a great number of flocking control methods were developed to achieve the proposed flocking rules, such as Lyapunov-based approaches, optimization-based approaches, graph-theoretic approaches, and passivity-based approaches (R. Olfati-Saber and R. Murray 2004; Tanner, Jadbabaie, and Pappas 2003; Liu and Xu 2015; Arcak 2007; Hong et al. 2007; Dunbar and Murray 2006). Representatively, Olfati-Saber suggested a theoretical framework for analysis and design of decentralized flocking algorithms with a switching network connectivity structure (Olfati-Saber 2006), which integrated the passivity-based approach with a velocity consensus term for objective tracking.

1.2.3 Electric Vehicle System and Control with Over-Actuated Features

Spurred by the decline of fossil fuel and the strict emission requirements for environmental protection, the development of electric vehicles (EVs) with few/no emissions and high efficiency gathers significant concerns recently (Wada 2009; Noori, Gardner, and Tatari 2015; Burke 2007). In 2017, there are more than 3 million EVs on the road worldwide, and the sales of new EVs surpassed 1 million units (Noori, Gardner, and Tatari 2018). Concurrently, the rapidly expanded market of EVs also promotes the explosion of new vehicle electrification technologies, such as the distributed propulsion architecture with in-wheel motors (IWMs) and steer-by-wire actuation systems (Noori, Gardner, and Tatari 2018; Murata 2012). One significant advantage of these electrification technologies is to provide redundant actuators to improve the safety, energy efficiency, and agility of EVs (F. Wang et al. 2019; Peng

9

et al. 2019). For instance, the direct yaw moment control (DYC) and the four-wheel steering (4WS) control achieved by the IWMs and 4WS can simultaneously prevent vehicle rollover and maintain the input-output stability of vehicle planar motions (H. Wang et al. 2014; Wang and Chen 2018c).

For vehicles with over-actuated features, a hierarchical control configuration is a common framework to generate high-level virtual controls for certain control purposes. Then, control allocation is usually utilized to produce real controls by distributing the virtual controls to all available actuators. Intuitively, the number of available actuators is more than the number of virtual controls. Actually, a control allocation problem is an optimization problem with constraints, which penalizes the dissatisfaction of virtual controls as well as the energy consumption of real controls. The detailed control allocation information may refer to (Johansen and Fossen 2013).

Using control allocation, researchers and engineers have successfully enhanced vehicle stability and energy efficiency. For example, an automotive vehicle yaw stabilization scheme was developed via a dynamic control allocation approach (Tjonnas and Johansen 2009). Furthermore, an energy efficiency improvement method for electric vehicle planar motion was proposed with adaptive control allocation (Chen and Wang 2013).

1.3 Challenges in Flocking Control of CAV Systems

Currently, numerous studies about 1D CACC and platooning were explored. However, the flocking modeling and control of CAV systems for a general 2D planar motion are not well studied.

First, nonlinear vehicle dynamics are not fully explored in the flocking control of CAV systems. For example, a group of agent models simplified as single or double-integrator dynamics were used to directly apply existing flocking control protocols (Liu and Xu 2015; Iftekhar and Olfati-Saber 2012), instead of using practical vehicle planar dynamics with nonlinear tire models.

Second, vehicle yaw/orientation dynamics was not well addressed. In the existing flocking theory (Olfati-Saber 2006), the orientation of each agent was not intentionally controlled when the simplified point-mass modeling of agents was applied. Theoretically, the double-integrator dynamics is under-actuated when the additional control of yaw/orientation dynamics is required. Hence, Olfati-Saber firstly proposed to use the near-identity diffeomorphism (NID) transformation to partially linearize a class of kinematic $SE(2)$ vehicles that engaged yaw motions (Olfati-Saber 2002; Iftekhar and Olfati-Saber 2012). However, a vehicle could be an over-actuated system. In this regard, the NID transformation cannot be directly applied without sacrificing the control performance of CAV systems since the control degrees of freedom cannot be fully utilized. Moreover, the application of the NID transformation in the flocking theory may lead to inappropriate flocking control protocols, which are transformed for the yaw/orientation control of vehicles. The stability of vehicles, especially for yaw motions, is therefore not guaranteed. The proof of the stability issue of the NID transformation is referred to as section 4.2.

Third, the existing flocking control is not suitable for transportation system applications. On the one hand, the original flocking control algorithms do not adapt to traffic rules and shared driving environments. For instance, the assumptions of free flocking and temporary obstacles may fail or even be impossible in transportation systems, in which lane boundaries could be permanent obstacles for every agent/vehicle.

Furthermore, the flocking behaviors of vehicles also need to handle lane-keeping and lane-changing situations based on the traffic rules. On the other hand, the specific requirements of flocking performances emerged from transportation system applications. For example, CAV systems may need to consider energy efficiency from a system level. Moreover, convergence speed is also a critical concern in practical engineering applications.

Fourth, over-actuated vehicle control systems still need further investigations regarding complicated tire-road contact conditions. Additional actuators or novel advanced control methods are excepted to be applied to improve vehicle safety.

Fifth, no experimental validation has been carried out to prove the feasibility, robustness, and accuracy of flocking applications. The field tests should be conducted to bridge flocking theoretical works and experimental validations, in which all CAVs are fully controlled in a distributed manner. The tunable parameters in flocking algorithms could be obtained for real vehicles as well.

1.4   Statement of Contributions

To tackle the aforementioned challenges, this dissertation seeks to promote the application of the 2D flocking theory in the cooperative control of CAV systems with over-actuated features. The board contributions of this dissertation lie in the following aspects, which are summarized in Fig. 1 as well[1].

_____

[1]To make this dissertation completed, in Appendix A, several novel vehicle dynamics control methods are studied by fully utilizing the advantages of extra actuators. Maintaining vehicle stability, additional actuators, namely active yaw stabilizer and active rollover preventer, are applied to enhance vehicle yaw/lateral and roll stability. To detect both tripped and untripped rollover, a new rollover index, named mass-center-position metric, is developed.
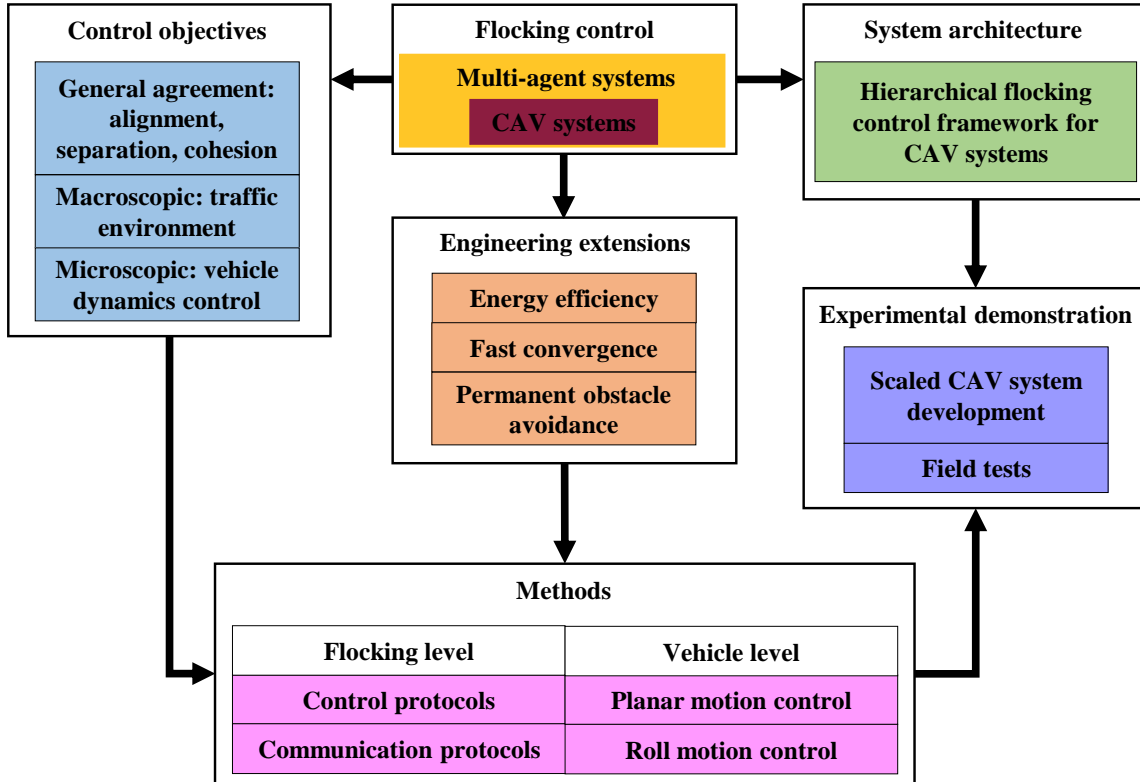
Figure 1. Summary of dissertation contributions.

First, several new flocking control algorithms are developed to accommodate flocking rules and traffic environments. The performance considerations of fast convergence speed, permanent obstacle avoidance, and energy efficiency are used to extend the engineering applications of flocking theory.

Second, a novel hierarchical flocking control framework for CAV systems to integrate path planning, speed profile generation, and nonlinear vehicle dynamics control. With hierarchical configuration, the proposed flocking control framework can adapt to complicated vehicle dynamics with a self-organizing feature. In the high-level layer, applying a 2D flocking theory, the cooperative trajectories (paths and speeds) of CAV systems are produced via a distributed control based on shared information. In the low-level layer, the trajectory tracking and vehicle orientation guidance of

vehicles are achieved by a feedforward and feedback control design. In particular, control allocation is established to take the merits of the over-actuated properties of each vehicle. Note that the proposed framework can be applied to other autonomous systems as well, such as unmanned aerial vehicles, autonomous underwater vehicles, and mobile robots.

Third, experimental validations are conducted to demonstrate the proposed hierarchical flocking control framework. Three scaled CAVs with a wireless communication network are developed as a general research platform. Additionally, three flocking cases are also exhibited to further confirm results obtained from simulations in a practical fashion.

1.5   Dissertation Roadmap

This dissertation is organized in the following way.

In Chapter 2, a brief preliminary is presented to summarize several key concepts of algebraic graph theory. Moreover, a brief introduction of conventional flocking control algorithms and basic analysis tools is given.

In Chapter 3, several novel flocking rules and protocols are proposed to accommodate transportation engineering applications. The convergence speed, permanent obstacle avoidance, and energy efficiency are investigated.

In Chapter 4, a novel hierarchical flocking coordination framework is proposed to integrate flocking control and vehicle dynamics control. Besides, the sectionalization and transformation of vehicle models, vehicle predictive orientation guidance, and low-level controller design are also presented.

In Chapter 5, experiments are conducted to demonstrate novel flocking protocols. A scaled CAV system is developed for experimental research. Furthermore, experimental results are analyzed to convince the proposed hierarchical flocking control of CAV systems.

Finally, in Chapter 6, conclusions are summarized, and future potential research directions are proposed.

Chapter 2

PRELIMINARIES

The graph-based abstraction method plays an important role in the analysis and synthesis control of multi-agent systems, which provides a system-level network topology description in terms of the interaction geometry including vertices and edges. Hence, this chapter covers some basic concepts and analysis tools used in algebraic graph theory used throughout this dissertation. More details about algebraic graph theory may refer to (Godsil and Royle 2013). In addition, several significant preliminary results of the flocking control theory are discussed as well.

2.1 Algebraic Graph Theory

2.1.1 Basic Concepts

The geometry topology of flocks is modeled by a proximity structure (G, q), where $q = \mathrm{col}(q_1, \ldots, q_n) \in \mathbb{R}^{mn}$ denotes the spatial geometry configuration of n agents in a m-dimensional space, and G is the proximity net of a graph that consists of a pair of vertices and edges indicated in (2.1).

$$\mathcal{E}(q) = \{(i,j) \in \mathcal{V} \times \mathcal{V} : \|q_j - q_i\| < d_r, i \neq j\}, \mathcal{V} = \{1, 2, \ldots, n\}, \qquad (2.1)$$

where d_r is the interaction range of agents, and $\| \cdot \|$ represents the 2-norm operation.

Based on the edge definition, a set of spatial neighbors of agent i is defined by (2.2).

$$N_i = \{j \in \mathcal{V} : \|q_j - q_i\| < d_r, i \neq j\}. \qquad (2.2)$$

2.1.2 Graph Matrices and Laplacians

The adjacency matrix $A = [a_{ij}]$ of a graph is a matrix where the elements represent the connective weights among vertices. When a pair of vertices are connected through an edge, we have $a_{ij} \neq 0 \iff (i, j) \in \mathcal{E}$; otherwise, $a_{ij} = 0$. A graph is called weighted whenever its adjacency matrix contains other than just 0-1 elements. Furthermore, a graph is called undirected if an only if its adjacency matrix is symmetric.

The Laplacian matrix of a graph, denoted as $\mathcal{L}$, and its spectral properties are used to analyze convergence and stability performance. The scalar graph Laplacian is a matrix associated with G, which is defined in (2.3).

$$\mathcal{L} = \Delta(A) - A, \tag{2.3}$$

where $\Delta(A)$ is the degree matrix of G as decipted in (2.4).

$$\Delta(A) = \text{diag} \left(\sum_{j=1}^{n} a_{ij} \right), i \in \mathcal{V}. \tag{2.4}$$

Laplacian matrix $\mathcal{L}$ always has a zero eigenvalue $\lambda_1 = 0$. To evaluate the convergence performance of a multi-agent system, the minimum non-zero eigenvalue of Laplacian matrix, denoted as $\lambda_2(\mathcal{L})$, indicates the worst-case convergence speed.

2.2 Flocking Theory

2.2.1 Flocking Control

In flocking theory, three categories of agents are typically defined, which are α-agents, β-agents, and γ-agents, respectively. The α-agents represent the flock

that performs flocking behaviors, the dynamics of which are depicted as a class of double-integrator equations in (2.5).

$$\begin{cases} \dot{q}_i = p_i \\ \dot{p}_i = u_i \end{cases} \quad i \in \mathcal{V}, \tag{2.5}$$

where q_i, p_i and $u_i \in \mathbb{R}^m$ denote the position, velocity and control input of α-agent i. The β-agents represent obstacles, which typically interact with α-agents through repulsive forces. The γ-agents are (virtual) leaders of a group of α-agents, which can provide the position and speed trajectory references for α-agents to avoid fragmentation among α-agents.

Given the α-agent dynamics described in (2.5), the flocking control protocol u_i is given in (2.6) (Olfati-Saber 2006).

$$u_i = f_i^{\alpha} + f_i^{\beta} + f_i^{\gamma}, \tag{2.6}$$

where f_i^{α} is the control effort to regulate the desired lattice geometry without collision among α-agents, f_i^{β} is the repulsive force for the obstacle avoidance, and f_i^{γ} is the navigational term to collectively enable the objective position and speed tracking.

The desired geometry topology of the flocking coordination is typically recognized as a lattice formation, which satisfies the constraints in (2.7).

$$- \epsilon \le \left\| q_i - q_j \right\| - d \le \epsilon, \forall (i, j) \in \mathcal{E}(q), \tag{2.7}$$

where d is the lattice scale and ϵ is the edge-length uncertainty.

2.2.2   Flocking Hamiltonian Operator

In flocking theory, a Hamiltonian operator, which is a strong analytic tool to evaluate the behaviors of a group of agents, is typically used to describe the satisfaction

of the flocking rules required by desired flocking phenomena. Therefore, the associated Hamiltonian, which consists of the structural potential collective energy and kinetic energy of a multi-agent system, is formulated in (2.8) to evaluate the satisfaction of the flocking rules of the multi-agent system, which include the formation of the desired lattice (cohesion), collision avoidance among α-agents (separation), speed matching among α-agents (alignment), obstacle avoidance, and position and speed tracking of a virtual navigational leader.

$$H(q, p) = K(p) + V(q), \tag{2.8}$$

where $p = \text{col}(p_1, \cdots, p_i, \cdots p_n) \in \mathbb{R}^{mn}$, and $K(p)$ is the relative kinetic energy related to a virtual leader, γ-agent, which is defined in (2.9) to imply the performance of alignment and speed tracking.

$$K(p) = \frac{c_1^\gamma}{2} \sum_{i \in \mathcal{V}} \|p_i - p_r\|^2 \geq 0, \tag{2.9}$$

where c_1^γ is a constant weight, and p_r is the velocity of the γ-agent.

The potential energy $V(q)$ in (2.8) consists of three parts depicted in (2.10).

$$V(q) = V_\alpha(q) + V_\beta(q) + V_\gamma(q), \tag{2.10}$$

where V_α, V_β, and V_γ are potential energy functions that represent the interaction effects among α-α agents, α-β agents, and α-γ agents, respectively. In details, V_α is defined in (2.11), which attempts to evaluate the performance of cohesion and separation among α-agents.

$$V_\alpha(q) = c^\alpha \sum_{i \in \mathcal{V}} \sum_{j \in \mathcal{V}/\{i\}} \left[\int_{\|d\|_\sigma}^{\|q_j - q_i\|_\sigma} \phi_\alpha(x) \mathrm{d}x \right] \geq 0, \tag{2.11}$$

where c^α is a constant weight, and $\|\cdot\|_\sigma$ denotes σ-norm defined in (2.12) to make $\|\cdot\|_\sigma$ differentiable everywhere.

$$\|z\|_\sigma = \frac{1}{\sigma} \left[\sqrt{1 + \sigma\|z\|^2} - 1 \right], \tag{2.12}$$

19

where $\sigma \in (0,1)$ is a small constant. Additionally, ϕ_α is a coordination action function to generalize a smooth pairwise potential energy with a finite cut-off, which is presented in (2.13).

$$\phi_\alpha(z) = \rho_h(z/\|d_r\|_\sigma)\phi(z - \|d\|_\sigma), \tag{2.13}$$

where

$$\rho_h(z) = \begin{cases} 1 & z \in [0, h) \\ \frac{1}{2}\left[1 + \cos\left(\pi\frac{z-h}{1-h}\right)\right] & z \in [h, 1] \\ 0 & \text{otherwise} \end{cases} \tag{2.14}$$

where $h \in (0,1)$. In addition,

$$\phi(z) = \frac{1}{2}[(a + b)\sigma_1(z + c) + (a - b)], \tag{2.15}$$

in which $\sigma_1(z) = z/\sqrt{1 + z^2}$, and the parameters a, b, and c satisfy $0 < a \le b$ and $c = |a - b|/\sqrt{4ab}$.

The potential energy between α-agents and β-agents, namely V_β, is formulated in (2.16) to evaluate the relative positions between α-agents and obstacles.

$$V_\beta(q) = c^\beta \sum_{i \in \mathcal{V}} \sum_{k \in N_i^\beta} \int_{\|\hat{d}\|_\sigma}^{\|\hat{q}_{i,k} - q_i\|_\sigma} \phi_\beta(x)\mathrm{d}x \ge 0, \tag{2.16}$$

where c^β is a constant weight, and $\hat{d}$ is the constant interaction range of α-agents for detecting β-agents, and $\phi_\beta \le 0$ is an repulsive obstacle action function defined in (2.17).

$$\phi_\beta(z) = \rho_h(z/\|\hat{d}\|_\sigma)(\sigma_1(z - \|\hat{d}\|_\sigma) - 1). \tag{2.17}$$

In addition, N_i^β is the neighbor set of α-agent i composed by β-agents, and $\hat{q}_{i,k}$ can be determined by the closest distance from the position of a point on the neighboring obstacle boundary as shown in (2.18).

$$\hat{q}_{i,k} = \arg\min_{x \in O_k}\|x - q_i\|. \tag{2.18}$$

The potential energy regarding to the virtual leader position tracking of α-agents, namely V_γ, is presented in (2.19).

$$V_\gamma(q) = c_2^\gamma \frac{1}{2} \sum_{i \in \mathcal{V}} \|q_i - q_r\|^2 > 0, \qquad (2.19)$$

where c_2^γ is a constant weight, and q_r is the position of the γ-agent.

Chapter 3

DEVELOPMENT OF NOVEL FLOCKING CONTROL ALGORITHMS

3.1   Overview

Actually, most of flocking rules and flocking algorithms attempt to provide the interaction protocols of multi-agent systems among α-agents, β-agents, and γ-agents. In this regard, various flocking control protocols are actually used to regulate interactions in multi-agent systems considering α-agents, β-agents, and γ-agents. To promote the engineering applications of flocking theory, this chapter aims to investigate the performances of fast convergence, permanent obstacle avoidance, and energy efficiency, which involve α-α, α-β, and α-γ interactions, respectively. The detailed contributions of this chapter are summarized as follows [2].

1. To improve flocking convergence speed for completing certain emergent tasks, e.g. quick seeking and rescue, a novel fast-convergence flocking control method of multi-agent systems with switching communication topology is proposed. First, a new distributed per-step convergence factor (D-PCF) is defined to indicate the convergence speed of each agent. Then, to decrease the D-PCF and thus increase flocking convergence speed, a new distributed fast synchronization (DFS) algorithm is developed to determine position-dependent and velocity-dependent adjacency weights on every communication channel of an ad hoc network of multi-agent systems. The simulation results show that compared

---

[2]The main content of this chapter is based on the author's works in (Wang and Chen 2020b), (Wang and Chen 2019b), and the manuscript "Flocking control of multi-agent systems with permanent obstacles in strictly confined environments" submitted to *Automatica*.

with conventional flocking control, the flocking control with the DFS algorithm can significantly accelerate flocking convergence speed without requiring larger control inputs.

2. Considering flocking behaviors in a strictly confined environment, the persistent interactions always existing between flocking agents and permanent boundaries (obstacles) is critical for engineering applications. To handle permanent obstacles, this chapter proposes a novel flocking control algorithm to guarantee the desired flocking coordination of multi-agent systems with permanent obstacle constraints. By analyzing the comprehensive behaviors of flocks via the Hamiltonian function, an obstacle zero-sum condition is developed to ensure the satisfaction of required flocking rules including permanent obstacle avoidance. Then, an additional control term representing the resultant influence of permanent obstacles is introduced to tackle interactions from permanent obstacles in a strictly confined space. Demonstrated and compared through simulation results, a multi-agent system steered by the proposed flocking control protocol can successfully achieve the desired flocking behaviors with permanent obstacles avoidance.

3. Inspired by cooperative foraging behavior in goose flocks, a distributed least-informed (DLI) method is introduced to achieve energy-efficient flocking control by selecting the least required informed agents. To avoid the fragmentation issue when applying the DLI method, three new concepts about the informed path, cycle, and tree are proposed. Based on the properties of the proposed new concepts, a theorem of fragmentation prevention is developed for multi-agent systems with a fraction of informed agents. Utilizing the developed theorem of fragmentation prevention, the initialization and updating principles of the selection of the least informed agents in the DLI method are described.

Simulation results demonstrate that by using the DLI method, a multi-agent system of 30 agents can successfully achieve energy-efficient flocking control without fragmentation. Namely, a collective motion around a defined objective with velocity consensus (flock formation) is achieved by a total 15.9% energy reduction, compared with the completed informed method.

3.2 Fast-Convergence Flocking Control of Multi-Agent Systems with Switching Communication Topology

The flocking convergence speed is a critical concern in some practical emergent flocking tasks, e.g. quick seeking and rescue (Murray 2007). However, in existing flocking research, only the asymptotic stability of flocking control protocols is analyzed via LaSalle's invariance principle (Olfati-Saber 2006), but the flocking convergence speed is not well discussed. Therefore, it is necessary to investigate the fast-convergence flocking control of multi-agent systems.

In the literature, the most fast-convergence problem for multi-agent systems is studied in consensus controls or averaging with a fixed communication topology and first-order agent dynamics. Usually, the Laplacian matrix $\mathcal{L}$ and its spectral properties of a multi-agent system abstracted as an algebraic graph G were used to analyze the convergence and stability performance (Godsil and Royle 2013). To evaluate flocking convergence performance, the minimum non-zero eigenvalue of the Laplacian matrix, $\lambda_2(\mathcal{L})$, indicates the worst-case convergence speed. Furthermore, an asymptotic or per-step convergence factor (PCF) for the whole multi-agent system, denoted as ρ, was also determined to give convergence time (Xiao and Boyd 2004). For a first-order multi-agent system with a fixed communication topology, the configuration of

the Laplacian matrix is fixed. Therefore, it is possible to minimize $\lambda_2(\mathcal{L})$ or ρ by searching optimal fixed adjacency weights off-line on each edge of G, while it may be a challenging optimization problem neither convex nor locally Lipschitz (Xiao and Boyd 2004; Kim 2010; Kim and Mesbahi 2006; Liu and Morse 2011). For example, L. Xiao et al. considered the fast convergence performance of linear iterations yielding distributed averaging consensus (Xiao and Boyd 2004).

Nevertheless, a switching communication topology in multi-agent systems with ad hoc networks is more common in flocking applications, whereas the failure and creation of connections between two agents happened frequently. Thus, the real-time distributed optimization of adjacency weights is necessary to improve flocking convergence speed. Furthermore, the second-order multi-agent systems are also more practical in reality. Unfortunately, few research works address the enhancement of convergence speed in flocking control considering the second-order agent dynamics and switching communication topology.

Motivated by the aforementioned problems, this chapter proposes the D-PCF to represent the disagreement status of flocking controls and develops the novel DFS algorithm to improve the flocking control convergence speed of second-order multi-agent systems, regarding the switching communication topology.

3.2.1   Flocking Distributed Disagreement Function and Convergence Factor

The disagreement function refers to a measure of the group disagreement in a networked multi-agent system. In the context of flocking control, three well-known Reynolds heuristic rules of flocking behaviors are applied to design the disagreement function, which include cohesion, separation, and alignment rules (Reynolds 1987). In
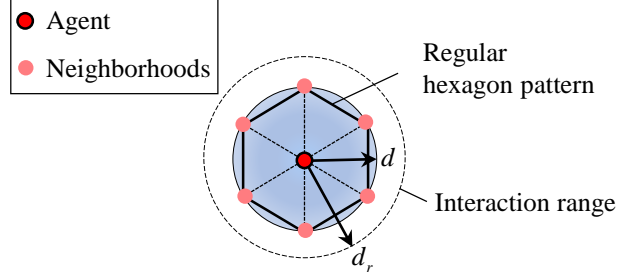
Figure 2. Regular hexagon pattern in a flocking lattice formation.

addition, virtual leader tracking and obstacle avoidance are also anticipated in flocking. Therefore, the Hamiltonian of a multi-agent system for flocking consensus control is defined as (2.8). The decision value is also an important parameter in the cooperative control of multi-agent systems. In the flocking control problem, the decision value is the common value of a group of agents whenever the agents are all in an agreement of the flocking rules. Therefore, the associated decision value of the disagreement function H is one of its local minima, denoted as H^*.

To examine the distributed disagreement status, a distributed Hamiltonian is proposed to indicate the local satisfaction of the flocking rules of each agent. For every α-agent $i \in \mathcal{V}$, an associated sub-graph G_i can be defined, which consists of a pair of vertices $\mathcal{V}_i = i, N_i$ and directed edges $\mathcal{E}_i = (i, j) : j \in N_i$. Corresponding to α-agent i, the distributed Hamiltonian over G_i is defined as (3.1).

$$H_i = V_i^\alpha + V_i^\gamma + K_i, i \in \mathcal{V}, \tag{3.1}$$

where V_i^α, V_i^γ and K_i are the distributed collective potential of lattice formation and virtual leader position tracking, and relative kinematic energy of G_i, respectively. Intuitively, H_i are determined by only using information shared between α-agent i and its neighborhoods.

26

Theoretically, based on the lattice formation with the constraint in (2.7), a regular hexagon pattern around an α-agent, illustrated in Fig. 2, is expected as a successful lattice formation. That is because the regular hexagon is the most compact geometry shape that can fit together without leaving gaps and keep identical distance among vertices (Ball 2016). From Fig. 2, based on the Reynolds flocking rules, three requirements for achieving the regular hexagon pattern include: i) the ideal number of α-agents in N_i should be at most six if the condition $d_r \in (d, \sqrt{3}d)$ holds; ii) the gap between α-agent i and every α-agent in N_i is d; iii) the position configuration of α-agents in in N_i should be distributed evenly on the circle centered at α-agent i. Hence, V_i^α is defined as (3.2), which only uses local information sharing, and the logarithmic operator in (3.2) ensures $V_i^\alpha = 0$ if and only if Λ_i, e_i, and Ξ_i all equal to zero.

$$V_i^\alpha = \ln \left[(1 + \Lambda_i)(1 + e_i)(1 + \Xi_i) \right], i \in \mathcal{V}, \tag{3.2}$$

where Λ_i indicates the satisfaction of the number of neighbors in N_i, which is depicted in (3.3).

$$\Lambda_i = \begin{cases} 0 & |N_i| \leq 6 \\ |N_i| & |N_i| > 6 \end{cases}, i \in \mathcal{V}, \tag{3.3}$$

where $|N_i|$ denotes the number of neighbors. In addition, e_i denotes the summation of the satisfaction errors of the lattice scale between α-agent i and its neighbors, which is depicted in (3.4).

$$e_i = \sum_{j \in N_i} |d_{ij} - d|, i \in \mathcal{V}, \tag{3.4}$$

where $d_{ij} = \left\| q_j - q_i \right\|$. The position distribution of neighbors is evaluated by Ξ_i, which is defined as (3.5).

$$\Xi_i = \left\| \sum_{j \in N_i} \frac{q_j - q_i}{\left\| q_j - q_i \right\|} \right\|, i \in \mathcal{V}. \tag{3.5}$$

The term V_i^γ and K_i in (3.1) are defined in (3.6) and (3.7), respectively.

$$V_i^\gamma = \left\| q_j - q_i \right\|, i \in \mathcal{V}, \tag{3.6}$$

$$K_i = \frac{1}{2} \left(\sum_{j \in N_i} \left\| p_j - p_i \right\|^2 + \left\| p_i - p_r \right\|^2 \right), i \in \mathcal{V}. \tag{3.7}$$

Lemma 3.2.1. *Considering α-agent i and $d_r \in (d, \sqrt{3}d)$ in a multi-agent system with a distributed Hamiltonian H_i defined in (3.1), the local minimum of H_i is zero and implies that α-agent i satisfies the Reynolds flocking rules and virtual leader tracking.*

Proof. From (3.3), (3.4), and (3.5), it can be seen that Λ_i, e_{ij}, and Ξ_i are all non-negative. Therefore, the values of the natural logarithm function in (3.2) are always non-negative, so that $V_i^\alpha \geq 0$. Especially, the condition i), ii), and iii) are held when $V_i^\alpha = 0$. In addition, V_i^γ and K_i in (3.6) and (3.7) are summations of a set of 2-norm functions, which result in $V_i^\gamma \geq 0$ and $K_i \geq 0$, and $V_i^\gamma = 0$ and $K_i = 0$ imply the achievement of the position and velocity tracking of the virtual leader.

To sum up, we have

$$H_i = V_i^\alpha + V_i^\gamma + K_i \geq 0, i \in \mathcal{V}. \tag{3.8}$$

The local minima of H_i are zero that satisfy the flocking rules. $\qquad \square$

Remark 3.2.1. The failure of the achievement of zero distributed Hamiltonian does not mean the dissatisfaction of flocking rules. For instance, when $|N_i|$ is 1 for α-agent i, it is impossible to make $\Xi_i = 0$, thus $H_i \neq 0$. Nevertheless, we may not be able to claim that α-agent i breaks the condition i) and iii) if it locates at the geometry edge of a multi-agent system.

The potential energy representing the interaction among α-α agents in (2.8), namely V_α, is not the exact sum of the distribution collective potential of lattice

formation, V_i^α in (3.1), since the number and position distribution of neighborhoods of α-agent i have to be considered in V_i^α.

The relationship between the decision value H^* of the whole multi-agent system and the distributed Hamiltonian is described in Theorem 3.2.1.

Theorem 3.2.1. *Assuming $|N_i| > 1, \forall i \in \mathcal{V}$ and considering a multi-agent system with a set of distributed Hamiltonians H_i, the decision value of the multi-agent system, H^*, is achieved if the following condition (3.9) holds.*

$$\sum_{i \in \mathcal{V}} H_i = V_\gamma^*, \tag{3.9}$$

where V_γ^* denotes a local minimum of V_γ.

Proof. Using (3.1), (3.2), (3.6) and (3.7) for all α-agents in the multi-agent system, we have

$$\sum_{i \in \mathcal{V}} H_i = \sum_{i \in \mathcal{V}} (V_i^\alpha + V_i^\gamma + K_i) = V_\gamma + K + \sum_{i \in \mathcal{V}} V_i^\alpha. \tag{3.10}$$

The quadratic form of (2.19) makes the values of V_γ non-negative. However, V_γ cannot be zero since it is impossible for all α-agents to locate at p_r simultaneously, namely $p_i = p_r, \forall i \in \mathcal{V}$, which violates the flocking rules on cohesion and alignment. Therefore, the flocking rule on the position tracking of α-agents with respect to the γ-agent is achieved whenever $V_\gamma = V_\gamma^* > 0$. Therefore, using Lemma 3.2.1, we have

$$\sum_{i \in \mathcal{V}} H_i \geq V_\gamma^*. \tag{3.11}$$

As a result, whenever the summation of distributed Hamiltonians equals to V_γ^*, the Reynolds flocking rules and virtual leader tracking are satisfied, and the decision value of the multi-agent systems is achieved. Specially, the decision value H^* equals to V_γ^*. $\qquad\square$

The PCF is a measure of the convergence speed to achieve the decision value (Xiao and Boyd 2004). Using the disagreement function H and its decision value H^*, the following formula in (3.12) defines the PCF at the time interval k.

$$\rho[k] = \sup_{H[k-1]\neq H^*} \frac{\left\|H[k] - H^*\right\|}{\left\|H[k-1] - H^*\right\|}. \tag{3.12}$$

In the same way, based on the distributed Hamiltonian, the D-PCF of α-agent i is described in (3.13).

$$\rho_i[k] = \sup_{\Theta_i[k-1]\neq \Theta_i^*} \frac{\left\|\Theta_i[k] - \Theta_i^*\right\|}{\left\|\Theta_i[k-1] - \Theta_i^*\right\|}, \tag{3.13}$$

in which $\Theta_i = V_i^\alpha + \frac{1}{2}\sum_{j\in N_i}\left\|p_j - p_i\right\|^2$, and Θ_i^* denotes the decision value of Θ_i that is zero. From (3.13), the D-PCF $\rho_i > 1$ indicates the increase of Θ_i, and the larger ρ_i implies the faster increase of Θ_i. Otherwise, $\rho_i < 1$ indicates the decrease of Θ_i, and the smaller ρ_i implies the faster decrease of Θ_i.

3.2.2   Fast Synchronization Strategy

The Laplacian matrix $\mathcal{L}$ is determined by algebraic connectivity information (adjacency weights) of multi-agent systems. Thus, given the adjacency weights a_{ij}, an adjacency matrix $A = [a_{ij}]$ and its associated Laplacian $\mathcal{L}(A)$ can be constructed. Based on the Laplacian analysis, the flocking convergence speed is actually determined by adjacency weights among agents (Godsil and Royle 2013). Therefore, determining an appropriate adjacency matrix A in real-time is a potential solution to decrease the flocking convergence factor.

In flocking theory, considering the adjacency matrix, the distributed control input u_i for a free-flocking scenario can be designed as (3.14), whose performance has been successfully demonstrated and analyzed in (Olfati-Saber 2006). Within (3.14), the
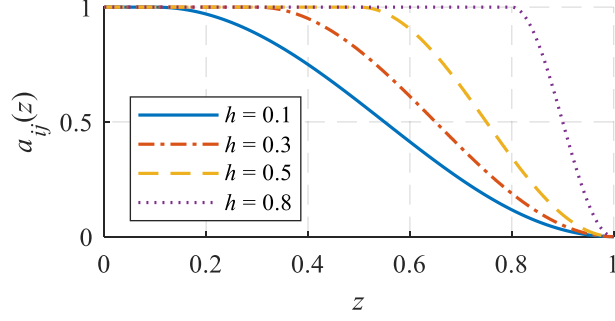
Figure 3. Adjacency bump function with respect to various values of h.

non-negative element a_{ij} of A affects producing attractive or repulsive forces between a pair of α-agents.

$$u_i = c^\alpha \sum_{j \in N_i} \left[-\mathbf{n}_{ij} \phi_\alpha \left(\left\| q_j - q_i \right\|_\sigma, a_{ij} \right), + a_{ij}(p_j - p_i) \right] - c_1^\gamma (p_r - p_i) - c_2^\gamma (q_r - q_i), \quad (3.14)$$

where $\mathbf{n}_{ij}$ denotes the unit vector along the line from α-agent i and α-agent j. Usually, a_{ij} is calculated through an adjacency bump function to provide position-dependent finite cut-offs and smooth adjacency weights. For example, the piecewise function shown in (3.15) was proposed in (R. Olfati-Saber and R. Murray 2003). From (3.15), it can be seen that $a_{ij} \in [0, 1]$ is held for all neighbors $j \in N_i$ of α-agent i. Furthermore, the parameter h alters the curve shape of the adjacency bump function. The influence of the different values of h on the curve shape of the adjacency bump function is presented in Fig. 3.

$$a_{ij}(z) = \begin{cases} 1 & z \in [0, h) \\ \frac{1}{2} \left[1 + \cos \left(\pi \frac{z-h}{1-h} \right) \right] & z \in [h, 1] \\ 0 & \text{otherwise} \end{cases}, \quad (3.15)$$

where $h \in (0, 1)$ is a constant, and $z = \left\| q_j - q_i \right\| / r$.

For a given adjacency bump function, a possible way to strengthen or weaken a_{ij} for additional fast convergence concerns is tuning function parameters in real-time. Hence, the decrease of flocking convergence factor could depend on the time-varying values of h if the adjacency bump function (3.15) is employed.

Based on Theorem 3.2.1, a minimum summation of distributed Hamiltonians also implies the achievement of the decision value. Namely, minimizing the distributed Hamiltonian of every agent also can make the multi-agent system reach a flocking agreement. Therefore, based on the D-PCF defined in (3.13), it is possible to accelerate the flocking control by achieving the least ρ_i for all α-agents, which provides the fastest convergence speed for Θ_i approaching Θ_i^*. To enhance flocking convergence speed, a distributed optimization problem can be established in (3.16).

$$
\begin{aligned}
\min_{q_i[k],p_i[k]} \quad & \rho_i[k] \\
\text{s.t.} \quad & q_i[k], p_i[k] \in \mathbb{R}^m, i \in \mathcal{V}
\end{aligned}
\tag{3.16}
$$

The solution of (3.16), denoted as $(q_i^*[k], p_i^*[k])$, is the optimal position and velocity of α-agent i, which can accommodate the minimum convergence factor. Thus, the adjacency weights a_{ij} should be adjusted to make states of α-agent i approach $(q_i^*[k], p_i^*[k])$. After solving (3.16), the curve shape of the adjacency bump function can be determined to make every agent move towards the desired position and velocity $(q_i^*[k], p_i^*[k])$, which can speedup the flocking control. Since $(q_i^*[k], p_i^*[k])$ contains both position and velocity information, every edge $(i,j) \in \mathcal{E}$ in multi-agent systems should have two different adjacency weights, position-dependent weight a_{ij}^q and velocity-dependent weight a_{ij}^p, respectively. Therefore, the flocking control protocol can be augmented as

$$
\tilde{u}_i = c^\alpha \sum_{j \in N_i} \left[-\mathbf{n}_{ij} \phi_\alpha \left(\left\| q_j - q_i \right\|_\sigma, a_{ij}^q \right), + a_{ij}^p (p_j - p_i) \right] - c_1^\gamma (p_r - p_i) - c_2^\gamma (q_r - q_i). \tag{3.17}
$$

In addition, a_{ij}^q and a_{ij}^p are calculated by modifying the adjacency bump function in (3.15), which replaces h by h_{ij}^q or h_{ij}^p. In detail, h_{ij}^q and h_{ij}^p are defined as

$$h_{ij}^s = \left(1 - \frac{\left\| s_j - s_i^* \right\|}{2d_r} \right) \left| \cos \frac{\theta_{ij}^s}{2} \right|, j \in N_i, \tag{3.18}$$

in which s is either q or p, and $\theta_{ij}^s \in []0, 2\pi$ is the angle between s_j and s_i^*. In (3.18), the differences of distance and orientation between s_j and s_i^* is used to determine the values of h_{ij}^s. When s_j is closer to s_i^*, a larger h_{ij}^s is produced to give a larger a_{ij}^s to strength the position-dependent or velocity-dependent adjacency weights between α-agent j and α-agent i, which make states of α-agent i approach to s_i^*. Otherwise, a smaller a_{ij}^s is produced.

3.2.3   Simulation Results and Discussions

In this section, simulations are conducted in MATLAB® to verify the performance of the proposed DFS algorithm. Note that all values used in simulations only have numerical meaning, so that there is no physics unit for all parameters and variables. In the simulations, ten α-agents are randomly initialized in a 2-dimensional spatial box $(0, 60) \times (0, 60)$ with zero velocity. The unique virtual leader of the group of agents is set to move along a straight line with the constant velocity vector $[3, 0]^{\mathrm{T}}$, which starts from the position $(60, 30)$. In addition, the lattice scale d is 3, and the interaction region d_r is 5.1, which satisfies the condition $d_r \in (d, \sqrt{3}d)$.

Two cases are studied. The first case (Case 1) uses the conventional flocking control, which is only steered by the flocking control protocol introduced in (3.14) with the adjacency bump function in (3.15), where h is 0.3. The second case (Case 2) employs the DFS algorithm with the same initial condition of Case 1. In addition,
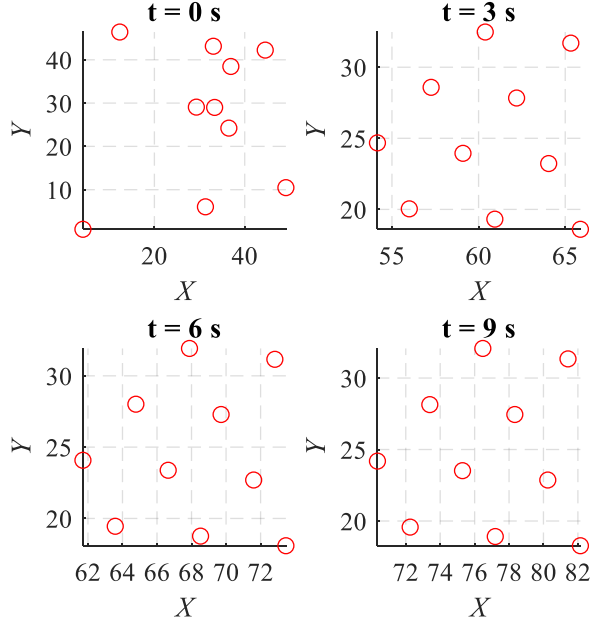
Figure 4. Flocking movement in Case 1.

the augmented flocking control protocol in (3.17) with the modified adjacency bump function is used in Case 2. Results are shown in Fig. 4, 5, 6, 7, and 8.

The flocking movements of the group of agents are presented in Fig. 4 and Fig. 5. With the same initial condition, both Case 1 and Case 2 can achieve the flocking formation pattern and track the virtual leader, and the desired lattice scale is kept once the flocking is formed. Thus, the DFS algorithm does not impair the satisfactions of the flocking rules and virtual leader tracking.

The velocity consensus performances of the flocks are shown in Fig. 6, where p_x and p_y denote the velocity of agents along X and Y direction, respectively. The groups of agents in both Case 1 and Case 2 can successfully track the virtual leader velocity vector. However, the velocity consensus is achieved around 2.5 s in Case 2 as implied by the consensus point (solid red circle) in Fig. 6 (c) and (d), which is achieved in
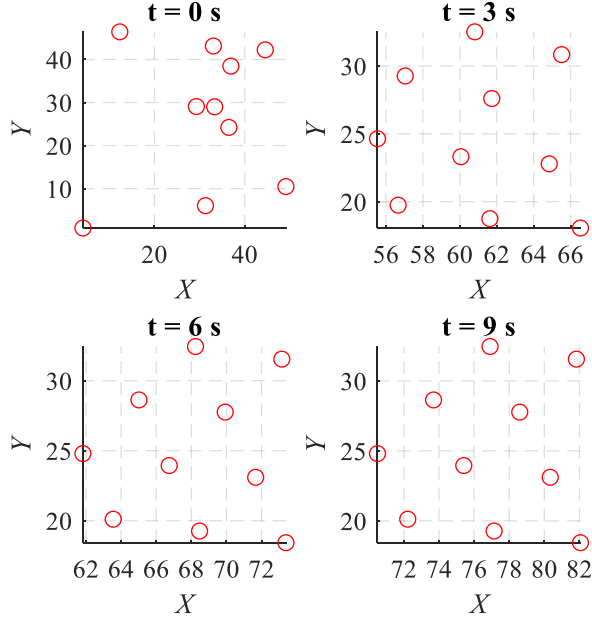
Figure 5. Flocking movement in Case 2.

Case 1 around 5 s as indicated in Fig. 6 (a) and (b). Thus, the DFS algorithm can successfully speed up the flocking velocity consensus. In Fig. 7, u_x and u_y denote the control inputs of every agent along X and Y direction, respectively. Similar to velocity consensus, the control inputs in Case 2 also have faster convergence speed. In addition, the magnitude of control inputs in Case 2 is even less than the ones in Case 1. Hence, the DFS algorithm does not demand larger control inputs.

The flocking convergence performance with the DFS algorithm is also directly demonstrated through the disagreement function (Hamiltonian) in Fig. 8, which plots the time history of the Hamiltonian of the whole multi-agent system. Before 1.04 s, the disagreement function in both Case 1 and Case 2 shows a trend for growth till the peak value, 1892. Then, the disagreement function in two cases starts to decrease, and the decision value, 480, is gradually achieved. From two zoom-in plots in Fig. 8,

35
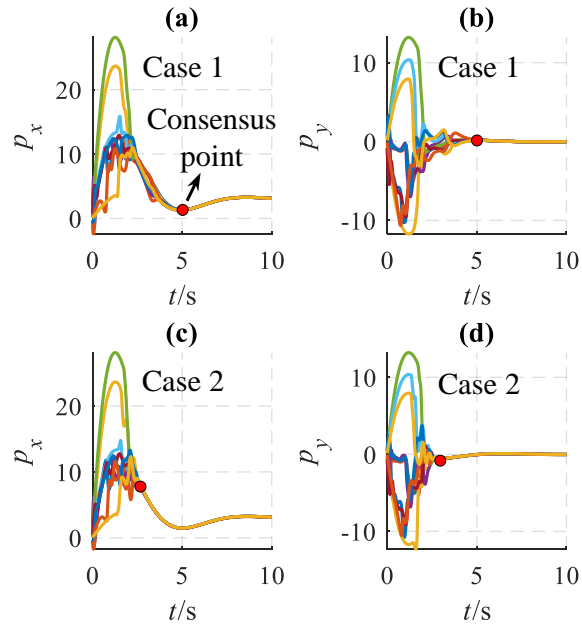
Figure 6. Velocity consensus results in flocking.
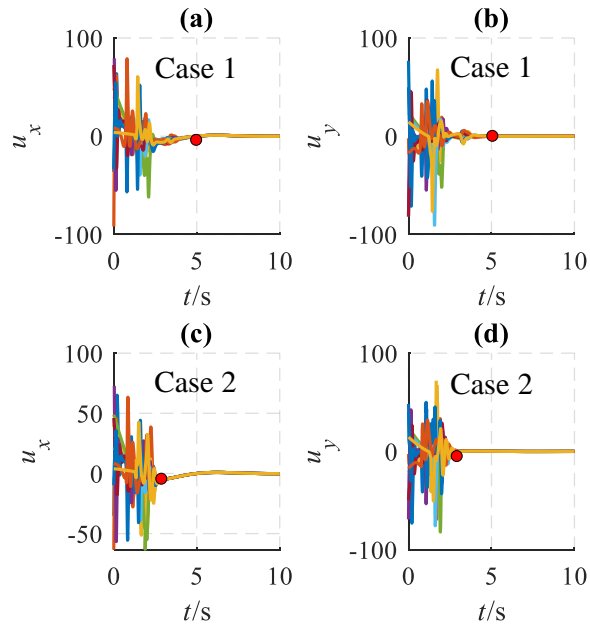
Figure 7. Control inputs results in flocking.
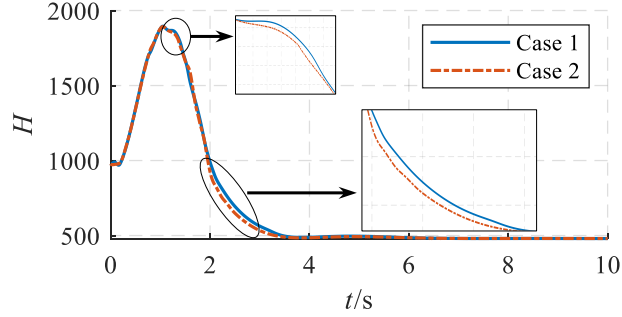
Figure 8. Hamiltonian results in flocking.

a faster negative decrease rate can be observed, which confirms the DFS algorithm can help to achieve desired flocking consensus faster.

3.2.4 Conclusions

The D-PFC and the DFS algorithm are proposed to achieve the fast-convergence flocking control of second-order multi-agent systems with the switching communication topology. Demonstrated by two numerical cases study, simulation results show that the group of agents steered by the augmented flocking control protocol with the DFS algorithm can successfully accelerate the flocking control speed without demanding larger control inputs.

3.3 Flocking Control of Multi-Agent Systems with Permanent Obstacles in Strictly Confined Environments

In the existing flocking studies, free flocking without obstacles is a dominated scenario as indicated in Fig. 9 (a) (Reynolds 1987; Su, Wang, and Lin 2009; Tanner, Jadbabaie, and Pappas 2003). In some other flocking scenarios with obstacle avoidance,

37

the obstacles are typically considered as temporary objects that only have transient interactions (repulsive forces) with respect to flocking agents (Olfati-Saber 2006; Khatib 1986). For example, two different types of temporary obstacles, a black ellipse in front of agents and two boundaries of a confined space that are close to agents, are shown in Fig. 9 (b) and (c), respectively. These obstacles, which only interact partial agents temporarily (labeled by red color), are usually modeled as temporary spatio-temporal constraints. All of the flocking agents are not directly influenced by obstacles at one time (Vásárhelyi et al. 2018). Therefore, after the flocking agents bypass (see Fig. 9 (b)) or depart away from (see Fig. 9 (c)) the temporary obstacles, the influences of obstacles are not considered and discussed in any final equilibrium of flocking dynamics for multi-agent systems (Olfati-Saber 2006; Khatib 1986).

Although a free flocking and/or temporary obstacles may be sufficiently assumed in nature or in sensing networks (Olfati-Saber 2006; Liu and Xu 2015), these assumptions can fail or even be impossible in some engineering applications of artificial multi-agent systems. One notable example is that the road boundaries cannot be taken as temporary constraints of vehicular agents in transportation systems considering traffic safety (Iftekhar and Olfati-Saber 2012). Furthermore, the vascular walls of human blood vessels, in which a group of micro-robots is manipulated, cannot be viewed as temporary obstacles as well (Jeon et al. 2010). For the road boundaries and vascular walls, persistent interactions on all of the (vehicular and robotic) agents would perform all the time for safety considerations.

Permanent obstacles are defined as obstacles or boundaries that persistently interact with agents all the time in the process of flocking coordination in this section. The permanent obstacles could be generated or defined by different situations, such
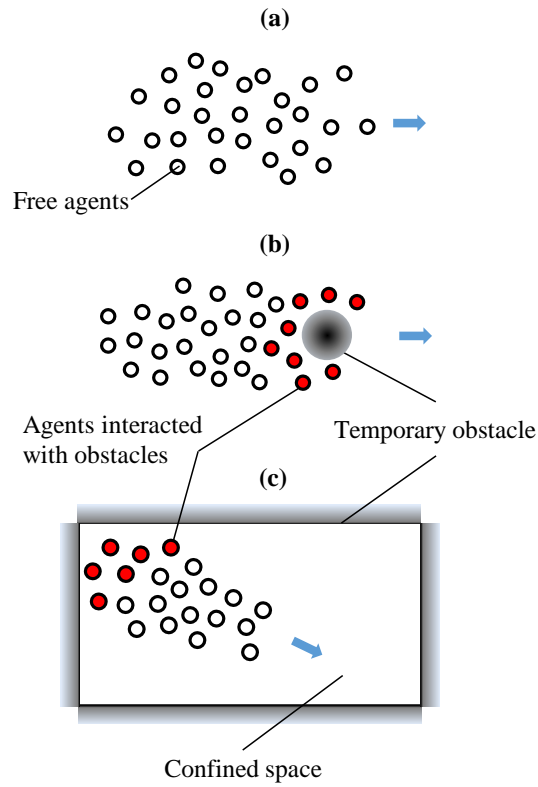
Figure 9. Flocking scenarios without obstacles or with temporary obstacles (boundaries) that only interact with partial agents (labeled by red color) for a period of time.
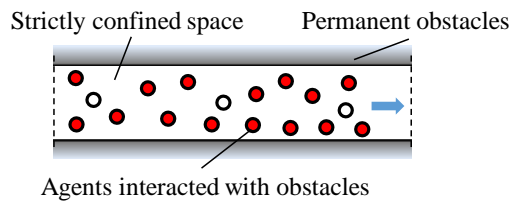
Figure 10. Flocking interactions with permanent obstacles (boundaries) that interact with all of the agents all the time in a strictly confined space.

as a group of agents moving in a strictly confined environment. The strictly confined environment makes the constrained multi-agent systems interacted with boundaries all the time as long as they are moving in the space. Therefore, the boundaries of the strictly confined environment could be considered as permanent obstacles. An example of the strictly confined environment is presented in Fig. 10, in which all of the agents are controlled in a limited tube-like space to satisfy all the required flocking rules.

Motivated by the aforementioned problem, this section seeks to generalize and extend the existing flocking theory for the cooperative control of multi-agent systems with permanent obstacles in strictly confined environments.

3.3.1 Flocking Behaviors with Temporary Obstacles

In literature, a general cooperative control problem of multi-agent systems, such as formation and clumping control, can be formulated as an optimization problem, in which the control law attempts to minimize a cost function iteratively to achieve control objectives (Nedic and Liu 2018; Nedic and Ozdaglar 2009). Inspired by this idea, the cooperative control of flocking coordination was solved by optimization techniques to adapt to large-scale complicated scenarios (Yu, Chen, and Cao 2010; Zhang et al. 2019). In this section, we also take the merits of the optimization paradigm to appraise flocking behaviors to expand the following discussions.

In details, the Hamiltonian in (2.8) is adopted as the cost function of the optimization problem for flocking control since its minima represent the satisfaction of flocking rules, which is analyzed in the remainder of this section. Furthermore, the flocking control protocol is the searching strategy to solve the optimization problem.

40

Hence, the flocking optimization problem is established in (3.19).

$$\begin{aligned} \min_{q,p} \quad & H(q,p) \\ \text{s.t.} \quad & q, p \in \mathbb{R}^{mn} \end{aligned} \tag{3.19}$$

The set of optimal solution of (3.19) is written in (3.20), which ensures the minimum of H, denoted as H^*.

$$S = \left\{ (q^*, p^*) \,\middle|\, \arg\min_{q,p \in \mathbb{R}^{mn}} H(q,p) \right\}. \tag{3.20}$$

For free flocking or flocking with only temporary obstacles, the relationship between the local minima of all energy sub-terms in H and the satisfactions of corresponding flocking rules are discussed in Lemma 3.3.1, 3.3.2, 3.3.3, and 3.3.4 as follows.

Lemma 3.3.1. *The flocking rules on the cohesion and separation of α-agents are achieved at $\left\|q_j - q_i\right\|_\sigma = \left\|d\right\|_\sigma, \forall i \in \mathcal{V}, j \in N_i \neq \varnothing$ if and only if $V_\alpha = 0$ in (2.11).*

Proof. On the one hand, the flocking rules on the cohesion and separation of α-agents means that every α-agent keeps $\left\|d\right\|_\sigma$ with each neighbor in N_i, namely $\left\|q_j - q_i\right\|_\sigma = \left\|d\right\|_\sigma, \forall i \in \mathcal{V}, j \in N_i \neq \varnothing$. Therefore, from (2.11), the lower limit of the integral, $\left\|d\right\|_\sigma$, equals to its upper limit, $\left\|q_j - q_i\right\|_\sigma$, so that $V_\alpha = 0$.

On the other hand, based on (2.13), we have the definite integral $\int_{\left\|d\right\|_\sigma}^{\left\|q_j - q_i\right\|_\sigma} \phi_\alpha(x)\mathrm{d}x \geq 0$, which makes $V_\alpha = 0$ if and only if the definite integral equals to zero. If $V_\alpha = 0$, there are two cases. The first case is $\phi_\alpha = 0$ resulted from $\left\|q_j - q_i\right\|_\sigma \geq \left\|r\right\|_\sigma$, which makes $N_i = \varnothing, \forall i \in \mathcal{V}$. However, the set of neighbors of α-agent i should not be empty regarding the requirements of cohesion. The second case is $\left\|q_j - q_i\right\|_\sigma = \left\|d\right\|_\sigma$, which satisfies the flocking rules on cohesion and separation. $\square$

Lemma 3.3.2. *The flocking rules on the alignment and speed tracking of the (virtual) γ-agent are achieved at $p_i = p_r, \forall i \in \mathcal{V}$ if and only if $K = 0$ in (2.9) .*

Proof. On the one hand, the flocking rules on the alignment and speed tracking of the (virtual) γ-agent means that every α-agents has the same velocity as the γ-agent, namely $p_i = p_r$. Substituting $p_i = p_r$ into (2.9), we have $K = 0$.

On the other hand, owing to the quadratic form of the kinetic energy in (2.9), $K = 0$ gives $p_i = p_r$. $\square$

Lemma 3.3.3. *The flocking rule on the avoidance of temporary obstacles is achieved at $\left\|\hat{q}_{i,k} - q_i\right\|_\sigma \geq \left\|\hat{d}\right\|$, namely, $\phi_\beta = 0, \forall k \in N_i^\beta, i \in \mathcal{V}$ if and only if $V_\beta = 0$ in (2.16).*

Proof. On the one hand, the flocking rule on the avoidance of temporary obstacles means that the distance from every α-agent to β-agents is larger than $\left\|\hat{d}\right\|_\sigma$, which results in $\phi_\beta = 0, \forall k \in N_i^\beta, i \in \mathcal{V}$. Substituting $\phi_\beta = 0$ into (2.16), we have $V_\beta = 0$.

On the other hand, based on (2.17), we have the definite integral $\int_{\|\hat{d}\|_\sigma}^{\left\|\hat{q}_{i,k} - q_i\right\|_\sigma} \phi_\beta(x)\mathrm{d}x \geq 0$, which makes $V_\beta = 0$ if and only if the definite integral equals to zero. If $V_\beta = 0$, there are two cases. The first case is $\left\|\hat{q}_{i,k} - q_i\right\|_\sigma = \left\|\hat{d}\right\|_\sigma$ to provide the same limits of the definite integral. The second case is $\left\|\hat{q}_{i,k} - q_i\right\|_\sigma \geq \|d\|_\sigma$, which makes $\phi_\beta = 0$. Both cases satisfy the flocking rule on the avoidance of temporary obstacles. $\square$

Lemma 3.3.4. *The flocking rule on the position tracking of α-agents with respect to the γ-agent is achieved if and only if $V_\gamma = V_\gamma^* > 0$ in (2.19), in which V_γ^* denotes the value of V_γ at its local minima.*

Proof. The quadratic form of (2.19) makes the values of V_γ non-negative. However, V_γ cannot be zero since it is impossible for all α-agents to locate at p_r simultaneously, namely $p_i = p_r, \forall i \in \mathcal{V}$, which violates the flocking rules on cohesion and alignment. Therefore, the flocking rule on the position tracking of α-agents with respect to the γ-agent is achieved whenever $V_\gamma = V_\gamma^* > 0$. $\square$

Based on the above discussions and summaries in Lemma 3.3.1, 3.3.2, 3.3.3, and 3.3.4, Theorem 3.3.1 is provided to characterize the set of local minima of H for flocking with temporary obstacles, which was only partially implied in literature (Reza Olfati-Saber and R. M. Murray 2003), but now is rephrased in the context of the optimization problem (3.19) and (3.20).

Theorem 3.3.1 (Flocking with temporary obstacles). *For a multi-agent system that obeys certain flocking rules, e.g. the cohesion, separation, alignment, avoidance of temporary obstacles, position and speed tracking of a (virtual) objective, every local minimum of the associated H satisfies the set of flocking rules, and vice versa.*

Proof. Based on the inequalities in (2.9), (2.11), (2.16), and (2.19), we have

$$H \geq V_\gamma^*, \forall t > 0. \tag{3.21}$$

In addition, by utilizing the summarized properties in Lemma 3.3.1, 3.3.2, 3.3.3, and 3.3.4 between the satisfaction of flocking rules and the values of K, V_α, V_β, and V_γ, $H = V_\gamma^*$ implies K, V_α, V_β, and $V_\gamma = 0$. Therefore, the minimization of the Hamiltonian obtains a set of local minima with the same value V_γ^*, which represents the achievement of the desired flocking rules of the multi-agent system. Namely, S in (3.20) can be rewritten as (3.22).

$$S = \left\{ (q^*, p^*) \in \mathbb{R}^{mn} \times \mathbb{R}^{mn} : H = V_\gamma^* \right\}. \tag{3.22}$$

Therefore, the sufficiency is proved.

For the necessity, if the required flocking rules are satisfied, the local minima of K, V_α, V_β, and V_γ are all achieved. Based on (2.8) and (2.10), the combination of the local minima of K, V_α, V_β, and V_γ is also a local minimum of the corresponding H. Thus, the necessity is proved. □

Based on Theorem 3.3.1, we have the following corollary for free flocking, which can be understood as a specific case in Theorem 3.3.1.

Corollary 3.3.1 (Free flocking). *For a multi-agent system that obeys the set of flocking rules described in Theorem 3.3.1 without requiring obstacle avoidance, every local minimum of the associated H satisfies the set of flocking rules, and vice versa.*

Proof. Without considering obstacle avoidance, the inequality in (3.21) is still held since temporary obstacles do not exist in any equilibrium of H. Based on (2.16), $V_\beta = 0$ since there is no obstacle. Employing the same proof process of Theorem 3.3.1, $H = V_\gamma^*$ also indicates free flocking phenomena without obstacles. The necessity can be similarly proved as well through the counterpart in Theorem 3.3.1. $\square$

Actually, Theorem 3.3.1 and Corollary 3.3.1 do not provide any surprising results of flocking coordination compared with some existing conclusions, such as Theorem 2 and Theorem 5 in (Olfati-Saber 2006), but reveal the characteristics of H in the optimization paradigm. Essentially, the optimization of H is not a convex optimization problem since there are multiple local minima. However, due to the following aspects, the nonconvex optimization problem can still be resolved via convex optimization techniques. First, the Hamiltonian H is as the summation of K, V_α, V_β, and V_γ by utilizing relative distances and speeds among α, β, and γ agents. Hence, H is translation-invariant and has a set of equilibrium points with the same value. For free flocking or flocking with temporary obstacles, the minimum value of H is V_γ^*, which represents the achievement of the flocking rules. Second, it is acceptable that H approaches any local minimum for the desired flocking coordination by given certain initial and boundary conditions. Therefore, the control protocol for flocking with temporary obstacles or free flocking can be effectively and directly determined through

convex optimization techniques (Boyd and Vandenberghe 2004; Nedic and Ozdaglar 2009). That is why the gradient decent method can be used in this section to derive the flocking control input u_i, $\forall i \in \mathcal{V}$ in (3.23) to iteratively find local minimum of H, which is similar to other classic flocking control protocols in (Arcak 2007; Olfati-Saber 2006; Su, Wang, and Lin 2009).

$$
\begin{aligned}
u_i &= -\nabla_{q_i,p_i} H \\
&= \underbrace{(-\nabla_{q_i} V_\alpha)}_{f_i^\alpha} + \underbrace{(-\nabla_{q_i} V_\beta)}_{f_i^\beta} + \underbrace{(-\nabla_{q_i} V_\gamma - \nabla_{p_i} K)}_{f_i^\gamma},
\end{aligned} \tag{3.23}
$$

where

$$
\nabla_{q_i} V_\alpha(q) = -c^\alpha \sum_{j \in N_i^\alpha} \mathbf{n}_{ij} \phi_\alpha \left(\left\| q_j - q_i \right\|_\sigma \right), \tag{3.24}
$$

$$
\nabla_{q_i} V_\beta(q) = -c^\beta \sum_{k \in N_i^\beta} \hat{\mathbf{n}}_{i,k} \phi_\beta \left(\left\| \hat{q}_{i,k} - q_i \right\|_\sigma \right), \tag{3.25}
$$

$$
\nabla_{q_i} V_\gamma(q) = c_2^\gamma (q_i - q_r), \tag{3.26}
$$

$$
\nabla_{p_i} K(p) = c_1^\gamma (p_i - p_r). \tag{3.27}
$$

In (3.23), f_i^α is the control effort to regulate the desired lattice geometry without collision among α-agents, f_i^β is the repulsive force for the obstacle avoidance, and f_i^γ is the navigational term to collectively enable the (virtual) objective position and speed tracking. In (3.24) and (3.25), $\mathbf{n}_{ij}$ is the unit vector along the line connecting q_i and q_j, and $\hat{\mathbf{n}}_{i,k}$ is the unit vector along the line connecting q_i and $\hat{q}_{i,k}$.

3.3.2 Flocking Behaviors with Interactions with Permanent Obstacles

Beyond the temporary obstacles, the avoidance of permanent obstacles, which could be generated by strictly confined working spaces in some engineering applications, has

to be addressed as well in flocking control. Similar to temporary obstacles, permanent obstacles are also assumed as static without loss of generality so that the definition of β-agents in (2.18) still can be applied. However, H containing V_β in (2.16) cannot be solely used to evaluate the avoidance of permanent obstacles of α-agents as elaborated in Theorem 3.3.2.

In a strictly confined space, the boundaries (serving as permanent constraints or obstacles) always have influences on α-agents during and after a flocking process, namely $\left\|\hat{q}_{i,k} - q_i\right\|_\sigma < \left\|\hat{d}\right\|_\sigma$ for all $t > 0$. Hence, based on the discussion in 4), V_β in (2.16) can never reach zero. In this situation, permanent obstacles are avoided only when $V_\beta = V_\beta^*$ is held, where $V_\beta^* > 0$ is the optimal value at the local minima of V_β with permanent constraints. Therefore, the inequality (3.21) has to be rewritten as (3.28) for flocking with permanent obstacles.

$$H \geq V_\gamma^* + V_\beta^*, \forall t > 0. \tag{3.28}$$

The following Theorem 3.3.2 provides the properties of the Hamiltonian accommodating interactions from permanent obstacles. Based on Theorem 3.3.2, the obstacle zero-sum condition is proposed to fulfill the new requirements of flocking control with permanent obstacles in a strictly confined environment.

Theorem 3.3.2 (Flocking with permanent obstacles). *Let a multi-agent system obey a set of flocking rules including cohesion, separation, alignment, position and speed tracking of a virtual leader, and obstacle avoidance in a strictly confined space. Then, the set of flocking rules is satisfied if and only if the Hamiltonian H achieve the local minima with the obstacle zero-sum condition in (3.29).*

$$\sum_{k \in N_i^\beta} \hat{\mathbf{n}}_{i,k} \phi_\beta\left(\left\|\hat{q}_{i,k} - q_i\right\|_\sigma\right) = 0, \forall i \in \mathcal{V}. \tag{3.29}$$

Proof. According to (3.28), the achieved local minima of H can be defined in the set of the configuration and velocity of α-agents in (3.30), where the equality in (3.28) is held.

$$S = \left\{ (q^*, p^*) \in \mathbb{R}^{mn} \times \mathbb{R}^{mn} : H = V_\gamma^* + V_\beta^* \right\}. \tag{3.30}$$

Next, we are going to prove that only the local minima in (3.30) with the satisfied obstacle zero-sum condition (3.29) can assure the set of flocking rules including permanent obstacle avoidance. For the local minima of H, the corresponding gradient is zero, presented in (3.31).

$$\nabla H = \nabla_q V_\alpha + \nabla_q V_\beta + \nabla_q V_\gamma + \nabla_p K = \mathbf{0}_{n \times 1}. \tag{3.31}$$

For flocking with temporary obstacles, ∇H will asymptotically go to zero since $\nabla_q V_\alpha$, $\nabla_q V_\beta$, $\nabla_q V_\gamma$, and $\nabla_p K$ will approach to $\mathbf{0}_{n \times 1}$ by applying the gradient-based flocking control protocol in (3.23). In particular, $\nabla_q V_\beta$ converges to $\mathbf{0}_{n \times 1}$ once the influences of temporary obstacles disappear. Namely, $\left\| \hat{q}_{i,k} - q_i \right\|_\sigma \geq \left\| \hat{d} \right\|_\sigma$ for all $i \in \mathcal{V}$ and $k \in N_i^\beta$ makes $\phi_\beta \left(\left\| \hat{q}_{i,k} - q_i \right\|_\sigma \right) = 0$, which makes the equality in (3.32) held by substituting (3.25).

$$\nabla_q V_\beta = \sum_{i \in \mathcal{V}} \nabla_{q_i} V_\beta(q) = \mathbf{0}_{n \times 1}. \tag{3.32}$$

In sum, there are generally no interactions between α-agents and temporary obstacles in any equilibrium (local minimum) of H. In other words, temporary obstacles will disappear after the desired flocking pattern (lattice) is formed.

Nevertheless, when permanent obstacles, namely the boundaries or constraints of the strictly confined space, are considered, the condition $\left\| \hat{q}_{i,k} - q_i \right\|_\sigma \geq \left\| \hat{d} \right\|_\sigma$ cannot be satisfied for all $t > 0$. Hence, it is implausible to have $\phi_\beta \left(\left\| \hat{q}_{i,k} - q_i \right\|_\sigma \right) = 0$ for all $t > 0$ to make $\nabla_q V_\beta = \mathbf{0}_{n \times 1}$. For permanent obstacle avoidance, an alternative situation to still make $\nabla_q V_\beta = \mathbf{0}_{n \times 1}$ is that for any α-agent i, we have the summation in (3.25) equal to zero, which is defined as the obstacle zero-sum condition in (3.29).

The proof of the converse can be completed in a reverse way and omitted for simplicity. $\square$

The obstacle zero-sum condition in (3.29) indicates that the resultant influence of neighbored obstacles in N_i^β of α-agent i is zero. Therefore, the obstacle zero-sum condition can be recognized as a new flocking rule to avoid reaching undesirable local minima that cannot satisfy the obstacle zero-sum condition, which specifically works for flocking control with permanent obstacles or in a strictly confined environment. The existence of the solutions to satisfy the obstacle zero-sum condition is proved as follows.

In the obstacle zero-sum condition, $\hat{\mathbf{n}}_{i,k}$ is defined as

$$\hat{\mathbf{n}}_{i,k} = \frac{\hat{q}_{i,k} - q_i}{\sqrt{1 + \sigma \left\| \hat{q}_{i,k} - q_i \right\|^2}}. \tag{3.33}$$

Substituting (3.33) into (3.29), we have

$$\sum_{k \in N_i^\beta} \frac{\hat{q}_{i,k} - q_i}{\sqrt{1 + \sigma \left\| \hat{q}_{i,k} - q_i \right\|^2}} \phi_\beta \left(\left\| \hat{q}_{i,k} - q_i \right\|_\sigma \right) = 0, \tag{3.34}$$

which results in

$$\sum_{k \in N_i^\beta} \hat{q}_{i,k} \phi'_\beta \left(\left\| \hat{q}_{i,k} - q_i \right\| \right) = q_i \sum_{k \in N_i^\beta} \phi'_\beta \left(\left\| \hat{q}_{i,k} - q_i \right\| \right), \tag{3.35}$$

where

$$\phi'_\beta \left(\left\| \hat{q}_{i,k} - q_i \right\| \right) = \frac{\phi_\beta \left(\left\| \hat{q}_{i,k} - q_i \right\|_\sigma \right)}{\sqrt{1 + \sigma \left\| \hat{q}_{i,k} - q_i \right\|^2}}. \tag{3.36}$$

Therefore, based on (3.35), given certain permanent obstacles (β-agents), the existence of solutions for the obstacle zero-sum condition implies that there is a solution of (3.37).

$$q_i = \frac{\sum_{k \in N_i^\beta} \hat{q}_{i,k} \phi'_\beta \left(\left\| \hat{q}_{i,k} - q_i \right\| \right)}{\sum_{k \in N_i^\beta} \phi'_\beta \left(\left\| \hat{q}_{i,k} - q_i \right\| \right)}. \tag{3.37}$$

With permanent obstacles, N_i^β is not an empty set. Namely, the denominator in the right-hand-side of (3.37) cannot be zero, such that the solution of q_i exists with permanent obstacles.

Remark 3.3.1. The obstacle zero-sum condition provides us a new tool to completely describe flocking phenomena with permanent obstacles. However, the obstacle zero-sum condition is not required to be satisfied all the time as long as it is achieved on the final equilibrium of H.

Indicated by Theorem 3.3.2, the relationship between $V_\beta(q)$ and the obstacle zero-sum condition in (3.29) is depicted in Corollary 3.3.2.

Corollary 3.3.2. *Considering $V_\beta(q)$ is the obstacle potential energy of a multi-agent system with permanent obstacles, $V_\beta(q) = V_\beta^*$ is obtained if and only if the obstacle zero-sum condition is satisfied.*

Proof. The corollary is readily obtained based on the proof process of Theorem 3.3.2. □

3.3.3   Novel Flocking Control Algorithm for Permanent Obstacles

In free flocking or flocking with temporary obstacles, Theorem 3.3.1 and Corollary 3.3.1 imply that it is suitable to use the conventional Hamiltonian depicted in (2.8) to develop flocking control protocols via the classic gradient descent method. In particular, the gradient-based term f_i^β in (3.23) generates a repulsive force normal to the surfaces of temporary obstacles to keep α-agents away. However, flocking control with permanent obstacles cannot formulate an optimization problem using H in (2.8). Theorem 3.3.2 implies that with the interactions from permanent obstacles, there

are two types of local minima of H: local minima satisfying and unsatisfying the obstacle zero-sum condition. Namely, not all of the local minima of H can satisfy the obstacle zero-sum condition in (3.29). As a result, H in (2.8) cannot evaluate flocking behaviors with permanent obstacles anymore, and the gradient descent method cannot guarantee an appropriate local minimum of H, which also satisfies the obstacle zero-sum condition.

A novel augmented Hamiltonian will be proposed to consider the obstacle zero-sum condition in this section, and a new flocking control protocol is developed by using the augmented Hamiltonian.

The Hamiltonian in (2.8) is augmented to $\hat{H}$ in (3.38) when the obstacle zero-sum condition is considered.

$$\hat{H} = H + H_\beta, \tag{3.38}$$

where H_β, defined in (3.39), is a new potential energy term to evaluate the resultant forces of (permanent) β-agents on α-agents.

$$H_\beta = \sum_{i \in \mathcal{V}} \left\| H_\beta^i \right\|_\sigma \geq 0, \tag{3.39}$$

in which

$$H_\beta^i = \sum_{k \in N_i^\beta} \hat{\mathbf{n}}_{i,k} \phi_\beta \left(\left\| \hat{q}_{i,k} - q_i \right\|_\sigma \right). \tag{3.40}$$

Intuitively, $H_\beta = 0$ when the obstacle zero-sum condition is achieved. Based on the proof of Theorem 3.3.2, the new equilibrium points of $\hat{H}$, denoted as $(\hat{q}^*, \hat{p}^*)$, is a selection of the equilibrium points of H in (3.30) that satisfy the obstacle zero-sum condition.

Using (3.38), the gradient decent method could be applied to develop a new flocking control algorithm based on the newly augmented Hamiltonian. The resulted

augmented flocking control protocol is first presented in (3.41).

$$\hat{u}_i = f_i^\alpha + f_i^\beta + h_i^\beta + f_i^\gamma, \tag{3.41}$$

where h_i^β is defined in (3.42) that represents the force steering multi-agent systems to satisfy the obstacle zero-sum condition.

$$h_i^\beta = -\nabla_{q_i} H_\beta = -\nabla\sigma(H_\beta^i), \tag{3.42}$$

in which $\nabla\sigma$ is the gradient of σ-norm that is described in (3.43).

$$\nabla\sigma(z) = \frac{z}{1 + \sigma\|z\|_\sigma}. \tag{3.43}$$

The relationship between the augmented Hamiltonian, $\hat{H}$, and the set of flocking rules including permanent obstacle avoidance is described in the following Theorem 3.3.3.

Theorem 3.3.3 (Augmented Hamiltonian). *For a multi-agent system that obeys a set of flocking rules, e.g. cohesion, separation, alignment, position and speed tracking of a virtual leader, and permanent obstacle avoidance, every local minimum of the associated augmented Hamiltonian $\hat{H}$ defined in (3.38) indicates the satisfaction of the set of flocking rules, and vice versa.*

Proof. Based on the inequalities of (3.28) and (3.39), and the equation (3.38), we have

$$\hat{H} \geq V_\gamma^* + V_\beta^*, \forall t > 0. \tag{3.44}$$

Therefore, the set of configurations and velocities of α-agents defined in (3.45) is the group of all the local minim of $\hat{H}$.

$$\hat{S} = \left\{ (\hat{q}^*, \hat{p}^*) \in \mathbb{R}^{mn} \times \mathbb{R}^{mn} : \hat{H} = V_\gamma^* + V_\beta^* \right\}. \tag{3.45}$$

Indicated by Theorem 3.3.2, the condition $V_\beta = V_\beta^*$ is held if and only if the obstacle zero-sum condition is satisfied ($H_\beta = 0$). Therefore, all members (q^*, p^*) in $\hat{S}$ meet the requirements of all the flocking rules including permanent obstacle avoidance.

The proof of the converse can be completed in a reverse way and is omitted for simplicity. $\qquad\qquad\square$

Remark 3.3.2. Actually, compared with H, the augmented Hamiltonian $\hat{H}$ does not create new equilibrium points but helps to select a group of equilibrium points that satisfy the obstacle zero-sum condition. Namely, $\hat{S}$ in (3.45) is a subset of S in (3.30). Therefore, the conclusions from the convergence and stability analysis of H in existing literature still can be applied to $\hat{H}$.

3.3.4 Simulation Results and Discussions

Simulation results are obtained through MATLAB® to verify and compare the proposed augmented flocking control design for permanent obstacles. In this section, a CAV system within a three-lane freeway environment is studied, which is a tube-like 2D strictly confined space as depicted in Fig. 11.

Five indistinctive α-agents (vehicles), V1-V5, are initialized with random positions (X, Y) between two straight road boundaries, which are recognized as two neighboring obstacle profiles O_k to generate permanent obstacles (β-agents). The area between two permanent road boundaries is defined as the feasible space for the flocking control of α-agents. In this situation, α-agents always interact with β-agents in the feasible space. Note that β-agents are continuously determined based on the changing positions of α-agents. Implied in Fig. 11, because O_k are two parallel straight road boundaries,
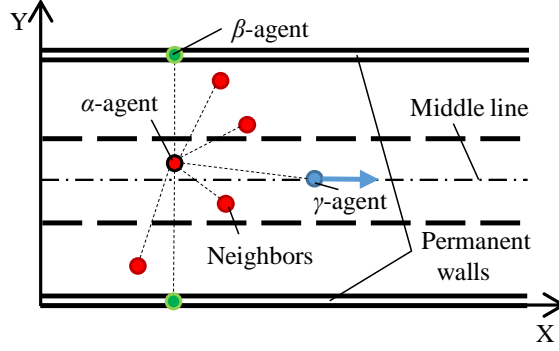
Figure 11. A 2D strictly confined three-lane freeway environment with the α-agents (vehicles), β-agents(permanent road boundaries), and γ-agent (virtual leader).

β-agents of an α-agent at one time are always two perpendicularly projected points on the road boundaries with respect to the α-agent. Moreover, five α-agents are commanded to track a navigational virtual leader γ-agent moving along the middle line of the middle lane at $Y = 4.5$ m with a fixed speed of 20 m/s. Thus, five α-agents are expected to achieve the desired lattice along the middle line. Regarding the targeted driving speed, the lattice scale d among vehicles is set as 30 m to keep traffic safety. In addition, given the lattice ratio $\kappa = 1.6$, the interaction range r of α-agents is 48 m.

Two different simulation cases are studied for comparison. The first case is that the augmented flocking control protocol specifically developed for permanent obstacles is applied. The second case is that the existing classic flocking algorithm without considering permanent obstacles (e.g. the flocking design in (Olfati-Saber 2006)) is applied with the same initial conditions of the first case. The simulation results of the first case are presented in Fig. 12 and Fig. 13, and the simulation results of the second case are presented in Fig. 14 and Fig. 15. Furthermore, to explain the dynamic behaviors of vehicles, the responses of the lateral control input of V1 is illustrated in Fig. 16, and the responses of the Hamiltonian H and H_β are presented in Fig. 17.
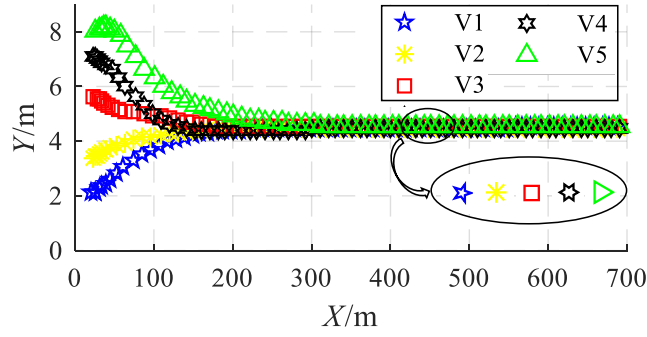
Figure 12. Maneuvers of α-agents with the augmented flocking control protocol.
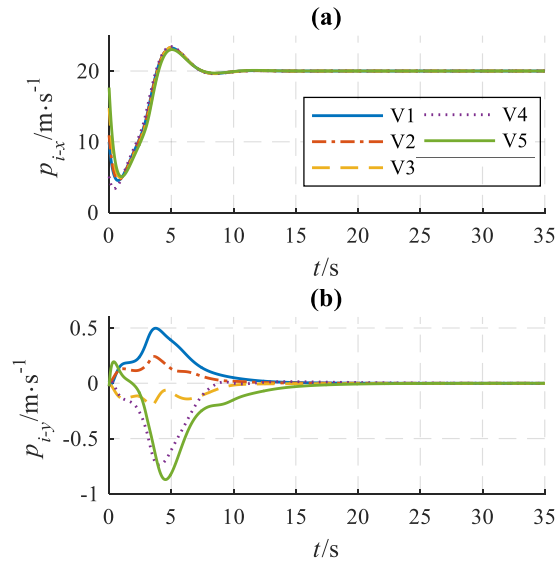
Figure 13. Longitudinal and lateral velocity trajectories of α-agents with the augmented flocking control protocol.

From the maneuvers of α-agents with the augmented flocking control protocol, as shown in Fig. 12, all α-agents are constrained within the feasible space, and the desired lattice is successfully formed along the middle line to track the common virtual leader, γ-agent. Moreover, the zoom-in circle also indicates that there is no collision during the process. From Fig. 13, the longitudinal and lateral speeds of α-agents, p_{i-x} and p_{i-y}, also asymptotically converge to the anticipated values. Therefore, the full set

54
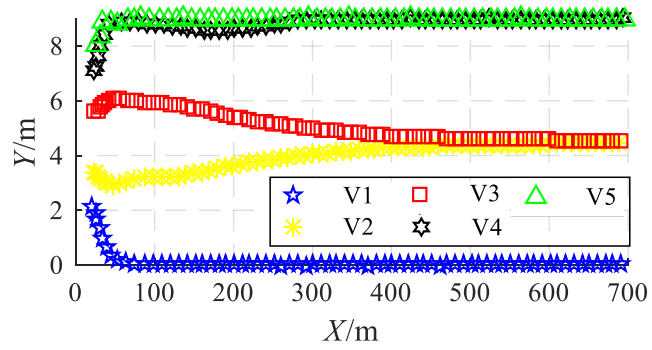
Figure 14. Maneuvers of α-agents with the classic flocking control protocol.
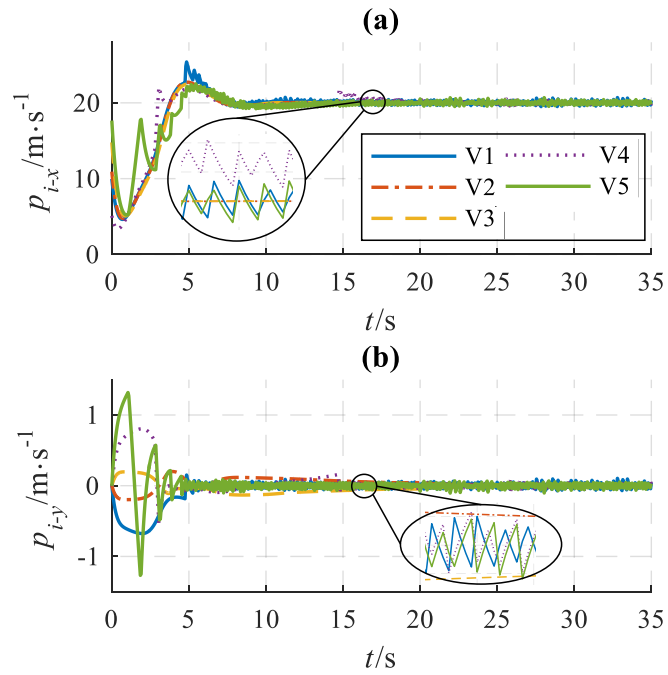
Figure 15. Longitudinal and lateral velocity trajectories of α-agents with the classic flocking control protocol.

55

of flocking rules, especially the avoidance of permanent obstacles (road boundaries), is satisfied in the strictly confined space.

When a conventional flocking algorithm without considering permanent obstacles is applied, not all of α-agents are controlled along the middle line to track the virtual γ-agent as expected, shown in Fig. 14. The vehicles, V1, V4, and V5, although are still restricted within the feasible space, move towards/against the permanent road boundaries. The geometry topology of α-agents, hence, does not achieve the desired flocking lattice. Furthermore, the oscillations around the desired speeds presented in the zoom-in circles in Fig. 15 are observed in the speed trajectories of V1, V4, and V5, which are owing to the influences of the permanent road boundaries as well. To explain the oscillations in Fig. 14 and Fig. 15, the lateral control inputs of V1, u_{1-y}, is illustrated in Fig. 16.

From the perspective of control inputs in Fig. 16, the permanent boundaries generate repulsive forces as the barriers of the α-agent V1 to avoidance obstacles. In the classic flocking control shown in Fig. 16 (a), without regulated by h_i^β, the repulsive forces from the permanent road boundaries, f_{1-y}^β, to V1 contradict to f_{1-y}^α and f_{1-y}^γ for lattice formation, collision avoidance, and virtual leader tracking. Namely, when V1 approaches to the middle line to avoid road boundaries, f_{1-y}^β decreases with the increases of f_{1-y}^α and f_{1-y}^γ. As a result, V1 moves back towards road boundaries, which increases f_{1-y}^β to push vehicles to the middle line again. Hence, the oscillations in positions and speeds occur, which is not acceptable considering the requirements of traffic safety. However, as presented in Fig. 16 (b), the augmented flocking control is able to resolve the oscillation issue with the help of h_i^β .
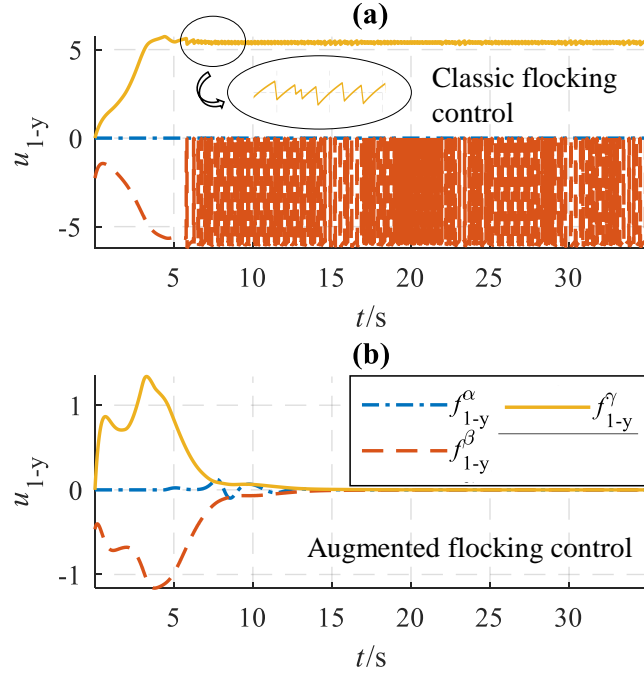
Figure 16. Lateral control inputs of V1.

Examining the responses of H and $\hat{H}$ shown in Fig. 17 (a), the five vehicles controlled by the augmented flocking control is able to asymptotically approach to a local minimum. For the classic flocking control, however, H cannot approach a local minimum because of the unexpected oscillation phenomena around the equilibrium point. In (3.39), H_β indicates the satisfaction of the obstacle zero-sum condition to avoid permanent obstacles in the strictly confined space. As shown in Fig. 17 (b), compared with the classic flocking control, the augmented flocking control successfully handles the interactions from permanent obstacles without oscillations by approaching $H_\beta = 0$. Thus, the multi-agent system with the augmented flocking control protocol is verified to achieve the set of flocking rules including permanent obstacle avoidance, as indicated in Theorem 3.3.3. On the other hand, since the obstacle zero-sum condition is not satisfied when the classic flocking control is employed, from the oscillations of

57
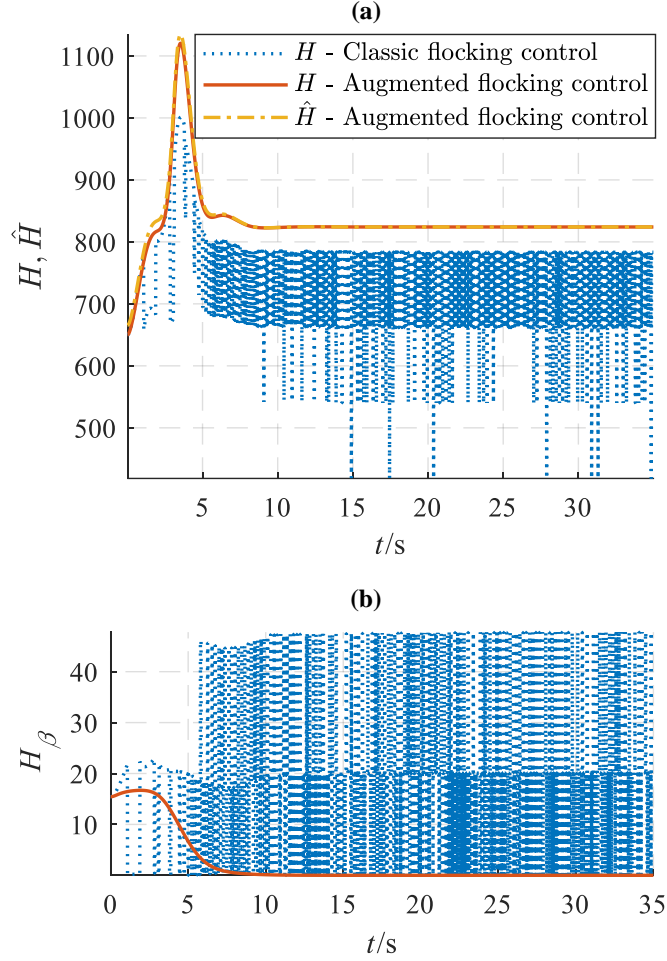
Figure 17. Hamiltonian responses of flocking controls.

H_β in Fig. 17 (b), the flocking rule of permanent obstacle avoidance is violated, as shown in Fig. 14.

3.3.5   Conclusions

This section analyzes comprehensive flocking behaviors with permanent obstacles in a strictly confined space. It is proved that the set of flocking rules including

permanent obstacle avoidance can only be achieved when the obstacle zero-sum condition is held. Moreover, a novel augmented flocking protocol is proposed to achieve flocking coordination with permanent obstacles. Implied by simulation results, the augmented flocking protocol algorithm can successfully achieve the desired flocking coordination with respect to permanent obstacles, while the existing flocking control without permanent obstacles cannot.

3.4   Energy-Efficient Flocking Control

In the nature, flocking implies certain system-level energy optimization for the migration of a group of animals. However, few literatures specifically formulate the energy efficiency performance of flocking control to investigate this important flocking feature, which is a critical concern in engineering applications. For example, UAVs and AGVs are all energy-consuming multi-agent systems for flocking control (Murray 2007). Therefore, this section is motivated to develop an energy-efficient flocking control method.

In the science of animal behavior, it is reported that geese on the border of flocks often appeared to eat more food to balance out the energy cost of grazing and vigilant behavior (Black et al. 1992). In other words, to improve the energy efficiency of the whole group, the social division with different energy-based characteristics can be observed in goose flocks with different task assignments of geese. Inspired by the foraging cooperation in goose flocks, an energy-efficient way to model the flocking phenomenon could be achieved by assigning agents with different roles corresponding to different control inputs. In the flocking theory, the control inputs of agents that perform flocking coordination are determined by the information collected from their

neighbors, obstacles, and/or leader(s). Depending on if an agent can or cannot obtain the movement information of the leader(s), a group of agents can be classified into two categories: informed and uninformed. Usually, the informed agents have larger accelerations from attraction influences of the leader(s), which force them to achieve the destination cohesion. Thus, informed agents also cost more energy than uninformed agents. In this case, the energy efficiency of cooperative control of multi-agent systems could be improved by only allocating leader's information to a small portion of agents. Namely, only a minority of agents will be selected as informed agents, and other uninformed agents just follow their nearest neighbors.

From the system-level perspective, the aforementioned idea is promising because both the communication energy and the kinetic energy will be saved, since the majority of (uninformed) agents may require less control efforts due to the lack of pertinent information from the leader(s). On the other hand, a fraction of informed agents in a group was proved to be able to lead and complete a desired coordinated motion collectively. For example, only a proportion of informed agents in a swarm was needed to guide the whole group towards a destination (Couzin et al. 2005) or velocity consensus (Su, Wang, and Lin 2009). However, with a fraction of informed agents, the fragmentation issue may emerge, as illustrated in Fig. 18. Theoretically, a flocking formation requires that the communication graph of a multi-agent system has at least one rooted spanning tree (Wang, Qin, and Yu 2014). The information absence of goals cannot guarantee that the communication topology of the multi-agent system has at least one rooted spanning tree to enable a desired flocking pattern.

To promote engineering applications of the flocking theory, energy-efficient flocking control is studied in this section based on a novel DLI method. The proposed DLI
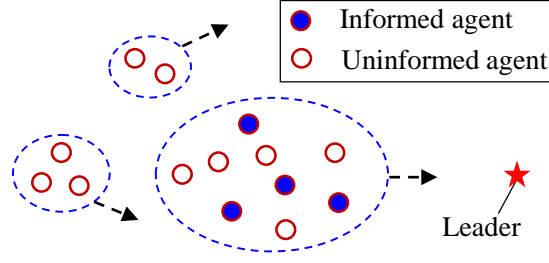
Figure 18. Fragmentation in flocking formation.

method can achieve flocking formation without fragmentation and also reduce energy consumption by seeking the least selection of informed agents.

3.4.1 Flocking Control with Selected Informed Agents for Energy Saving

In the flocking control protocol (2.5), all α-agents are informed about the states of γ-agents to avoid fragmentation. Without considering obstacle avoidance (no f_i^{β}), if a fraction of α-agents is selected to be informed, the control protocol (2.6) can be rewritten in (3.46).

$$\breve{u}_i = f_i^{\alpha} + h_i(t)f_i^{\gamma}, \tag{3.46}$$

where $h_i(t)$ is a time-varying parameter. Whenever $h_i = 1$, α-agent i is informed. Otherwise, $h_i = 0$. Since γ-agents represent the desired objectives or virtual leaders of α-agents, the positions and speeds of γ-agents can be assumed to be larger than those of α-agents for the tracking purpose. Thus, f_i^{γ} is usually nonnegative. Therefore, with the same configuration q of all nodes/agents, the relationship between the flocking control protocol (2.6) and (3.46) can be depicted by the inequality in (3.47).

$$\breve{u}_i \leq u_i. \tag{3.47}$$

The equality in (3.47) is held if and only if all α-agents are informed.

61

To evaluate the energy consumption of the group of α-agents, an energy-based index is defined as (3.48),

$$E = \int P(t)\mathrm{d}t, \tag{3.48}$$

where

$$P(t) = \sum_{i \in \mathcal{V}} \left(|u_i^{\mathrm{T}}(t)| \left| \int u_i(t) \right| \right). \tag{3.49}$$

Note that in (3.49), u_i can be replaced by $\breve{u}$. As indicated by (3.47) and (3.49), the smaller $\breve{u}$ can give less P, such that the energy consumption defined in (3.48) is reduced. In this case, the optimization of the selection of the informed α-agents is a promising way to improve the energy efficiency of the flocking control.

Remark 3.4.1. To guarantee the leader tacking performance, at least one informed α-agent should be kept, which is also the optimal number of the informed α-agents for the energy-efficient flocking control.

3.4.2   Informed Path, Cycle, and Tree

In order to prevent the fragmentation when only a fraction of informed α-agents are selected, the definitions of path, cycle, and tree in graph theory are extended to the informed path, cycle, and tree, respectively. The three new concepts are defined as follows, and also illustrated in Fig. 19.

Definition 3.4.1 (Informed path, cycle, and tree). Considering a multi-agent system as a graph G, an informed path, informed cycle, or informed tree, is defined as a (subgraph) path, cycle, or tree of G, which contains at least one informed α-agent, respectively.
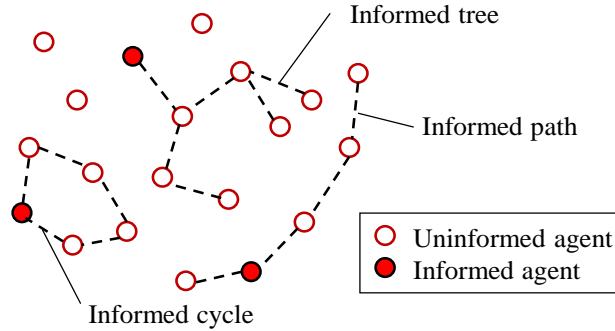
Figure 19. Illustration of informed path, cycle, and tree.

Within an informed path, cycle, or tree, every uninformed α-agent can access to at least one informed α-agent through a path based on the definition. The following lemmas provide the consensus properties of the multi-agent system controlled by the protocol (3.46), if an informed path, cycle, or tree exists.

Lemma 3.4.1 (Flocking enabled by informed path). *For a multi-agent system G with the agent dynamics shown in (2.5) and controlled by the flocking control protocol (3.46), suppose that an informed path $\mathcal{P}_{info} \subseteq G$ is a rooted spanning tree and exists for all $t \geq 0$, the flocking formation, consisting of a quasi α-lattice formation, velocity consensus, and objective tracking, is achieved without fragmentation.*

Proof. The subgraph $\mathcal{P}_{info}$ is a rooted spanning tree of G, such that $\mathcal{V}(\mathcal{P}_{info}) = \mathcal{V}(G)$. Therefore, with the first term in the flocking control protocol (3.46), the consensus of the whole group is achieved with the formation of a quasi α-lattice to avoid the fragmentation with a matched velocity, whereas all uninformed α-agents in G can access to at least one informed α-agents via a path.

For the virtual leader tracking, since $h_i = 1$ holds for all informed α-agents in (3.46), the term f_i^γ guarantees that all informed α-agents are able to track the objective. In (Su, Wang, and Lin 2009), it also claimed that an uninformed α-agent can track the

virtual leader as long as it has a path with an informed α-agent. Hence, all uninformed α-agents in G also can follow the virtual leader. $\qquad\square$

Lemma 3.4.2 (Flocking enabled by informed cycle)**.** *For a multi-agent system G with the agent dynamics shown in (2.5) and controlled by the protocol (3.46), suppose that an informed cycle $\mathcal{C}_{info} \subseteq G$ exists for all $t \geq 0$, and also spatially encloses all α-agents in the complement set $G \setminus \mathcal{C}_{info}$, the flocking formation, consisting of a quasi α-lattice formation, velocity consensus, and objective tracking, is achieved without fragmentation.*

Proof. The class of α-agents spatially enclosed by $\mathcal{C}_{info}$ is denoted by $\mathcal{B}$, such that $\mathcal{V}(G) = \mathcal{B} \cup \mathcal{C}_{info}$. If $\mathcal{B} = \varnothing$, a rooted spanning tree of G in the form of an informed path is contained in $\mathcal{C}_{info}$ whenever any edge of $\mathcal{C}_{info}$ is removed to break the cycle. Thus, using Lemma 3.4.1, all α-agents in G achieve the flocking without the fragmentation.

If $\mathcal{B} \neq \varnothing$, $\mathcal{C}_{info}$ is a subgraph of G, such that $\mathcal{V}(\mathcal{C}_{info}) \subset \mathcal{V}(G)$. When $\mathcal{C}_{info}$ intends to achieve flocking, the space enclosed by $\mathcal{C}_{info}$ is contracted. In this regard, given the finite interaction range d_r, the shrunk spatial space makes any enclosed α-agent in $\mathcal{B}$ is asymptotically connected to α-agents in $\mathcal{C}_{info}$. Namely, G contains a bipartite graph $G_{bi} = \mathcal{E}_{bi}, \mathcal{V}(\mathcal{B}), \mathcal{V}(\mathcal{C}_{info})$ as $t \to \infty$, whose partition has the mapping relationship from $\mathcal{V}(\mathcal{B})$ to $\mathcal{V}(\mathcal{C}_{info})$ via the edge set $\mathcal{E}_{bi}$. Therefore, the union $G_{bi} \cup \mathcal{C}_{info}$ contains a rooted spanning tree, and all uninformed α-agents can access to at least one informed α-agents through a path. $\qquad\square$

Lemma 3.4.3 (Flocking enabled by informed tree)**.** *For a multi-agent system G with the agent dynamics shown in (2.5) and controlled by the protocol (3.46), suppose that an informed tree $\mathcal{T}_{info} \subseteq G$ is a rooted spanning tree, and exists for all $t \geq 0$, the*

flocking formation, consisting of a quasi α-lattice formation, velocity consensus, and objective tracking, is achieved without fragmentation.

Proof. Since a tree can be broken down into multiple paths (Godsil and Royle 2013), an informed tree $\mathcal{T}_{info}$ can also be broken down into several informed paths, namely $\mathcal{T}_{info} = \bigcup_{i \in I} \mathcal{P}^i_{info}$, where $I = 1, 2, \ldots$. Using Lemma 3.4.1, each partition $\mathcal{P}^i_{info}$ is able to achieve the flocking without the fragmentation. Hence, $\mathcal{T}_{info}$ can also achieve the flocking without the fragmentation. $\qquad\qquad\square$

Collecting Lemma 3.4.1, 3.4.2, and 3.4.3, the following theorem of the fragmentation prevention is developed to avoid the fragmentation with a portion of informed α-agents.

Theorem 3.4.1 (Fragmentation prevention)**.** *For a multi-agent system G with the agent dynamics shown in (2.5) and controlled by the protocol (3.46), suppose that only a fraction of α-agents is informed, the fragmentation is prevented if every uninformed α-agent satisfies at least one of the following conditions for all $t \geq 0$:*

(i) Belongs to an informed path, cycle, or tree;

(ii) Spatially enclosed by an informed cycle.

Proof. If the set of spatial neighbors of an α-agent is not empty, the α-agent must belong to a path, cycle, or tree, which connects the α-agent to any of its neighbors. Thus, the connected α-agents in the graph G can be represented by a group of paths, which can composite the cycle or tree further, if possible. Based on Lemma 3.4.1, 3.4.2, and 3.4.3, the uninformed α-agents have to belong to an informed path, cycle, or tree to avoid the fragmentation to guarantee the formation of the rooted spanning tree.

If the set of spatial neighbors of an α-agent is empty, the α-agent is called individual α-agent, which cannot access any information from other α-agents. Using Lemma 3.4.2,

the uninformed individual α-agent still can be a part of desired flocking formation if it is spatially bounded by an informed cycle. Otherwise, the individual α-agent has to be informed to prevent the fragmentation. $\qquad\qquad\qquad\qquad\qquad\qquad\qquad$ □

Essentially, two conditions in Theorem 3.4.1 guarantee that every α-agent is either informed or uninformed that accesses at least one informed α-agent through a path, although the multi-agent system does not have a root spanning tree yet.

3.4.3 Distributed Least-Informed Method

To reduce the energy cost of the flocking control of multi-agent systems, one possible method is to only select a fraction of informed α-agents. In this section, the DLI method is developed to seek the least required informed α-agents for energy efficiency improvement. To avoid the fragmentation issue, the DLI method should satisfy Theorem 3.4.1 strictly.

Based on Remark 3.4.1, the least one informed α-agent is anticipated to achieve the most energy-efficient flocking without fragmentation. However, this unique informed α-agent cannot be determined until a rooted spanning tree appears. Therefore, the DLI method works in an iterative fashion to monotonically decrease the number of informed α-agents and simultaneously satisfy the conditions in Theorem 3.4.1. Given initial positions of all α-agents, the initial informed α-agents is determined through the following (3.50).

An α-agent i is initially selected to be informed if the inequality in (3.50) is satisfied.

$$\left(q_i - q_j \right)^{\mathrm{T}} \cdot \left(q_i - q_i^c \right) \geq 0, \forall j \in N_i^{\alpha}, \qquad\qquad (3.50)$$

66
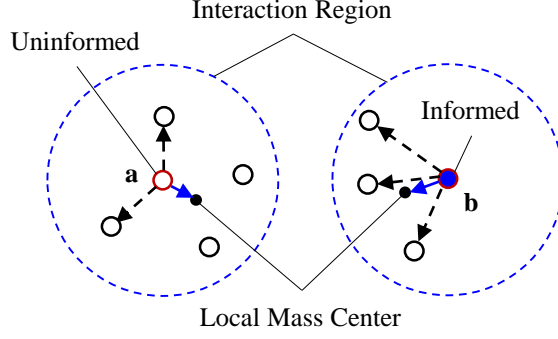
Figure 20. Initial selection of the informed and uninformed α-agents.

where q_i^c is a local mass center defined as

$$q_i^c = \text{Ave}(N_i^\alpha) = \frac{q_i + \displaystyle\sum_{j \in N_i^\alpha} q_j}{|N_i^\alpha| + 1},$$ (3.51)

in which $|N_i^\alpha|$ denotes the quantity of N_i^α.

The DLI method is created in a distributed manner. Therefore, each α-agent can be determined as informed or uninformed based on the information only gathered from its neighbors set N_i^α. The inequality in (3.50) also works for $N_i^\alpha = \varnothing$, which gives $q_i^c = q_i$ and thus makes the left-hand side of the inequality zero. Hence, α-agents with $N_i^\alpha = \varnothing$ should be initialized as informed ones. For clarification, Fig. 20 illustrates the initial selection of the informed and unformed α-agents of a network using (3.50). The α-agent "a" in Fig. 20 is initialized as an uninformed agent since there are two agents within the neighbor set do not satisfy the inequality in (3.50). However, all α-agents in the neighbor set of the α-agent "b" hold the inequality in (3.50), so that the α-agent "b" is initialized as an informed agent.

After initialization, an updating policy is needed to change the informed α-agents to uninformed and vice versa during the flocking formation. In the updating process, on one hand, an uninformed α-agent has to be changed to be informed to avoid

fragmentation if it does not satisfy the conditions in Theorem 1 anymore. Since all uninformed α-agents are enclosed by the informed cycles after the initialization based on (3.50), using Lemma 3.4.2, the uninformed α-agents can always access at least one informed α-agent through a path. Hence, none of the uninformed α-agents need to change status after the initialization, which guarantees that the number of informed α-agents is monotonically decreased during the formation of flocking.

On the other hand, some informed α-agents need to be updated to become uninformed to save energy. To achieve this update without fragmentation (satisfy the conditions in Theorem 3.4.1), an informed α-agent is updated to be uninformed if and only if it connects to another informed α-agent via a path. In other words, the loss of the information privilege should not influence any other uninformed α-agents to satisfy the conditions in Theorem 3.4.1. Since the undirected communication topology is utilized, an arbitral agreement is necessary to determine the sequence of the loss of the information privilege of two or more connected informed α-agents. The arbitral index is defined in (3.52).

$$\Omega_i = \|q_i - q_r\| + \|p_i - p_r\| , i \in \mathcal{V}. \tag{3.52}$$

The informed α-agent is changed to be uninformed whenever it has the largest Ω_i, compared with any other connected and informed α-agents. Due to the distributed configuration, all involved informed α-agents can be updated simultaneously in every time interval.

3.4.4   Simulation Results and Discussions

In this section, simulation results are displayed to verify the energy-efficient flocking control, enabled by the proposed DLI method. In the simulation, 10 α-agents

are commanded to move in free 2-dimensional space without obstacles. The finite interaction range d_r is 4.5 m, the lattice scale d is 3 m, and the edge-length uncertainty ϵ is 0.1 m. Moreover, the simulated agents are initialized with random positions in the box area $[0, 30] \times [0, 30]$ m^2 with zero velocities. The virtual unique leader, γ-agent, of the group of α-agents is set to move along a straight line with the constant velocity vector $[1.5, 0]^{\mathrm{T}}$ m/s, which starts from the initial position $(15, 15)$. Thus, 10 α-agents are expected to achieve a quasi α-lattice and move collectively around the γ-agent. Moreover, the average speeds of the group of α-agents, $\bar{q}_x$ and $\bar{q}_y$, is used to indicate the velocity consensus.

Three different cases are investigated in this section for comparisons with the same initial condition and flocking control setups. In the first case, all the α-agents are assumed to be informed and controlled by the classic protocol without h_i. In the second case, the group of α-agents is controlled by the protocol (3.46), and three α-agents in the group are randomly selected to be informed initially without updates. Finally, the DLI method is demonstrated in the third case to generate informed α-agents. Simulation results are presented in Fig. 21, 22, 23, 24, 25.

The movement of the group of α-agents for three cases is shown in Fig. 21, 22, 23, where the red circles represent the uninformed α-agents and the red circles with blue stars represents the informed α-agents. In Fig. 21, the flocking without the fragmentation is achieved when all α-agents are informed, which shows the similar results given in (Olfati-Saber 2006) and (Su, Wang, and Lin 2009). In Fig. 22, the fragmentation happens and only a small portion of uninformed α-agents connected to the three informed α-agents is formatted in the desired flocking pattern. The result of
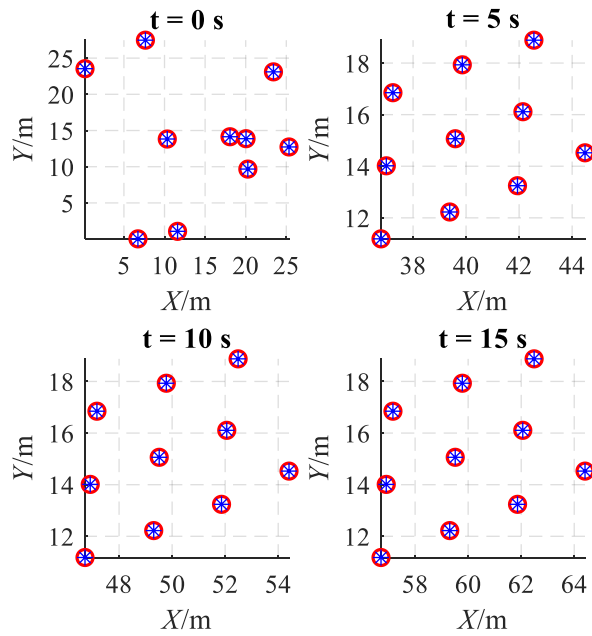
Figure 21. Flocking formation of α-agents for Case 1.
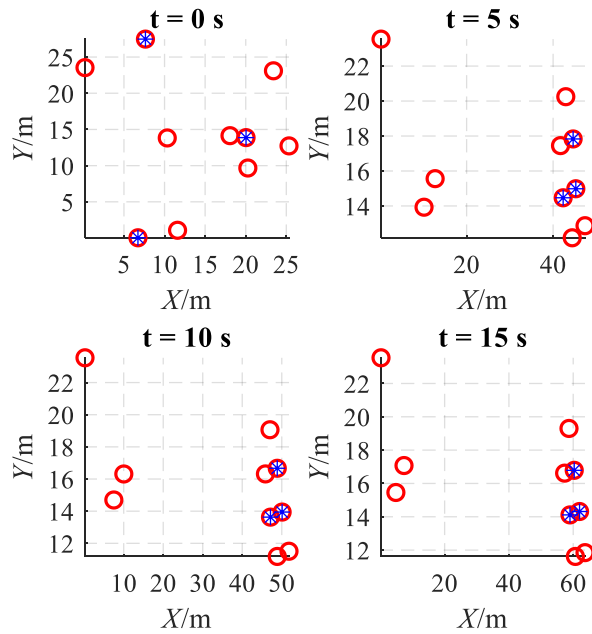
Figure 22. Flocking formation of α-agents for Case 2.
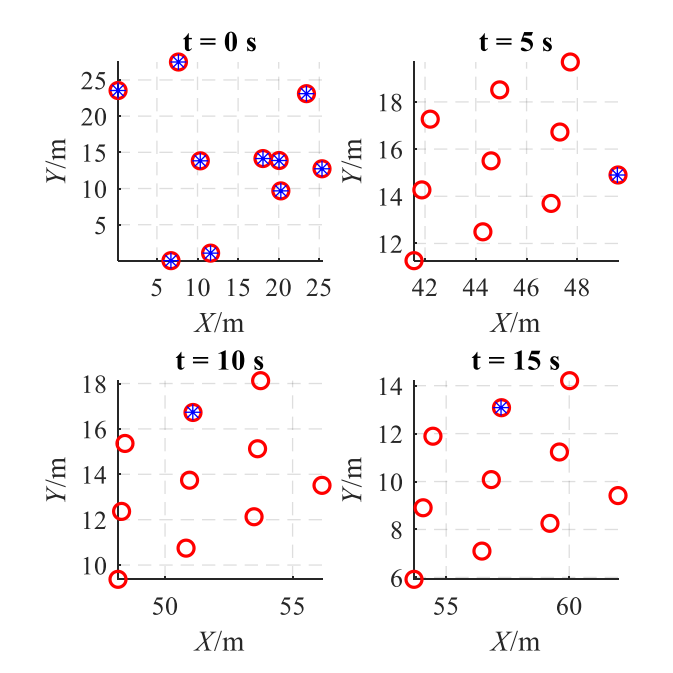
Figure 23. Flocking formation of α-agents for Case 3.

Case 3 in Fig. 23 shows that a desired flocking without fragmentation is achieved, and the number of informed α-agents is decreased. Therefore, the informed α-agents generated by the DLI method are able to satisfy the conditions in Theorem 3.4.1 and finally lead the desired flocking configuration. Moreover, in Fig. 23, the final number of informed α-agents is only one, which is the least number of required informed α-agents for tracking the leader. Although the steady flocking configurations of Case 1 and Case 3 are different (see $t = 15$ s in Fig. 21 and Fig. 23), both of them are the desired flocking formations as well as satisfy the flocking rules.

Fig. 24 shows the velocity consensus performance of the flocks. The group of α-agents controlled by the protocol (3.46) in Case 1 can successfully track the desired velocity vector of the given γ-agent. Compared with the failure of velocity consensus in Case 2, the flocks in Case 3 can track the desired velocity. Since the quantity of
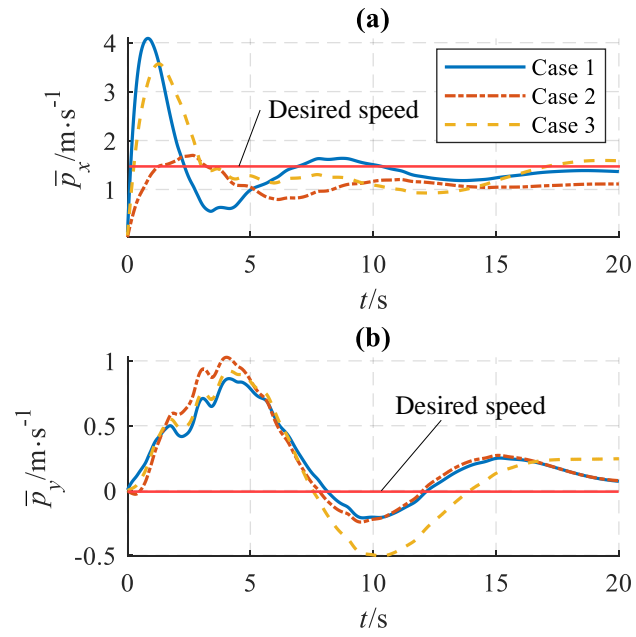
Figure 24. Velocity consensus of the flocks.
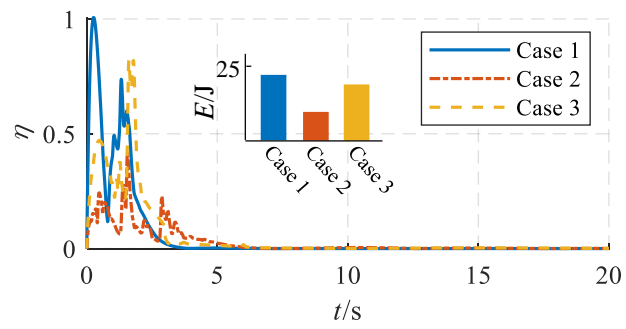
Figure 25. Energy consumption of the flocks.

informed α-agents is decreased in the process of flocking, the velocity tracking errors are slowly decreased over a relatively long time. This is because the impact of the virtual leader, γ-agent, is reduced by less informed α-agents. The fast convergence of the flocking control is an interesting topic and will be addressed in the future.

The energy efficiency performance of the DLI method is demonstrated in Fig. 25, in which η denotes the normalization of P. As shown in the bar chart of Fig. 25, the integrals of P, namely E, of Case 1, Case 2, and Case 3 are 23.9 J, 11.2 J, and 20.1 J, respectively. Compared with Case 1, the energy consumption for Case 3, when the DLI method is applied, is reduced by 15.9% via appropriately selecting less informed α-agents. Note that it is meaningless to have the least energy in Case 2, since the randomly selected informed α-agents cannot avoid the fragmentation. While employing the DLI method may increase the onboard computational energy cost, the energy savings on the kinetic energy consumption is typically much more than the computational energy cost for practical multi-agent systems, such as UAVs and AGVs.

3.4.5   Conclusions

This section proposes the DLI method to generate the least required informed α-agents to improve the energy efficiency of the flocking control and simultaneously avoid the fragmentation. Demonstrated by three simulation examples for a multi-agent system with 10 α-agents, the simulation results show that the group of α-agents controlled by the protocol with the DLI method can successfully achieve the desired flocking configuration with less energy consumption.

Chapter 4

HIERARCHICAL FLOCKING FRAMEWORK FOR CAV SYSTEMS

4.1   Overview

The existing fundamental benchmark of flocking control of multi-agent systems can be summarized as follows: a group of agents is controlled by flocking protocols to achieve desired flocking rules based on double-integrator models and the NID transformation. This fundamental benchmark may work for some multi-agent systems, such as mobile robots and unmanned aerial vehicles (UAVs), but not for CAV systems, of which the nonlinear vehicle dynamics and tire forces cannot be handled by double-integrator models and the NID transformation.

In this chapter, two main issues in the application of flocking theory in the cooperative control of CAV systems are resolved. First, nonlinear vehicle dynamics are fully considered in the flocking control of CAV systems. Second, the vehicle yaw/orientation dynamics are well addressed without the NID transformation. The detailed contributions of this chapter are summarized as follows [3].

1. A novel hierarchical flocking control framework for CAV systems is proposed, which can handle complex nonlinear vehicle dynamics without using the NID transformation. Within the novel framework, mission planning, path planning, speed profile generation, and local vehicle dynamics control are synthesized together. Moreover, different vehicle sizes can be considered in the modified

_____
[3]The main content of this chapter is based on the author's works in (Wang and Chen 2018a) and (Wang and Chen 2020a).

flocking control design. Note that the proposed framework can be applied to other artificial multi-agent systems as well, such as UAVs, autonomous underwater vehicles, and mobile robots.

2. The agent/vehicle dynamics sectionalization is provided. Benefited from the proposed framework, different models of agent/vehicle dynamics are applied in different layers. Hence, the practical nonlinear vehicle dynamics are separated from the high-level flocking controller, which is authentically utilized in the low-level trajectory tracking control.

3. The predictive orientation guidance of CAV systems is produced. Given global path trajectory references and speed profiles, a sequence of the ideal heading angles is predicted based on the assumption of zero sideslip angle of vehicles, which is continuously described by an optimal fitting curve. Thus, the orientation reference is defined by taking the first-time derivative of the optimal fitting curve.

4. Together with nonlinear vehicle dynamics, path planning, speed trajectory, and orientation guidance are tracked through both feedforward and feedback controllers. In the low-level controller design, this chapter exploits an analytical single-point preview (ASPP) driver model as the feedforward control. Furthermore, a nonlinear Lyapunov controller with control allocation is employed as the feedback control to fully take the merits of the over-actuated vehicles.

5. An integrated simulation example of the flocking control of CAV systems on the multi-lane traffic environment is demonstrated with nonlinear vehicle dynamics, an obstacle, and multiple distinctive destinations.

4.2 Stability Issue of the NID Transformation

The NID transformation that cannot be applied in the flocking control of CAV systems is discussed in this section. In the flocking algorithm depicted in (2.6), only translation motions of α-agents modeled are controlled. However, the orientations of agents are not considered. Thus, when any flocking control law is applied to CAV systems, an under-actuated control problem emerges since vehicle yaw dynamics also need to be controlled. In this regard, the NID transformation method was proposed to tackle the under-actuated control mathematically (Olfati-Saber 2002).

In the NID transformation, the dynamics of a kinematic $SE(2)$ vehicle (introduced in (4.7)) is augmented with λ dynamics governed by (4.1).

$$\dot{\lambda} = -c_\lambda \left(\lambda - \epsilon \right), \tag{4.1}$$

where $0 < \epsilon < \lambda(0) < 1$, and $0 < c_\lambda$. The augmented agent dynamics is shown in (4.2).

$$
\begin{cases}
\dot{q}_i = R_{\lambda_i} v + \dot{\lambda} R_{\lambda_i} \mathrm{e}_1 \\[4pt]
\dot{p}_i = R_{\lambda_i} \tau_i + R_{\lambda_i} \hat{r}_i(\lambda, \dot{\lambda}) v + \dot{\lambda} R_{\lambda_i} \left[\hat{r}_i(\lambda, \dot{\lambda}) - c_\lambda \mathrm{I} \right] \mathrm{e}_1 \\[4pt]
\dot{R}_{\lambda_i} = R_{\lambda_i} \hat{r}_i(\lambda, \dot{\lambda}) \\[4pt]
\dot{v}_i = \tau_i
\end{cases}
, \tag{4.2}
$$

where $R_{\lambda_i} = [R_i \mathrm{e}_1, \lambda R_i \mathrm{e}_2]$, $\mathrm{e}_2 = [0,1]^{\mathrm{T}}$, and $\hat{r}_i(\lambda, \dot{\lambda})$ is defined in (4.3).

$$
\hat{r}_i(\lambda, \dot{\lambda}) =
\begin{bmatrix}
0 & -\lambda_i \\[6pt]
\dfrac{r_i}{\lambda} & \dfrac{\dot{\lambda}}{\lambda}
\end{bmatrix}.
\tag{4.3}
$$

For the second equation in (4.2), the control input τ_i is obtained by directly applying u_i to the double-integrator dynamics, as shown in (4.4).

$$\tau_i = R_{\lambda_i}^{-1} u_i - \hat{r}_i(\lambda, \dot{\lambda}) v_i - \dot{\lambda} \left[\hat{r}_i(\lambda, \dot{\lambda}) - c_\lambda \mathrm{I} \right] \mathrm{e}_1. \tag{4.4}$$

76

Hence, the second factor of τ_i, denoted by τ_i', for vehicle yaw dynamics control is obtained in (4.5).

$$\dot{r}_i = \tau_i' = -\frac{V_i}{\lambda}r_i + \frac{R_{2i}^{\mathrm{T}}}{\lambda}u_i, \qquad (4.5)$$

where R_{2i} is the second column of R_i. The explicit solution of (4.5) is solved as (4.6).

$$r_i(t) = r_{0i}e^{-\frac{V_i}{\lambda}t} + \int_0^t e^{-\frac{V_i}{\lambda}(t-s)}\frac{R_{2i}^{\mathrm{T}}}{\lambda}u_i\mathrm{d}s, \qquad (4.6)$$

From (4.6), vehicle yaw rate $r_i(t)$ is exponential stable without flocking control ($u_i = 0$). The first issue in (4.6) is that the yaw dynamics is dominated by λ dynamics with small λ values ($\lambda < 1$) and not controllable, which may not be desired for yaw rate tracking control purposes. Second, the control inputs determined in (4.4) is not designed for yaw rate stabilization or tracking. In fact, to achieve flock coordination and obstacle avoidance, the flocking control law may influence the transit performance of exponential stability of $r_i(t)$. As also suggested in (Olfati-Saber 2002), vehicle yaw dynamics could be locally controlled to track the desired yaw rate, which could be independent to the NID transformation. Last but not the least, the NID method may be only applicable for SE(2) vehicles. This transformation cannot be employed to practical nonlinear vehicle dynamics or other autonomous systems that have specific yaw motion control requirements. Note that the translation motion of CAV systems is not discussed here, which is controlled by flocking algorithms directly to guarantee flocking coordination and stability.
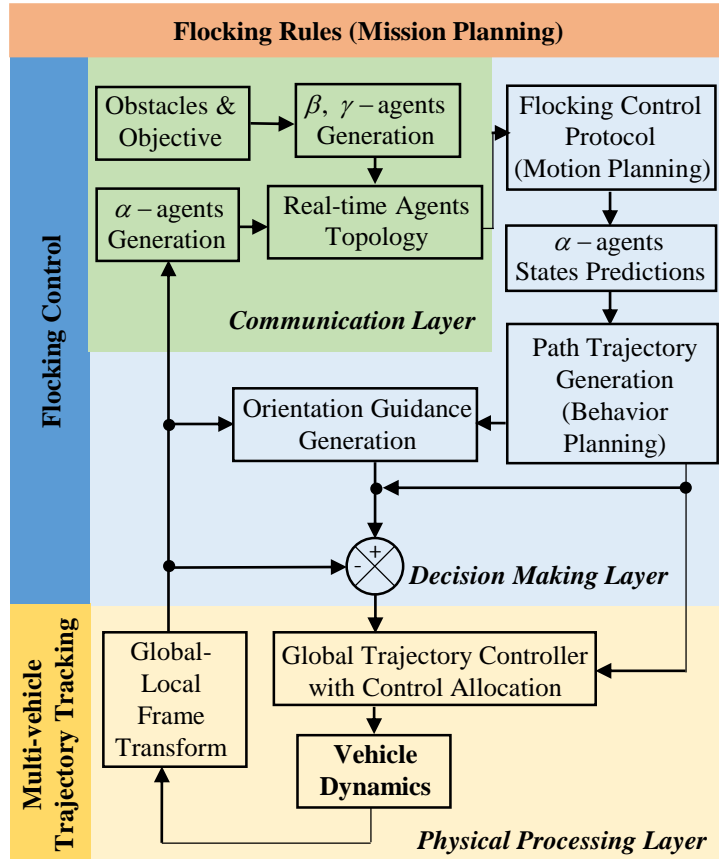
Figure 26. Novel hierarchical framework for the flocking control.

4.3 Hierarchical Framework for Flocking Control

4.3.1 Framework Configuration

To tackle the issues resulted from vehicle dynamics and orientation control, a novel hierarchical framework for the flocking control of CAVs is proposed in Fig. 26, which represents a typical vehicular CPS. From Fig. 26, the proposed framework contains two main components, the high-level flocking control and the low-level trajectory tracking control of CAV systems.

The high-level flocking control consists of information sharing and decision making in the network. Given the flocking rules, flocking theory is utilized to generate the trajectory references of the path and speed profile of a group of agents in the high-level layer, which includes mission planning, motion planning, and behavior planning. Namely, based on the shared global state-feedback of α-agents, updated obstacle detection, and objective setup, the geometric topology of multi-agent systems is generated in the communication layer of the vehicular CPS. The states of vehicles are predicted by applying the flocking control protocol in the high-level layer. Here, the flocking rules serve as the mission planning of CAV systems, and the flocking control protocol provides the motion planning of each vehicle. Moreover, the predicted states of vehicles are utilized to generate the desired references of trajectories and orientations, which is considered as the behavior planning of each vehicle.

In the low-level physical layer, the flocking control is realized through a class of global trajectory tracking control problems solved by the local vehicle dynamics controllers with the control allocation. The advantages of the proposed flocking control framework are stated as follows.

First, the proposed framework does not require dynamics transformation, such as the NID method. Hence, there is no stability issue introduced by the NID transformation (see section 4.2) when the flocking protocol is applied to control nonlinear vehicle dynamics, which make the proposed framework applicable to many other autonomous multi-agent systems, such as unmanned aerial vehicles, autonomous underwater vehicles, and mobile robots.

Second, the hierarchical configuration clearly separates the high-level flocking control design and the low-level control design for physical processing systems. From Fig. 26, a successful system synthesis depends on accurate predictions of vehicle states.

However, the simple agent dynamics are hard to fully and accurately predict the real vehicle states due to high nonlinearities. Benefited from the proposed hierarchical framework, the employment of simplified agent models in the high-level layer does not influence the prediction errors, if vehicles can fully track the references, including the path trajectories and orientations, generated by the flocking algorithm. Thus, in addition to achieving the high-level references, additional control requirements and more practical and complex system dynamics can be added and satisfied in the low-level control design.

Third, the proposed flocking control framework enables over-actuated vehicle control with prediction features. The independent low-level vehicle control can be formulated as an over-actuated control problem, which has more control degrees of freedom and feasibility to realize better control performance. In addition, given the state feedback of agents, the trajectories and orientations of agents are generated by the flocking algorithm with prediction features, which also benefit predictive control performance for the flock coordination to avoid collisions.

Fourth, the proposed hierarchical framework can handle the obstacle avoidance in the real world. Even though it is challenging for vehicles to acquire sufficient information of obstacles on the road in practice, the obstacle avoidance in the flocking control does not require full knowledge of all obstacles as long as the obstacles can be detected before vehicles approach them. Namely, in the proposed hierarchical framework, vehicles only need to avoid the obstacles that appear within finite detection ranges of vehicles. The detection ranges depend on the capability of the onboard sensors. Therefore, the proposed framework is suitable for obstacle avoidance in real-world situations.

Remark 4.3.1. Although some existing studies reported separating the high-level planning and the low-level trajectory tracking, those research works were mainly about a single vehicle, which cannot be extended for CAV systems in a straightforward way (Lim et al. 2018). On the one hand, the practical nonlinear vehicle dynamics and tire model are enclosed in the proposed framework. Hence, the road condition is considered. On the other hand, the complete framework for CAV systems not only has the high-level planning module and the low-level tracking control but also involves the communication layer, which can be recognized as a vehicular CPS and does not exist for a single-vehicle.

4.3.2 Traffic Rules in Flocking Control

To represent traffic rules for the application of the high-level flocking control, two typical traffic scenarios are mainly identified in this dissertation, namely lane-keeping and lane-changing driving maneuvers. When the flocking control protocol is applied to transportation systems, the corresponding definitions of β-agents and γ-agents are proposed to accommodate the lane-keeping and lane-changing behaviors.

The definitions of β-agents and γ-agents representing basic vehicle behaviors in traffic are shown in Fig. 27. For the lane-keeping scenario in Fig. 27 (a), β-agents are defined as two boundary lines of the lane, which serve as the permanent spatiotemporal constraints to achieve the lane-keeping control. At the same time, α-agents also receive the information from the navigational (virtual) γ-agent that moves along with the middle line of the lane. When the lane is blocked by an obstacle, the lane-changing behavior is expected to avoid the collision.
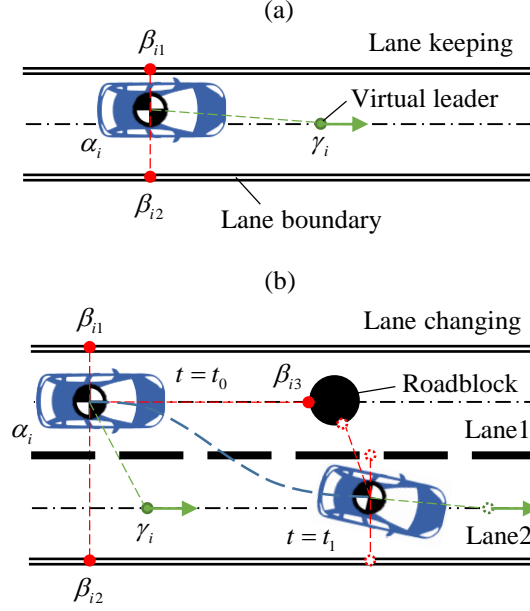
Figure 27. Definitions of β-agents and γ-agents for lane-keeping and lane-changing.

For the lane-changing scenario in Fig. 27 (b), before the vehicle enters the targeted lane, the boundary between two lanes is not described as β-agents anymore, while the outer boundaries of two lanes and the roadblock still perform as the constraints to generate β-agents. After the vehicle entering the targeted lane, the lane-keeping control is resumed. To lead the lane-changing maneuver, the γ-agent is also switched to move along with the middle line of the targeted lane.

Remark 4.3.2. Obstacles, namely β-agents can be either continuous or discrete, which depends on the obstacle properties. For example, the road boundary lines in Fig. 27 can generate continuous β-agents since they are permanent constraints of vehicles. However, the roadblock in a lane may provide a discrete β-agent since it only temporally appears in the detection range of vehicles. The virtual leaders γ-agents are continuous because α-agents should always receive the virtual leader information during the flocking process.

4.4 Vehicle Dynamics Sectionalization

Benefited by the proposed flocking coordination framework, the high-level flocking control of multi-agent systems and the low-level control of physical systems are able to adopt different dynamic models of the same agents to balance computation efficiency and control performance. Thus, for CAV systems, in addition to the aforementioned double-integrator dynamics in (2.5), $SE(2)$ vehicle dynamics and nonlinear single-track vehicle dynamics are introduced in this section.

4.4.1 Global $SE(2)$ vehicle dynamics

The global $SE(2)$ vehicle dynamics integrates vehicle global coordinates and orientations, which is depicted in (4.7).

$$
\begin{cases}
\dot{x} = \begin{bmatrix} \dot{X} & \dot{Y} \end{bmatrix}^{\mathrm{T}} = (R\mathbf{e}_1)V \\[2mm]
\dot{R} = R\hat{r} \\[2mm]
\dot{v} = \tau
\end{cases}
, \tag{4.7}
$$

where x is vehicle global position with two coordinates X and Y, $\mathbf{e}_1 = \begin{bmatrix} 1 & 0 \end{bmatrix}^{\mathrm{T}}$, $\hat{r} = \mathrm{diag}(r, -r)$. In addition, $v = \begin{bmatrix} V & r \end{bmatrix}^{\mathrm{T}}$, τ is control input, and R is the rotation matrix associated with vehicle heading angle ψ that is defined in (4.8).

$$
R = \begin{bmatrix} \cos\psi & -\sin\psi \\ \sin\psi & \cos\psi \end{bmatrix}. \tag{4.8}
$$
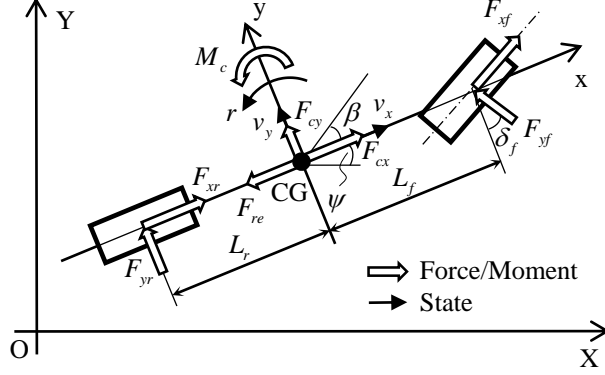
Figure 28. Single-track vehicle model diagram.

4.4.2 Nonlinear Single-Track Vehicle Dynamics

A nonlinear single-track vehicle dynamics model is adopted to describe the planar motion of vehicles, which is illustrated in Fig. 28.

Within Fig. 28, x-y is a local coordination frame of the vehicle. The governing equations of the vehicle dynamics with respect to the local frame are formulated in (4.9).

$$
\begin{cases}
M(\dot{v}_x - rv_y) = \underbrace{-F_{yf}\sin\delta + F_{xf}\cos\delta_f + F_{xr} - F_{re}}_{f_x} + F_{cx} \\
M(\dot{v}_y + rv_x) = \underbrace{F_{yf}\cos\delta_f + F_{xf}\sin\delta_f + F_{yr}}_{f_y} + F_{cy} \\
I_z\dot{r} = \underbrace{F_{yf}L_f\cos\delta_f - F_{yr}L_r + F_{xf}L_f\sin\delta_f}_{f_m} + M_c
\end{cases}
, \qquad (4.9)
$$

where f_x, f_y, and f_m are the external resultant longitudinal force, lateral force, and yaw moment from tires and air, respectively.

To determine tire forces in (4.9), the Dugoff's tire model is applied, which is featured by the simple formulation but able to describe the nonlinearities and coupling effects of tire longitudinal and lateral forces (Ding and Taheri 2010).

4.4.3 Model Sectionalization and Transformation

In the proposed flocking control framework, different control algorithms in different modules take the merits of different vehicle dynamics models to balance computational efficiency and control performance. Table 1 lists the sectionalization assignment of dynamic models.

Table 1. Dynamics model sectionalization assignment

Module	Dynamics Model
Flocking control	Double-integrator dynamics
Orientation guidance	$SE(2)$ vehicle dynamics
Global trajectory controller	Nonlinear vehicle dynamics

In the flocking theory, the double-integrator dynamics of agents (2.5) are applied. In the orientation guidance module, the full global planar motion of agents should be considered, which includes both translation and rotation of agents. Thus, the global $SE(2)$ vehicle dynamics (4.7) are adopted to generate orientation guidance. In the global trajectory controller with the control allocation, the single-track vehicle dynamics (4.9) have to be employed for considering practical vehicle performances and tire forces.

Remark 4.4.1. In the low-level control allocation, the load transfer among four tires is also considered, which is not explicitly shown in (4.9).

When the measured states of multiple vehicles are input to the information layer and the high-level control layer of the vehicular CPS, the following transformation
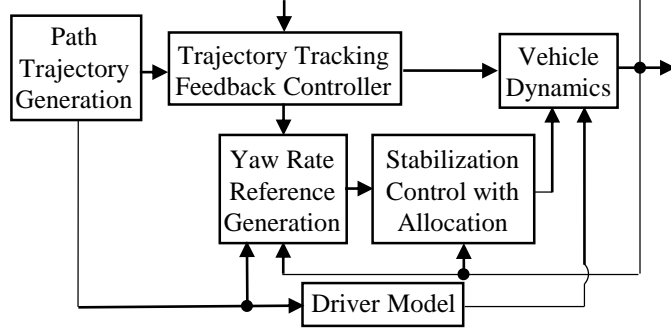
Figure 29. Trajectory tracking control configuration.

from the local frame to the global frame via (4.10) should be applied.

$$
\begin{bmatrix} v_x \\ v_y \end{bmatrix} = \begin{bmatrix} \cos{(\psi + \beta)} & \sin{(\psi + \beta)} \\ -\sin{(\psi + \beta)} & \cos{(\psi + \beta)} \end{bmatrix} \begin{bmatrix} \dot{X} \\ \dot{Y} \end{bmatrix} \tag{4.10}
$$

4.5   Controller Design

In this chapter, the high-level flocking control employs the conventional flocking control protocol, and the size of vehicles is considered. Besides, the low-level trajectory tracking control configuration is presented in Fig. 29. To fully track the states of α-agents, both global position and speed errors need to be mitigated. For the global positions tracking, a novel driver model, ASPP, is proposed to give the feedforward control to minimize both longitudinal and lateral position tacking errors, which considers the real-time flocking control requirements and the sensitivity of lateral tire forces. Furthermore, a nonlinear feedback Lyapunov controller with control allocation is designed for the global speeds tracking and the yaw motion stabilization.
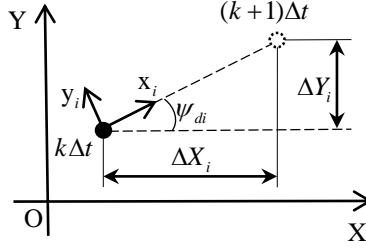
Figure 30. Definition of an ideal heading angle for an agent.

4.5.1 High-Level Flocking Control

The high-level flocking control protocol is implied in (3.23). To accommodate the dimensions of vehicles, the modified desired lattice scale is defined as $d' = d + d_L$, in which d_L is larger than the largest dimension of CAVs. Hence, the parameter d in the flocking protocol (3.23) is replaced by d'.

4.5.2 Predictive Orientation Guidance for CAV systems

The path references of CAV systems are directed from the positions of α-agents in flocking theory. However, as shown in (2.5), α-agents are typically modeled as a group of mass points without considering their orientations or yaw dynamics, while the yaw dynamics control is essential for vehicle driving. In this section, a predictive orientation planner is proposed to produce the yaw rate references for multi-vehicle systems. To maintain vehicle stability, zero sideslip angle is usually anticipated, which requires the vehicle lateral speed to be controlled around zero. Namely, it is ideal for α-agents to head towards their reference positions at the next time interval, which can be predicted through the flocking theory.

To track zero sideslip angle references of vehicles, Fig. 30 gives the definition of an ideal heading angle of α-agent i. In Fig. 30, Δt is the sampling interval and k is a positive integer, and ΔX_i and ΔY_i are longitudinal and lateral distances between the current position of α-agent i at $k\Delta t$ and the next position reference at $(k+1)\Delta t$, respectively. From Fig. 30, the ideal heading angle ψ_{di} at $k\Delta t$ is defined in (4.11).

$$\psi_{di}(k\Delta t) = \arctan\left(\frac{\Delta Y_i}{\Delta X_i}\right) = \arctan\left(\frac{\dot{Y}_i(k\Delta t)}{\dot{X}_i(k\Delta t)}\right). \tag{4.11}$$

Given a n-step time horizon starting from $(k\Delta t)$, the states $\dot{Y}_i$ and $\dot{X}_i$ of α-agent i only at $(k\Delta t)$ are from the real-time feedback, and the states from $(k+1)\Delta t$ to $(k+n-1)\Delta t$ are predicted by the flocking algorithm. Thus, in addition to $\psi_{di}(k\Delta t)$, the other $n-1(n>1)$ predicted values of the ideal heading angles can also be determined using the same method as shown in (4.11), which are denoted by $\psi_{di}((k+1)\Delta t)$, $\ldots$, $\psi_{di}((k+n-1)\Delta t)$. Then, an optimal fitting curve function $f_i(t)$ is obtained to continuously describe the ideal heading angle sequence, which is a polynomial function as depicted in (4.12).

$$\psi_{di} = f_i(t) = \sum_{j=0}^{n-1} a_j t^j, \tag{4.12}$$

where a_j is the polynomial coefficient. Taking the first time derivative of $f_i(t)$, the slope value of the fitting curve at the first time point $k\Delta t$, denoted by $r_{di}(k\Delta t)$, is adopted as the yaw rate control reference, and it is updated iteratively along with the shifted time horizon, as shown in Fig. 31. Within Fig. 31, ψ_i denotes a measurement of the current heading angle, and $\tilde{\psi}_{di}$ denotes the predicted heading angle.

In sum, based on the requirement of zero sideslip angles, the ideal heading angles and yaw rates of CAV systems are produced through current states of agents, path predictions via flocking protocols, and optimal curve fitting. Therefore, the yaw rate
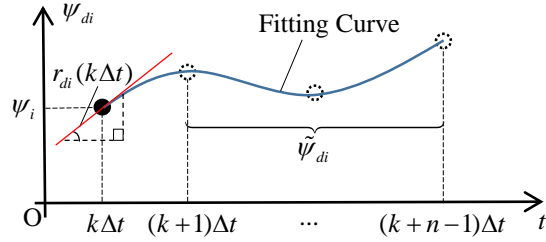
Figure 31. Determination of the predictive yaw rate reference.
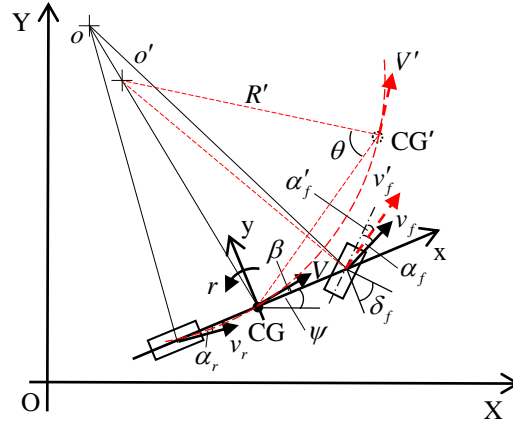
Figure 32. Schematic geometry of vehicle path tracking.

references are consistent with vehicle path trajectory tracking and yaw dynamics stabilization.

4.5.3 Analytical Single-Point Preview Driver Model

A novel ASPP driver model is proposed in this section to perform as a feedforward control for path tracking. The schematic geometry of vehicle path tracking is presented in Fig. 32. Within Fig. 32, o is the current vehicle steering center. Besides, the superscript $(\cdot)'$ denotes the control targets of vehicle states, and R' is the steering radius with respect to o'.

Given the corresponding coordinates of CG and CG', namely (X, Y) and (X_d, Y_d), respectively, the vehicle steering center should move from o to o' to make the vehicle drive along an ideal circular curve connecting CG and CG', which is the red dash curve in Fig. 32. As a result, a new front slip angle α'_f is required. The output of the ASPP driver model is the desired feedforward steering angle δ', which is depicted in (4.13).

$$\delta' = \beta + \frac{L_f r}{v_x} - \alpha'_f. \tag{4.13}$$

From the geometry relationship and desired driving path shown in Fig. 32, the desired front tire sideslip angle is determined in (4.14).

$$\alpha'_f = \arctan\left(\frac{R' + \sin\beta + L_f}{R' \cos\beta}\right), \tag{4.14}$$

in which

$$R' = \frac{\sqrt{(X_d - X)^2 + (Y_d - Y)^2}}{2\cos\theta}, \tag{4.15}$$

where

$$\theta = \frac{\pi}{2} + \beta - \arctan\left(\frac{Y_d - Y}{X_d - X}\right) + \psi. \tag{4.16}$$

From (4.15) and (4.16), the tracking errors of both longitudinal and lateral path trajectories are considered. Thus, the ASPP driver model is able to be applied to the flocking control of CAV systems.

4.5.4 Nonlinear Laypunov Controller Design with Control Allocation

Assume that the corrective control in (4.9) are achieved through the common active front steering (AFS) control and the direct yaw moment control (DYC). Thus, besides the feedforward control δ', three feedback control efforts are designed as the virtual control inputs, F_{cx}, F_{cy}, and M_c, which can be realized by the AFS and DYC.

Based on (4.9), the control law given by the following proposition can track the vehicle speeds trajectory and the yaw rate reference.

Proposition 4.5.1. *The virtual feedback control input $\tilde{u} = \begin{bmatrix} F_{cx} & F_{cy} & M_c \end{bmatrix}^T$ in (4.17) makes the tracking errors of driving speeds and yaw rates asymptotically stable.*

$$\tilde{u} = \bar{\mathbf{M}} \left(\dot{\chi}_d + \chi_d - \chi + \begin{bmatrix} -rv_y & rv_x & 0 \end{bmatrix}^T \right) - \mathbf{f}, \tag{4.17}$$

where $\bar{\mathbf{M}} = diag(M, M, I_z)$, $\chi = \begin{bmatrix} v_x & v_y & r \end{bmatrix}^T$ is vehicle states, $\chi_d = \begin{bmatrix} v_{xd} & v_{yd} & r_d \end{bmatrix}^T$ is vehicle reference, and $\mathbf{f} = \begin{bmatrix} f_x & f_y & f_m \end{bmatrix}^T$. A rotation matrix is adopted to transform vehicle coordinates between the local and global frames, as indicated in (4.10).

Proof. Given the reference vector χ_d, the tracking error vector is defined as

$$\mathbf{e} = \begin{bmatrix} e_1 & e_2 & e_3 \end{bmatrix}^T = \chi - \chi_d. \tag{4.18}$$

Defining a Lyapunov function in (4.19), we have the derivative of $\dot{V}$ in (4.20).

$$V = \frac{1}{2} \mathbf{e}^T \mathbf{e}. \tag{4.19}$$

$$\dot{V} = \sum_{j=1}^{3} \dot{e}_j e_j. \tag{4.20}$$

From (4.20), the condition,

$$\dot{e}_j = -e_j, j = 1, 2, 3, \tag{4.21}$$

makes $\dot{V}$ negative definite, namely

$$\dot{V} = -\sum_{j=1}^{3} \dot{e}_j^2 < 0. \tag{4.22}$$

Substituting (4.9) and (4.18) into (4.21), we have

$$\begin{cases} \dot{v}_x = rv_y + \dfrac{f_x + F_{cx}}{M} = \dot{v}_{xd} + v_{xd} - v_x \\ \dot{v}_y = -rv_x + \dfrac{f_y + F_{cy}}{M} = \dot{v}_{yd} + v_{yd} - v_y \\ \dot{r} = \dfrac{f_m + M_c}{I_z} = \dot{r}_d + r_d - r \end{cases} . \tag{4.23}$$

91

Therefore, the feedback control law in (4.17) are obtained by solving (4.23). $\qquad\square$

To incorporate all the vehicle control systems together, the relationship between the achievable values of $\tilde{u}$ from the control allocation, $\tilde{u}'$, and the real control vector U are developed as

$$
\tilde{u}' = \begin{bmatrix} F'_{cx} \\ F'_{cy} \\ M'_c \end{bmatrix} = SU, \tag{4.24}
$$

where

$$
S = \begin{bmatrix} 0 & 1 & 1 & 1 & 1 \\ C_f & 0 & 0 & 0 & 0 \\ L_f C_f & l_s/2 & -l_s/2 & l_s/2 & -l_s/2 \end{bmatrix}, \tag{4.25}
$$

and $U = \begin{bmatrix} \Delta\delta_f & F_{cx}^{fl} & F_{cx}^{fr} & F_{cx}^{rl} & F_{cx}^{rr} \end{bmatrix}^{\mathrm{T}}$, in which $\Delta\delta_f$ is the corrective front steering angle, and F_{cx}^{fl}, F_{cx}^{fr}, F_{cx}^{rl}, and F_{cx}^{rr} are four corrective longitudinal tire forces. The quadratic control allocation problem is formulated in (4.26).

$$
\begin{aligned}
\min_{U} \quad & J = (\tilde{u}' - \tilde{u})^{\mathrm{T}} W_1 (\tilde{u}' - \tilde{u}) + U^{\mathrm{T}} W_2 U \\
\text{s.t.} \quad & U \in U_b
\end{aligned}, \tag{4.26}
$$

where J is the cost function, W_1 and W_2 are the weighting matrix, and U_b is the feasible region of U. In (4.26), the cost function J contains the actuator penalty and the error generated by the control allocation algorithm. Hence, the real feedback control effort is

$$
U = \arg\min_{U \in U_b} J(t, \tilde{u}, U). \tag{4.27}
$$
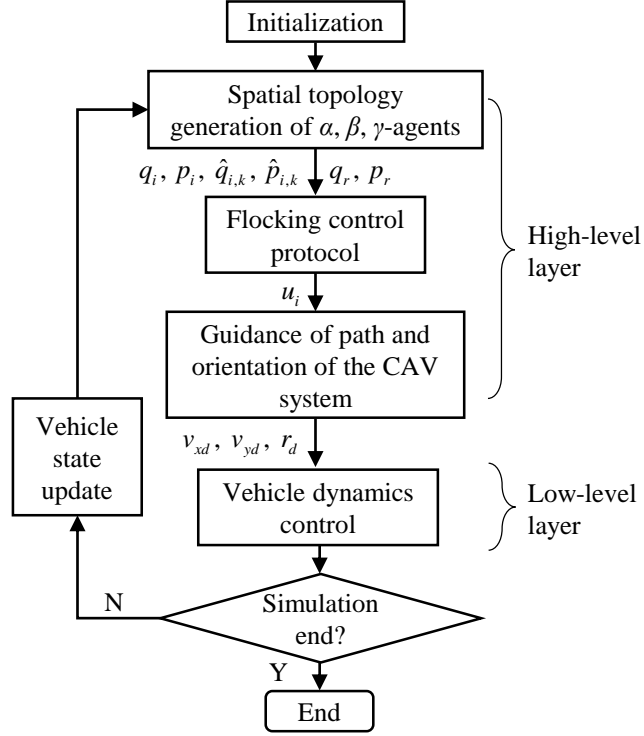
Figure 33. Flowchart of the simulation configuration.

4.6 Simulation Results and Discussions

Simulations are conducted in MATLAB/Simulink® to verify the novel flocking control framework with trajectory tracking for CAV systems. The flowchart of the simulation configuration is shown in Fig. 33.

The parameters of vehicles and flocking control are listed in Table 2. Considering the real sizes of the CAVs, the width (wheel track) is 1.65 m, and the length (wheelbase) is 3.05 m, so that L is 3.05 m.

The simulated scenario is a one-way three-lane straight highway with an obstacle on the middle line of "Lane 2", as shown in Fig. 34. The two outer lane boundaries

Table 2. Parameter values of simulated vehicles and flocking control

Symbol	Parameter values
M	1,650 kg
I_z	3,234 kg · m^2
C_x	80,000
C_y	45 kN · rad^{-1}
L_f	1.4 m
L_r	1.65 m
d_r	48 m
d	40 m
$c_{1,2}^{\alpha}$	1
$c_{1,2}^{\beta}$	1.2
$c_{1,2}^{\gamma}$	1
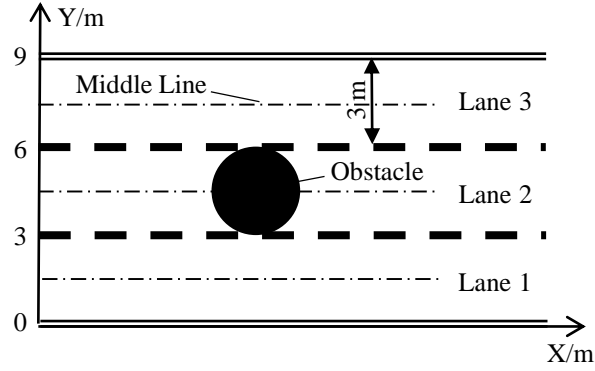
Figure 34. A one-way three-lane highway with an obstacle.

are indicated as double lines at $Y = 0$ m and $Y = 9$ m, and the obstacle, as one β-agent, is always served as the spatial constraint. The obstacle has a round shape with a radius at 1.5 m, which can totally block "Lane 2". To avoid the obstacle, the lane-changing maneuvers of vehicles are expected.

Four different cases are investigated in the simulation. In the first case, five indistinctive vehicles, V1-V5, are controlled to achieve the flocking coordination on the middle line of "Lane 2" at $Y = 4.5$ m, and the obstacle locates at $X = 50$ m. In addition, vehicles (α-agents) are controlled to follow γ-agents with a constant desired

speed at 20 m/s on the highway, where the tire-road friction coefficient in the Dugoff's tire model is set as 0.85. Initial yaw rates and sideslip angles are all zeros. The vehicle initial positions are randomly selected in the area of $(X_0, Y_0) \in [0, 40\text{m}] \times [0, 9\text{m}]$, and the non-zero initial longitudinal speeds are selected in the set $V_{x0} \in (0, 20\text{m/s})$. Compared with the first case, the second case only changes the obstacle location, which is moved to $X = 420$ m to examine the influence of the obstacle on a different stage of the flocking coordination. The third case is the most complicated one. Instead of a unique middle line tracking, vehicles are assigned to achieve flocking on two different middle lines of "Lane 1" and "Lane 2" where $Y = 1.5$ m and $Y = 4.5$ m, for the obstacle at $X = 320$ m. Finally, the fourth case is an unstable case without obstacles by using the existing fundamental benchmark. Namely, the proposed hierarchical flocking control framework is not employed. In the fourth case, the double-integrator agent dynamics is used, and the NID transformation as shown in section 4.2 is also used for vehicle yaw dynamics control without considering nonlinear vehicle dynamics. Other setups in the fourth case are the same as what are used in the first case. The simulation results of these cases are presented in Fig. 35.

As illustrated in Fig. 35, all simulated CAVs start from different random initial positions without overlaps. In Fig. 35 (a) for the first case, the obstacle appears during the coordinating process of the quasi α-lattice, or the flocking. The plot indicates that five vehicles are able to avoid the suddenly emerged roadblock, which can be detected in real-time through the advanced onboard perception and sensing systems, such as lidar, camera, and radar. Bypassing the roadblock, the flocking is then gradually realized as shown in the enlarged circle. The constant distances among vehicles are remained for improving traffic capacity. In the second case, the flocking is achieved first, as presented in Fig. 35 (b). After that, while moving with the desired flocking
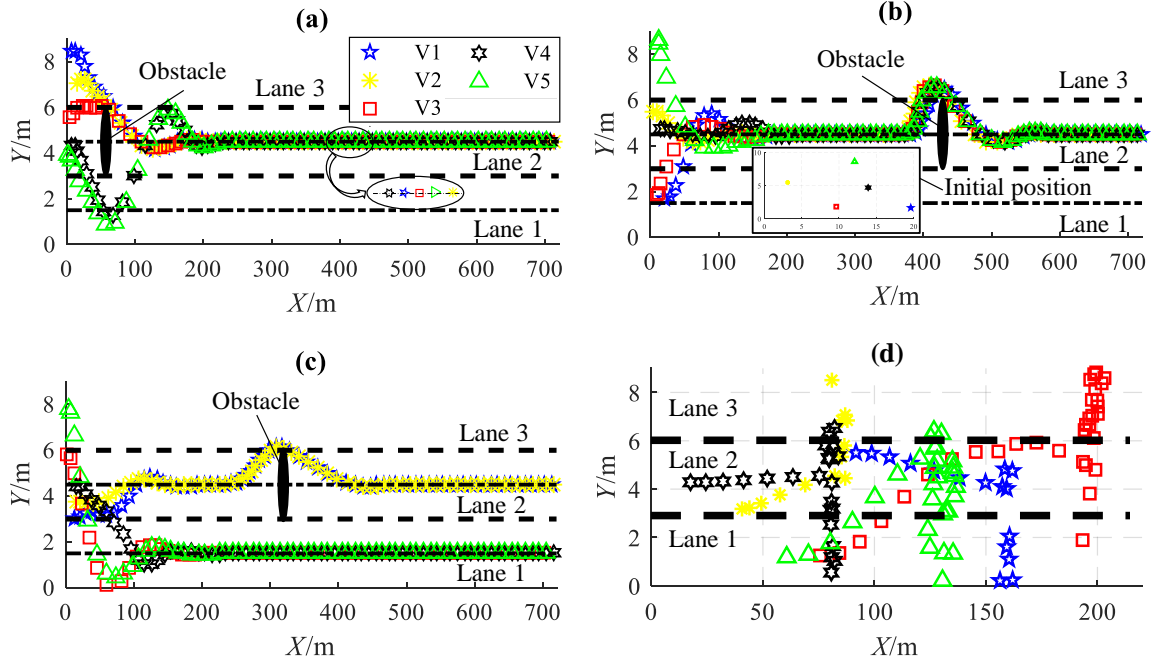
Figure 35. Path trajectories of five simulated vehicles in four different cases.

coordination, the CAV systems can still avoid the obstacle in a collective manner. In the third case, shown in Fig. 35 (c), led by two different assigned objectives (γ-agents), two groups of flocks are controlled on the middle lines of "Lane 1" and "Lane 2", respectively. Therefore, the CAV systems with flocking control can robustly achieve the flocking coordination to track multiple objectives and avoid collisions in a 2D traffic environment. Moreover, once the flocking is reached, all connected vehicles within the flocking behave in a collective fashion.

The flocking path trajectories of the fourth case are presented in Fig. 35 (d). The unstable vehicle control performance is observed, which is consistent with the analyses in section 4.2. Therefore, compared with the proposed flocking control framework, the existing flocking algorithm by using the NID and simplified double-integrator dynamics cannot handle nonlinear vehicle dynamics and orientation control. Thus, flocking behaviors cannot be successfully achieved.
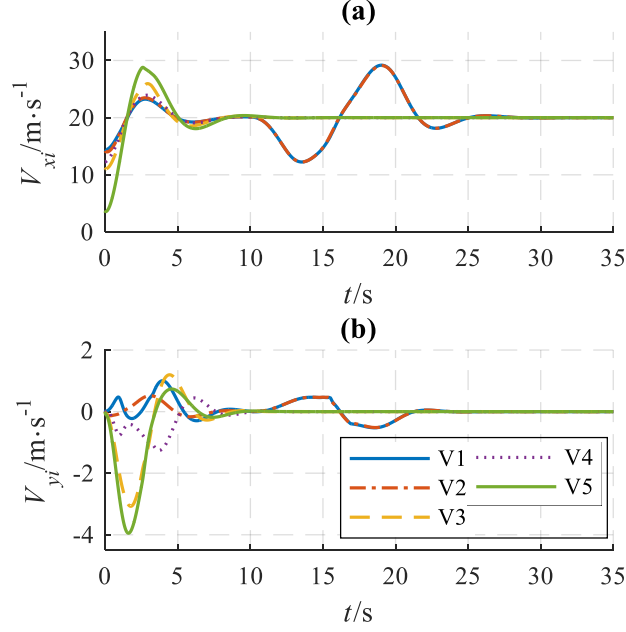
Figure 36. Global speeds of vehicles in the third case.

Furthermore, in Fig. 35, the steady-state of the flocking coordination is similar to the vehicle platooning. That is because the road boundary serves as the permanent spatial constraint during the lane-keeping scenario, which is always symmetric to the trajectory of γ-agent. In this regard, vehicle platooning can be recognized as one of the special cases of vehicle flocking coordination.

In detail, Fig. 36, 37, 38, 39, and 40 present the vehicle states, tracking errors, and control inputs in the third case as a paradigm. The corresponding global speeds responses of vehicles are shown in Fig. 36. It can be seen that all simulated vehicles can track the desired speeds, which is defined as 20 m/s for V_{xi} and 0 m/s for V_{yi}. Thus, velocity alignment in the flock is successfully performed. From Fig. 37, the vehicle yaw and lateral stability of vehicles are maintained through the orientation guidance and control.

97
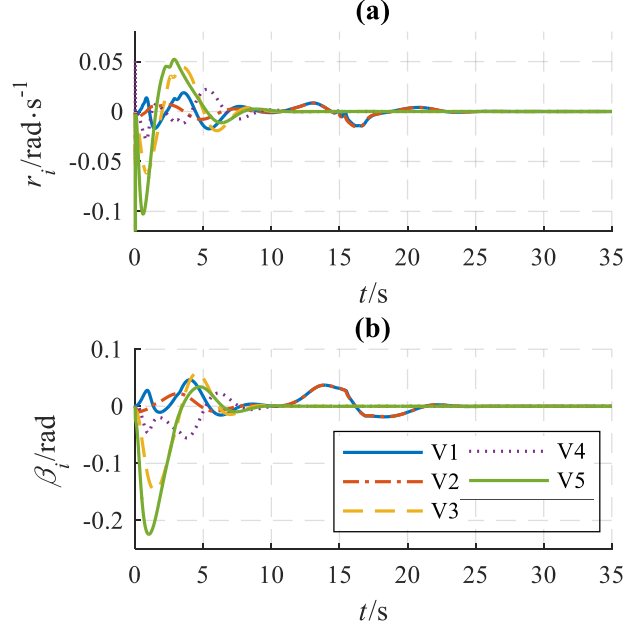
Figure 37. Yaw rates and sideslip angles of vehicles in the third case.

The reference tracking performances are presented in Fig. 38. Considering the nonlinear vehicle dynamics based on the novel framework, tracking errors of global path trajectories and vehicle local states are suppressed by the driver model and the nonlinear Lyapunov controller. In addition, owing to the small tracking errors illustrated in Fig. 38, the prediction errors resulted from the simple agent dynamics model are compensated, which is also one of the advantages of the proposed framework. Therefore, the hierarchical control framework with model sectionalization involving the nonlinear vehicle dynamics guarantees the stabilization performance of trajectories tracking of the global positions and orientations with small tracking errors.

In the high-level control layer, the flocking control law gives control efforts, as presented in Fig. 39, which indicate that both global longitudinal and lateral acceleration commands are stable to achieve the path trajectories in Fig. 35 (c). After the control
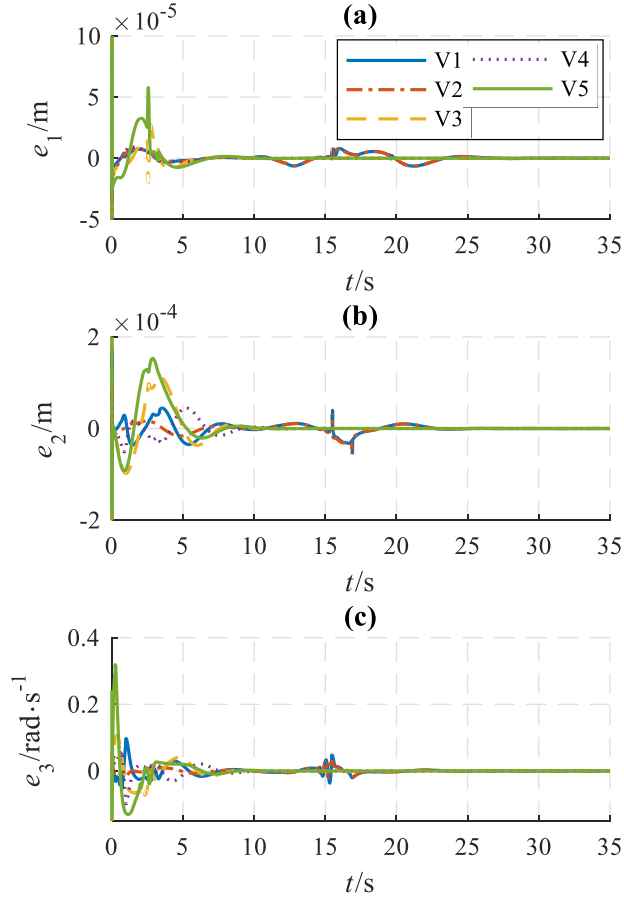
Figure 38. Tracking errors of vehicles in the third case.

allocation, the feedback control efforts are reasonably commanded, as indicated in Fig. 40.

Using the proposed hierarchical flocking coordination framework, the high-level layer only provides the real-time global path planning, and the detailed local orientation reference and trajectory tracking control inputs are generated and achieved by the low-level control of realistic nonlinear vehicle dynamics. Compared with vehicle platooning control, the CAV system with the flocking control interacts in a 2D protocol, even with multiple different cohesion destinations.
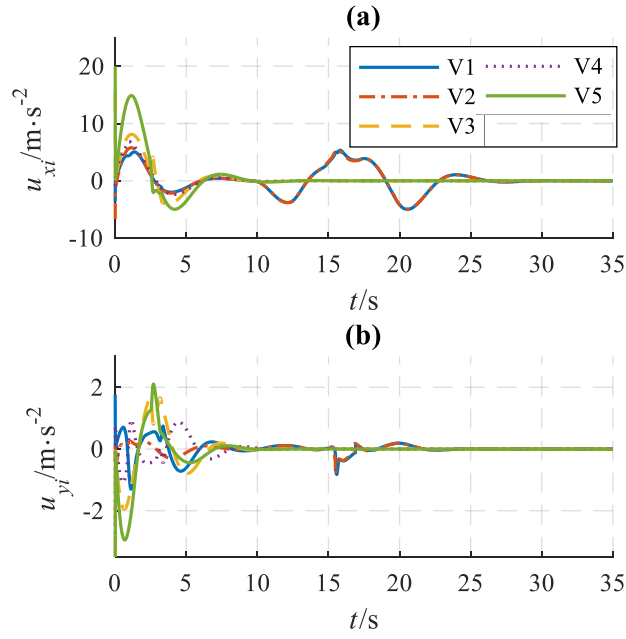
Figure 39. Virtual control inputs of α-agents in the third case.
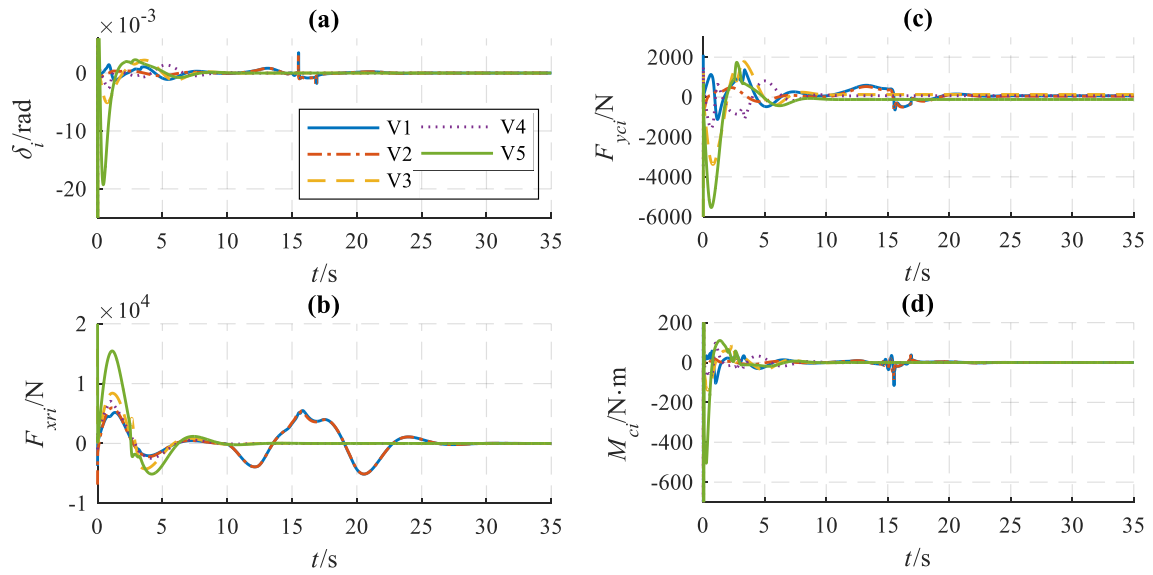
Figure 40. Real control inputs of vehicles in the third case.

All the obtained simulation results assume that the vehicles are identical. Because vehicles with various parameters are more practical in a real transportation system, heterogeneous vehicles with different sizes, dynamics, and/or constraints should be considered. In fact, the proposed framework may still work even if the high-level homogeneous agent dynamics is applied to the low-level heterogeneous vehicle dynamics. For instance, vehicles with larger sizes and masses usually have larger powers for prolusion and control. Therefore, a group of vehicles with heterogeneous dynamics could still overcome the prediction errors resulted from the homogeneous agent dynamics if the control capabilities are enough to achieve small tracking errors.

The general heterogeneous dynamics problem is still challenging for the flocking theory and cooperative control of vehicles, which will be an interesting future work to extend the proposed framework.

4.7   Conclusions

This chapter introduces a novel hierarchical flocking coordination framework to extend the application of the flocking theory for the cooperative control of multi-CAVs. Without relying on the NID transformation, the proposed hierarchical framework gives the global path trajectory in the high-level control layer and considers the nonlinear vehicle dynamics in the low level, which achieves the orientation and trajectory tracking control locally. Demonstrated by different cases in the one-way three-lane highway simulation, the proposed flocking coordination framework can successfully achieve velocity alignment, orientation control, collision avoidance between CAVs and obstacle, and multiple destinations cohesion with small tracking errors.

Chapter 5

EXPERIMENTAL VALIDATION OF FLOCKING CONTROL

The experimental validation of flocking control is necessary to prove the feasibility of flocking applications in transportation systems. Therefore, to conduct vehicular flocking experiments, a prototype of CAV research platform is introduced in this chapter, which includes three CAVs, as shown in Fig. 41. In particular, each CAV includes a drive-by-wire chassis and an onboard control system with wireless communication. Furthermore, three experimental cases are investigated in this chapter to demonstrate the proposed hierarchical flocking framework for CAV systems.

Figure 41. The scaled vehicle platform prototype.
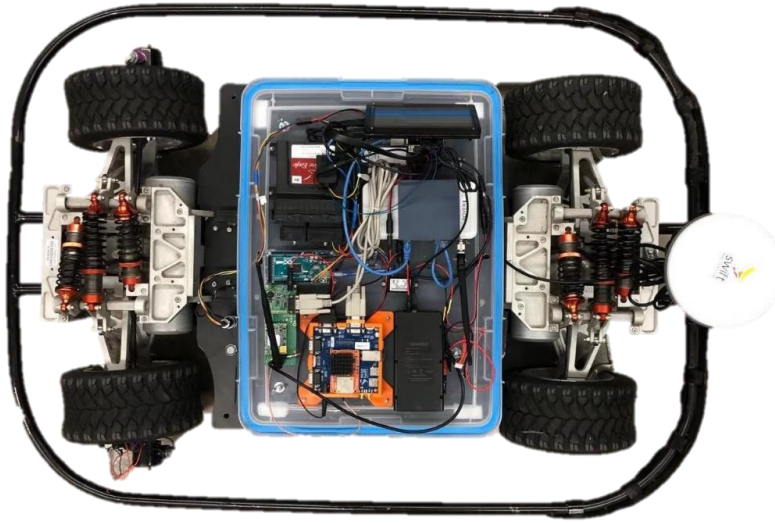
Figure 42. Mechanical configuration of scaled vehicle platform prototype.

5.1   Scaled Vehicle Platform Prototype Development

5.1.1   Vehicle Chassis

The configuration of the chassis design of each scaled CAV is presented in Fig. 42. The chassis is purely driven by electricity with four independent motors. Additionally, the chassis also has two steering motors to provide four-wheel steering capability. In particular, the chassis can be controlled through drive-by-wire technologies by using CAN bus protocols. Some vehicle parameters of the developed scaled CAV are listed in Table 3.

Table 3. Parameter values of a scaled CAV

Category	Values
Size (length × width × height)	1030 mm × 632 mm × 265 mm
Weight	sprung mass: 50 kg; unsprung mass: 8 kg
Maximum payload	20 kg
Maximum acceleration	$9 \text{ m} \cdot \text{s}^{-2}$ with zero payload
Maximum speed	53 mph
Battery capacity	30,000 mAh
Peak power	3 kW

5.1.2   Vehicle Power and Control System

The configuration of the CAV power and control system is shown in Fig. 43. The power supply of the scaled CAV is a package of the 12V, 30,000 mAh LiFePO4 battery equipped with a battery management system (BMS). The actuators of the scaled CAV include four driven motors and two servo steering motors. All on-board devices (e.g. GNSS, Raspberry Pi) and sensors are powered by an additional 12V DC onboard battery.

For control purposes, as shown in Fig. 43, the scaled CAV uses a Raspberry Pi 3 Model B+ as an onboard computer to share, transform, and record data. The low-level vehicle dynamics control unit employs New Eagle Raptor BCM 48, which receives vehicle states and sends CAN control commands to the chassis. The vehicle inertial states are measured by an inertial measurement unit (IMU), and the vehicle global positions and heading angles are obtained through a real-time kinematic GNSS system, which can provide the scaled CAV centimeter-level positioning. To connected three CAVs together and monitor vehicle statuses, a set of V2V and V2I networks are created for information sharing. In detail, the V2V network is developed based on the

UDP/IP protocol, and the V2I network is a WiFi-based network to start/stop the automatic control of scaled CAVs and retrieve data.

5.1.3 Vehicular Onboard Software System

The configuration of the vehicle onboard software system is presented in Fig. 44. In the onboard computer (Raspberry Pi 3 B+), a set of Python scripts is programmed to configure system setups, enable data transmission, transformation, and recording, and generate high-level flocking control inputs. The information going through V2X communication, including V2V and V2I communication, is also transmitted via the onboard computer. To accommodate the I2C bus using by IMU, an Arduino board with C scripts is adopted for data acquisition. Furthermore, for the low-level control of actuators, the rapid prototype development method is used to produce control algorithms by MATLAB/Simulink®.

5.2 Experiment Setups

The experiments are conducted in open flat ground, in which the antenna position of the GNSS base station is the origin of the global coordinate, and the directions of east and north are assigned as X and Y directions of the global coordinate, respectively.

To verify the proposed hierarchical flocking control framework for CAV systems, three cases are investigated in this chapter. The first case is free flocking without any influences from obstacles. In the first case, three CAVs (α-agents) are required to track a unique virtual leader (γ-agent). The second case is constrained flocking. In
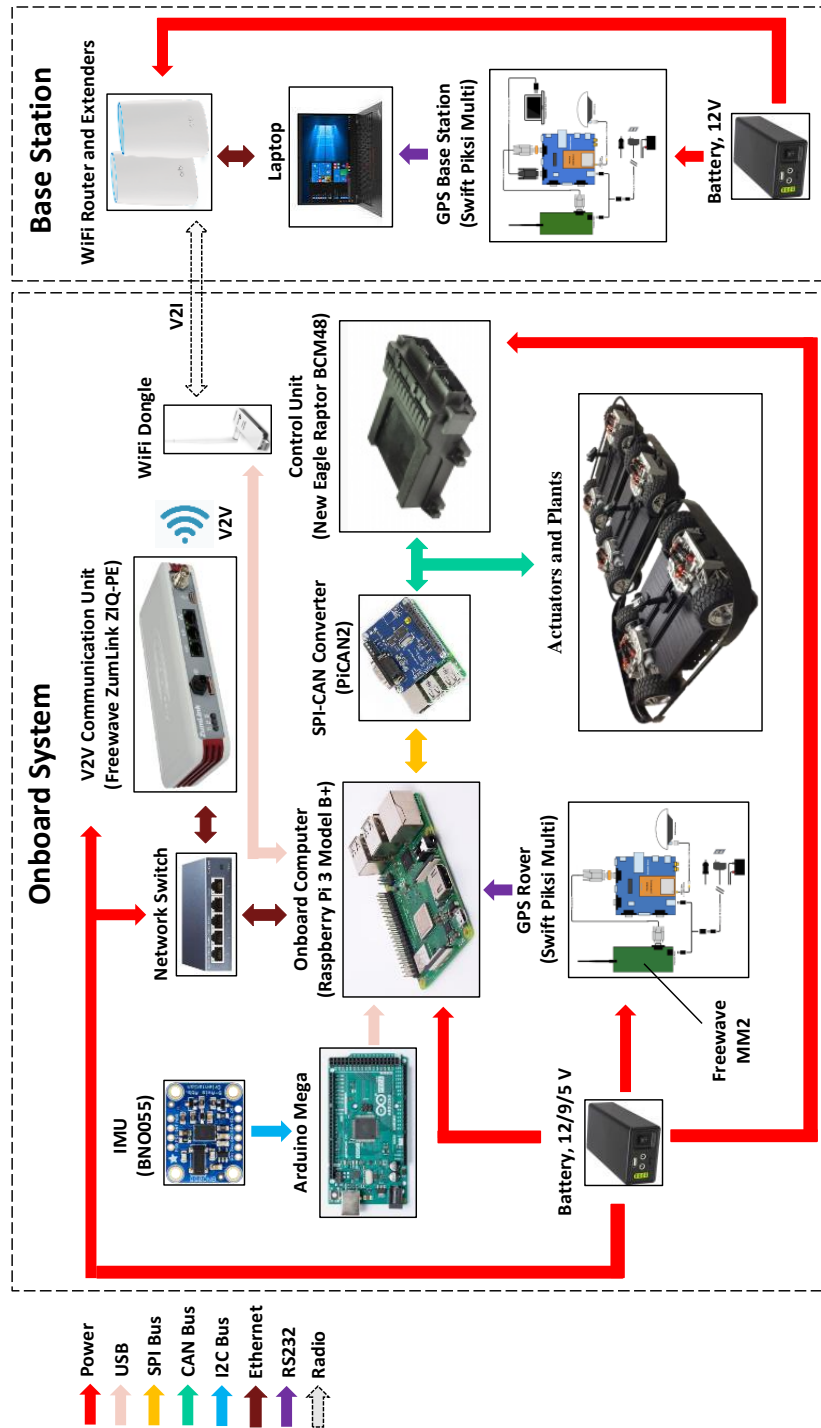
Figure 43. Power and control configuration of scaled vehicle platform prototype.
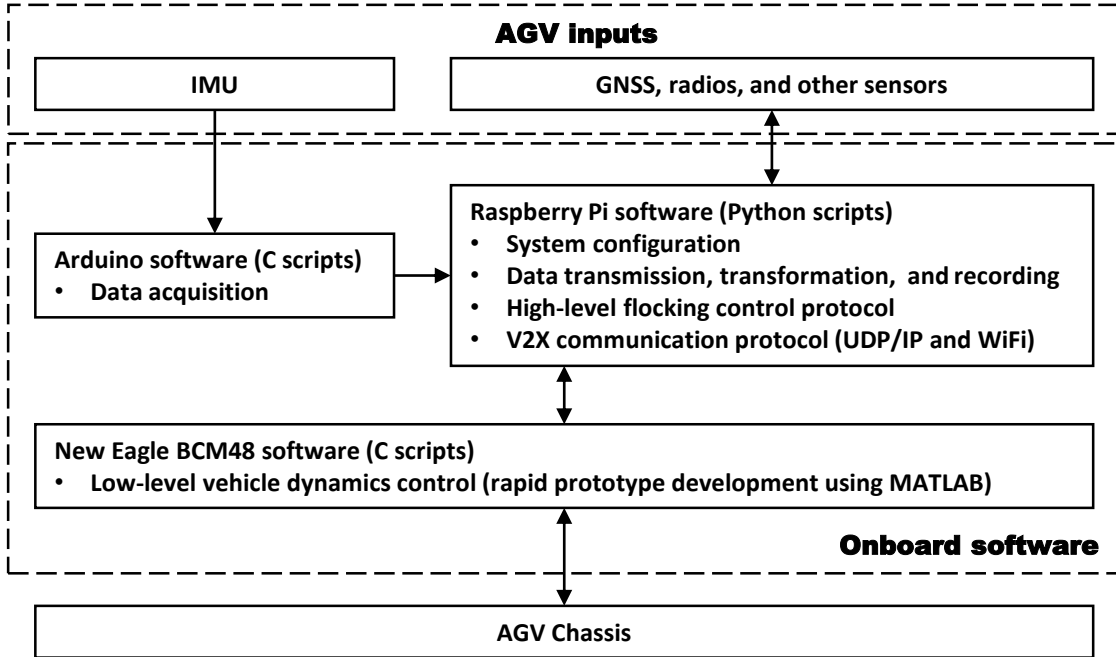
Figure 44. Onboard software configuration of scaled vehicle platform prototype.

the second case, three CAVs are required to track a unique virtual leader constrained by two boundary walls (β-agents) located at X = 3.5 m and X = 9.5 m, respectively. The third case employs two γ-agents, and different CAVs are asked to track different γ-agent in a space constrained by two walls introduced in the second case.

In the first and second cases, the unique γ-agent travels along the straight line Y = 6.5 m with speed 1.5 m/s. In the third case, two γ-agents travel along with two straight lines at Y = 5 m and Y = 8 m, respectively. All of other parameter values of flocking control are listed in Table 4.

Table 4. Parameter values of flocking control in experiments

Category	Values
c_α	0.08
c_β	0.15
c_γ	0.2
d_α	3.0 m
r_α	5.0 m
r_β	1.5 m
h	0.5
a	5
b	5
σ	0.1

5.3 Experiment Results and Discussions

The maneuvers of scaled CAVs in experiments are presented in Fig. 45, which implies lattice formation, collision avoidance among vehicles, and virtual leader position tracking. In Fig. 45 (a), it can be seen that the desired α-lattice is gradually formed in free flocking around the given γ-agent at Y = 6.5. Moreover, there is no collision, otherwise, three CAVs cannot have smooth path trajectories. Compared with free flocking, the maneuvers of the constrained flocking case, as shown in Fig. 45 (b), are affected by two walls, which force three CAVs to follow the γ-agent on a straight line. The chain-like lattice is also confirmed by the simulation results presented in Fig. 35. The multiple γ-agent tracking maneuvers are shown in Fig. 45 (c), which further verifies that the proposed hierarchical flocking control framework for CAV systems is competent for multiple γ-agent tracking without collision.

The detailed speed consensus, high-level flocking control inputs, and low-level vehicle real control inputs are presented in Fig. 46, 47, 48, and 49. Note that only the results of the constrained flocking case are exhibited as a paradigm. The desired

108
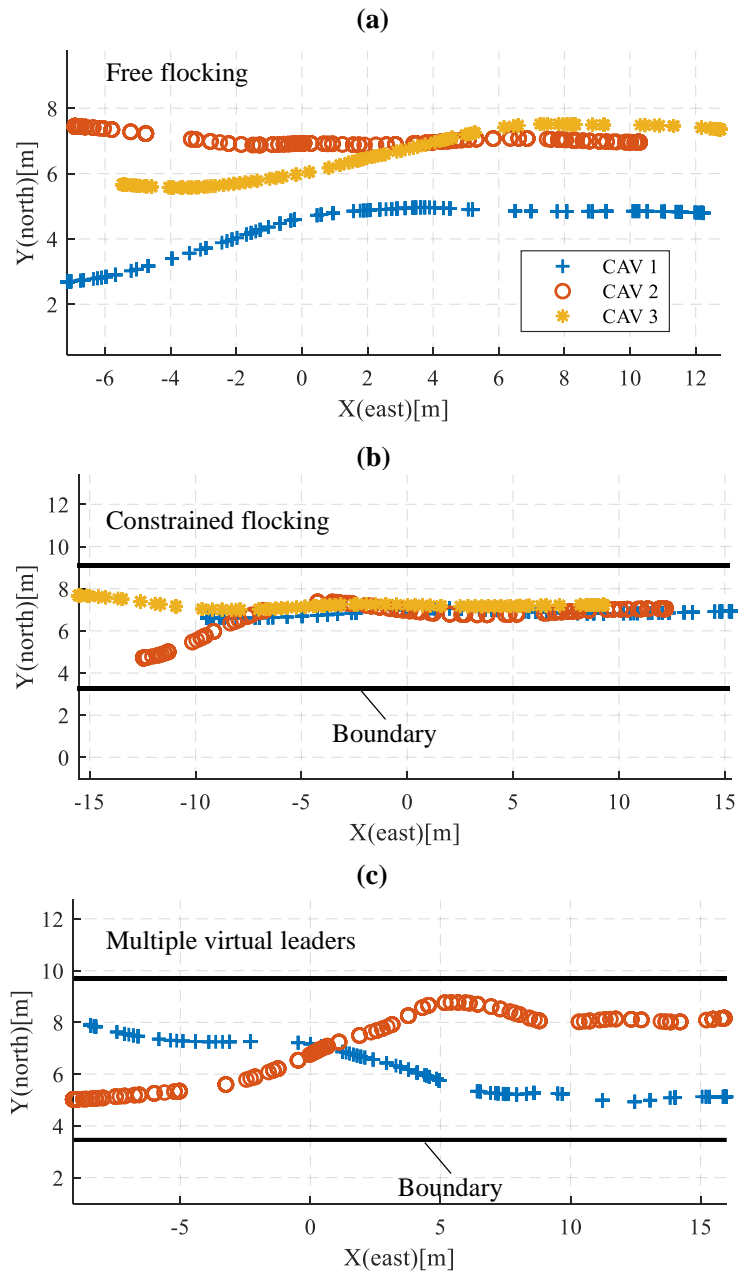
Figure 45. Maneuvers of scaled CAVs in experiments.

speed of CAVs is 1.5 m/s along the line Y = 6.5 m. Namely, the desired longitudinal speed of each CAV is 1.5 m/s, and the lateral speed should be zero. The speed consensus performance of CAVs is presented in Fig. 46, which implies that the desired longitudinal and lateral speeds are achieved. Thus, the speed consensus among three CAVs and the virtual leader is successfully performed.

Based on the double-integer node dynamics, the high-level flocking control inputs actually can be recognized as the required acceleration. As indicated in Table 3, the maximum acceleration of each CAV is 9 m/s^2. The maximum value of the high-level flocking control inputs generated during the experiment is 0.85 m/s^2. The low-level vehicle real control inputs, including steering angles and wheel torques, are plotted in Fig. 48 and 49, which indicate that the proposed framework can successfully command appropriate feedback control efforts. Therefore, the high-level flocking control and the low-level vehicle dynamics control do not violate the capability of each CAV. Furthermore, the values of flocking parameters listed in Table 4 is also practical and reasonable.

5.4   Conclusions

This chapter introduces the development of scaled CAVs, and the experiments are carried out as well. The experiment results further demonstrate that the proposed hierarchical flocking control framework works well on real vehicles.
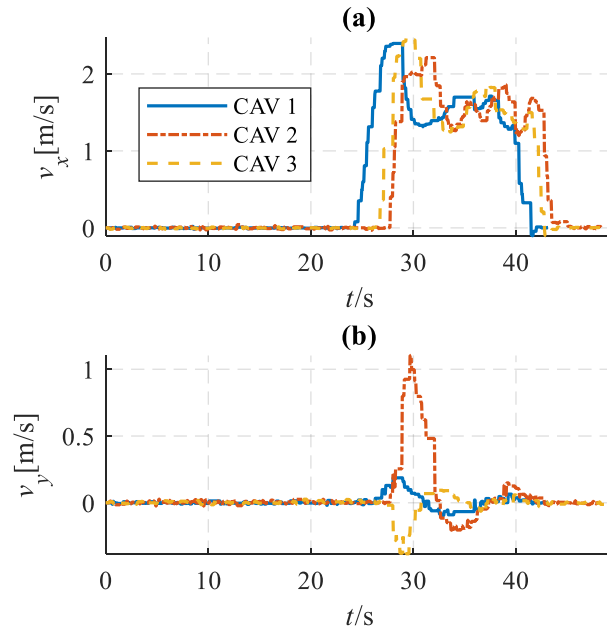
Figure 46. Speed trajectories of scaled CAVs in the constrained flocking case.
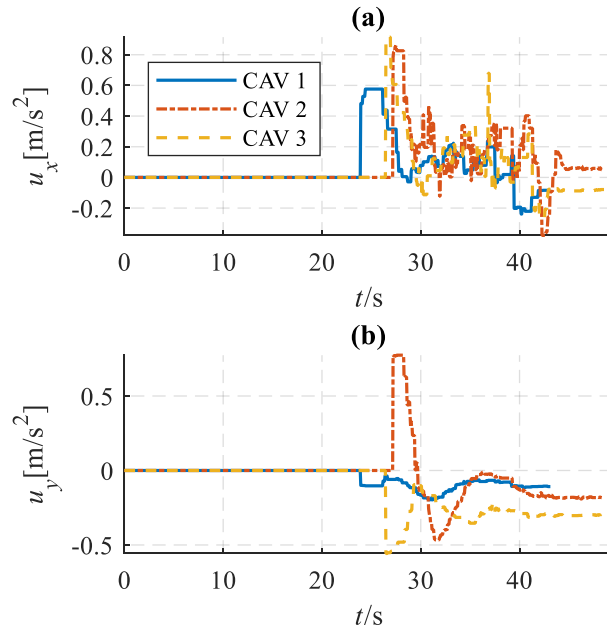
Figure 47. High-level flocking control inputs of scaled CAVs in the constrained flocking case.
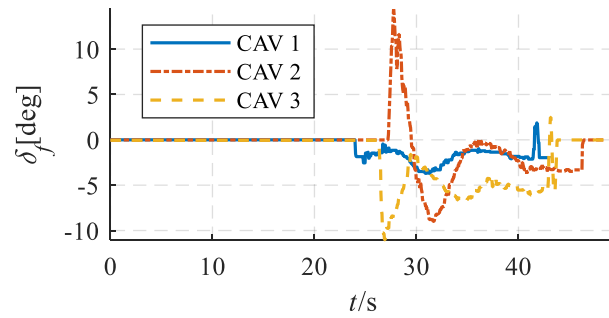
Figure 48. Steering angles of scaled CAVs in the constrained flocking case.
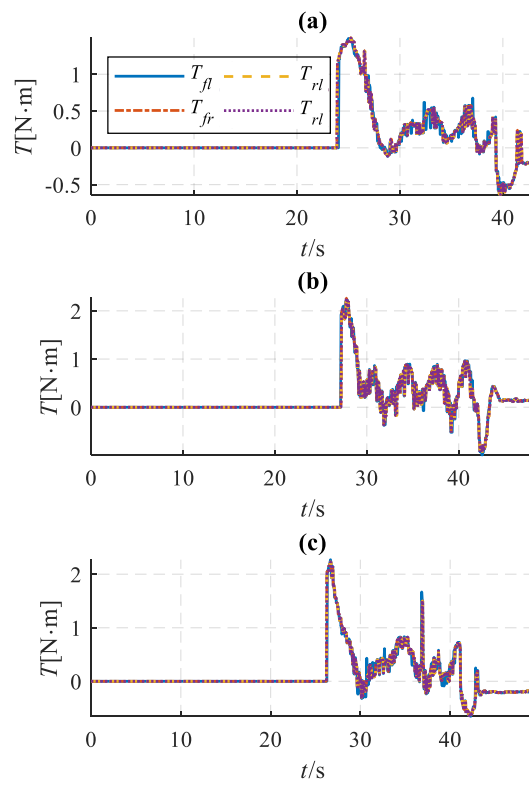
Figure 49. Wheel torques of scaled CAVs in the constrained flocking case.

Chapter 6

CONCLUSIONS AND FUTURE WORK

6.1   Conclusions

In this dissertation, a novel hierarchical flocking control framework is proposed to coordinate CAV systems in traffic. Employing the proposed flocking control framework, the issue resulted from the NID transformation is resolved, and the advantages of vehicles with over-actuated features also become feasible for the cooperative control of CAV systems. To generalize the engineering application of flocking theory in the high level of the proposed framework, this dissertation also develops several novel flocking control protocols regarding different performances required in vehicular control, which include fast convergence, permanent obstacle avoidance, and energy efficiency. In the low-level of the proposed framework, the new feedforward control (ASPP) and feedback control with control allocation are also introduced to take advantage of extra actuators. Finally, the experiments using three scaled CAVs are conducted to validate the proposed framework.

Based on simulation results, the proposed framework, flocking control algorithms, and vehicle dynamics control methods are able to achieve the anticipated performances. In addition, the experiment results also further demonstrate the proposed framework in reality. To sum up, the contributions in this dissertation could help to promote an efficient and safe ground mobility solution for modern transportation systems.

6.2 Future Work

Although the flocking control of CAV systems brings a promising solution to reduce traffic fatality and congestion, there are still many unexplored problems that endow researchers and scientists plenty of opportunities for future research. Several interesting topics are covered as follows.

1. In the literature, most of flocking studies use rigid interaction ranges and desired inter-agent gaps, so-called rigid spacing policy (RSP). Namely, the interaction ranges and the desired inter-agent gaps around every α-agent are constant and rigid during flocking control processes regardless of the speed, heading, and relative positions of α-agents. The RSP makes it simple to design flocking control protocols and conduct stability analysis. However, the flocking geometry configuration caused by the RSP is hard to adapt to complex traffic scenarios. Furthermore, the RSP is also not able to provide appropriate control inputs to benefit flocking engineering performances. Hence, a novel spacing policy should be investigated to generalize and extend the existing flocking theory for the vehicular cooperative control of CAV systems with an adaptive inter-agent gap.

2. As an essential component in CAV systems, vehicular communication is vulnerable to the presence of various cyber-attack threats, which are inherent challenges for networked systems. Therefore, cybersecurity attracts considerable attention from many researchers and engineers as a top priority. To enhance the security and robustness of CAV systems, the detection and rejection of cyber-attack with the hierarchical flocking control framework is essential. Besides, a novel resilient flocking control by specifically considering cyber-attack threats is necessary for vehicular flocking control.

3. In this dissertation, all of the involved vehicles are assumed to be homogeneous with the same dynamics property and control capability. However, it is impossible in reality. In the future, the vehicular flocking control with heterogeneous vehicle dynamics and constrained vehicle capability should be investigated to further generalize the application of the proposed framework.

4. In this dissertation, three scaled CAVs are used for experimental demonstrations. However, the similitude analysis between a scaled CAV and a full-size vehicle is not conducted. To get more convincing experiment results, the similitude relationship, including geometric, kinematic, and dynamic similitude, needs to be further addressed. Otherwise, a group of full-size CAVs may be required to carry out road experiments.

BIBLIOGRAPHY

Alur, R. 2015. "Principles of cyber-physical systems," 1–7. MIT Press.

Arcak, M. 2007. "Passivity as a design tool for group coordination." *IEEE Transactions on Automatic Control* 52 (8): 1380–1390.

Ball, P. 2016. *Patterns in nature: why the natural world looks the way it does.* University of Chicago Press.

Black, J.M., C. Carbone, R.L. Wells, and M. Owen. 1992. "Foraging dynamics in goose flocks: the cost of living on the edge." *Animal Behaviour* 44 (1): 41–50.

Boyd, Stephen, and Lieven Vandenberghe. 2004. *Convex optimization.* Cambridge University Press.

Burke, A.F. 2007. "Batteries and ultracapacitors for electric, hybrid, and fuel cell vehicles." *Proceedings of the IEEE* 95 (4): 806–820.

Cao, Y., W. Yu, W. Ren, and G. Chen. 2012. "An overview of recent progress in the study of distributed multi-agent coordination." *IEEE Transactions on Industrial Informatics* 9 (1): 427–438.

Chen, B., and H.H. Cheng. 2010. "A review of the applications of agent technology in traffic and transportation systems." *IEEE Transactions on Intelligent Transportation Systems* 11 (2): 485–497.

Chen, Y., and J. Wang. 2013. "Adaptive energy-efficient control allocation for planar motion control of over-actuated electric ground vehicles." *IEEE Transactions on Control Systems Technology* 22 (4): 1362–1373.

Couzin, I.D., J. Krause, N.R. Franks, and S.A. Levin. 2005. "Effective leadership and decision-making in animal groups on the move." *Nature* 433 (7025): 513–516.

Couzin, I.D., J. Krause, R. James, G.D. Ruxton, and N.R. Franks. 2002. "Collective memory and spatial sorting in animal groups." *Journal of Theoretical Biology* 218 (1): 1–12.

Cucker, F., and S. Smale. 2007. "Emergent behavior in flocks." *IEEE Transactions on automatic control* 52 (5): 852–862.

Darms, M.S., P.E. Rybski, C. Baker, and C. Urmson. 2009. "Obstacle detection and tracking for the Urban Challenge." *IEEE Transactions on Intelligent Transportation Systems* 10 (3): 475–485. doi:10.1109/TITS.2009.2018319.

Desjardins, C., and B. Chaib-Draa. 2011. "Cooperative adaptive cruise control: A reinforcement learning approach." *IEEE Transactions on Intelligent Transportation Systems* 12 (4): 1248–1260. doi:10.1109/TITS.2011.2157145.

Diba, F., and E. Esmailzadeh. 2012. "Dynamic performance enhancement of vehicles with controlled momentum wheel system." In *Proceedings of the 2012 American Control Conference,* 6539–6544. IEEE.

Ding, N., and S. Taheri. 2010. "A modified Dugoff tire model for combined-slip forces." *Tire Science and Technology* 38 (3): 228–244.

Dunbar, W.B., and R.M. Murray. 2006. "Distributed receding horizon control for multi-vehicle formation stabilization." *Automatica* 42 (4): 549–558.

Falcone, P., F. Borrelli, J. Asgari, H.E. Tseng, and D. Hrovat. 2007. "Predictive active steering control for autonomous vehicle systems." *IEEE Transactions on Control Systems Technology* 15 (3): 566–580.

Feng, K.T., H.S. Tan, and M. Tomizuka. 1998. "Automatic steering control of vehicle lateral motion with the effect of roll dynamics." In *Proceedings of the 1998 American Control Conference,* 4:2248–2252. IEEE.

Fernandes, P., and U. Nunes. 2015. "Multiplatooning leaders positioning and cooperative behavior algorithms of communicant automated vehicles for high traffic capacity." *IEEE Transactions on Intelligent Transportation Systems* 16 (3): 1172–1187.

Geng, C., L. Mostefai, M. Dena, and Y. Hori. 2009. "Direct yaw-moment control of an in-wheel-motored electric vehicle based on body slip angle fuzzy observer." *IEEE Transactions on Industrial Electronics* 56 (5): 1411–1419.

Godsil, C., and G.F. Royle. 2013. *Algebraic graph theory.* Vol. 207 of Graduate Texts in Mathematics. Springer Science / Business Media.

Goldman, R.W., M. El-Gindy, and B.T. Kulakowski. 2001. "Rollover dynamics of road vehicles: Literature survey." *International Journal of Heavy Vehicle Systems* 8 (2): 103–141.

Goodarzi, A., F. Diba, and E. Esmailzadeh. 2014. "Innovative active vehicle safety using integrated stabilizer pendulum and direct yaw moment control." *ASME Transactions Journal of Dynamic Systems, Measurement, and Control* 136 (5).

Goodarzi, A., M. Naghibian, D. Choodan, and A. Khajepour. 2016. "Vehicle dynamics control by using a three-dimensional stabilizer pendulum system." *Vehicle System Dynamics* 54 (12): 1671–1687.

Guanetti, J., Y. Kim, and F. Borrelli. 2018. "Control of connected and automated vehicles: State of the art and future challenges." *Annual Reviews in Control* 45:18–40.

Hedrick, J.K., I.M. Tomizuka, and P. Varaiya. 1994. "Control issues in automated highway systems." *IEEE Control Systems* 14 (6): 21–32.

Hong, Y., L. Gao, D. Cheng, and J. Hu. 2007. "Lyapunov-based approach to multiagent systems with switching jointly connected interconnection." *IEEE Transactions on Automatic Control* 52 (5): 943–948.

Iftekhar, L., and R. Olfati-Saber. 2012. "Autonomous driving for vehicular networks with nonlinear dynamics." In *Proceedings of IEEE Intelligent Vehicles Symposium,* 723–729.

Jeon, S., G. Jang, H. Choi, and S. Park. 2010. "Magnetic navigation system with gradient and uniform saddle coils for the wireless manipulation of micro-robots in human blood vessels." *IEEE Transactions on Magnetics* 46 (6): 1943–1946.

Jia, D., K. Lu, J. Wang, X. Zhang, and X. Shen. 2016. "A survey on platoon-based vehicular cyber-physical systems." *IEEE Communications Surveys and Tutorials* 18 (1): 263–284.

Johansen, T.A., and T.I. Fossen. 2013. "Control allocation—A survey." *Automatica* 49 (5): 1087–1103.

Jones, L. 2017. "Driverless cars: When and where?" *Engineering & Technology* 12 (2): 36–40.

Khatib, O. 1986. "Real-time obstacle avoidance for manipulators and mobile robots." In *Autonomous Robot Vehicles,* 396–404. Springer.

Kim, Y. 2010. "Bisection algorithm of increasing algebraic connectivity by adding an edge." *IEEE Transactions on Automatic Control* 55 (1): 170–174.

Kim, Y., and M. Mesbahi. 2006. "On maximizing the second smallest eigenvalue of a state-dependent graph Laplacian." *IEEE Transactions on Automatic Control* 51 (1): 116–120.

Lee, E.A. 2008. "Cyber physical systems: Design challenges." In *Proceedings of 11th IEEE Symposium on Object/Component/Service-Oriented Real-Time Distributed Computing,* 363–369. doi:10.1109/ISORC.2008.25.

Lee, E.A., and S. A. Seshia. 2016. "Introduction to embedded systems: A cyber-physical systems approach," 1–7. MIT Press.

Li, S.E., Y. Zheng, K. Li, and J. Wang. 2015. "An overview of vehicular platoon control under the four-component framework." In *Proceedings of IEEE Intelligent Vehicles Symposium,* 286–291. August. doi:10.1109/IVS.2015.7225700.

Lim, W., S. Lee, M. Sunwoo, and K. Jo. 2018. "Hierarchical trajectory planning of an autonomous car based on the integration of a sampling and an optimization method." *IEEE Transactions on Intelligent Transportation Systems* 19 (2): 613–626. doi:10.1109/TITS.2017.2756099.

Liu, J., and A.S. Morse. 2011. "Accelerated linear iterations for distributed averaging." *Annual Reviews in Control* 35 (2): 160–165.

Liu, Y., and B. Xu. 2015. "Improved protocols and stability analysis for multivehicle cooperative autonomous systems." *IEEE Transactions on Intelligent Transportation Systems* 16 (5): 2700–2710.

Martínez-García, M., Y. Zhang, and T. Gordon. 2016. "Modeling lane keeping by a hybrid open-closed-loop pulse control scheme." *IEEE Transactions on Industrial Informatics* 12 (6): 2256–2265. doi:10.1109/TII.2016.2619064.

Mashadi, B., and M. Gowdini. 2015. "Vehicle dynamics control by using an active gyroscopic device." *ASME Transactions Journal of Dynamic Systems, Measurement, and Control* 137 (12).

Mashadi, B., M. Mokhtari-Alehashem, and H. Mostaghimi. 2016. "Active vehicle rollover control using a gyroscopic device." *Proceedings of the Institution of Mechanical Engineers, Part D: Journal of Automobile Engineering* 230 (14): 1958–1971.

Milanes, V., S.E. Shladover, J. Spring, C. Nowakowski, H. Kawazoe, and M. Nakamura. 2014. "Cooperative adaptive cruise control in real traffic situations." *IEEE Transactions on Intelligent Transportation Systems* 15 (1): 296–305.

119

Motsch, S., and E. Tadmor. 2011. "A new model for self-organized dynamics and its flocking behavior." *Journal of Statistical Physics* 144 (5): 923–947.

Murata, S. 2012. "Innovation by in-wheel-motor drive unit." *Vehicle System Dynamics* 50 (6): 807–830.

Murray, R.M. 2007. "Recent research in cooperative control of multivehicle systems." *ASME Transactions Journal of Dynamic Systems, Measurement, and Control* 129 (5): 571–583.

Nedic, A., and J. Liu. 2018. "Distributed optimization for control." *Annual Review of Control, Robotics, and Autonomous Systems* 1:77–103.

Nedic, A., and A. Ozdaglar. 2009. "Distributed subgradient methods for multi-agent optimization." *IEEE Transactions on Automatic Control* 54 (1): 48.

NHTSA's National Center for Statistics and Analysis. 2016. *2015 Motor vehicle crashes: Overview.* Technical report. National Highway Traffic Safety Administration, August.

Noori, M., S. Gardner, and O. Tatari. 2015. "Electric vehicle cost, emissions, and water footprint in the United States: Development of a regional optimization model." *Energy* 89:610–625.

———. 2018. *Global EV outlook 2018 : Towards cross-modal electrification.* Technical report. Tech. Univ. Denmark.

Okubo, A. 1986. "Dynamical aspects of animal grouping: Swarms, schools, flocks, and herds." *Advances in Biophysics* 22 (C): 1–94.

Olfati-Saber, R. 2002. "Near-identity diffeomorphisms and exponential ϵ-tracking and ϵ-stabilization of first-order nonholonomic SE(2) vehicles." In *Proceedings of the 2002 American Control Conference,* 6:4690–4695.

———. 2006. "Flocking for multi-agent dynamic systems: Algorithms and theory." *IEEE Transactions on Automatic Control* 51 (3): 401–420.

Olfati-Saber, R., and R.M. Murray. 2003. "Flocking with obstacle avoidance: Cooperation with limited communication in mobile networks," 2:2022–2028.

———. 2004. "Consensus problems in networks of agents with switching topology and time-delays." *IEEE Transactions on Automatic Control* 49 (9): 1520–1533.

Olfati-Saber, Reza, and Richard M Murray. 2003. "Flocking with obstacle avoidance: Cooperation with limited information in mobile networks." In *Proceedings of the 42nd IEEE Conference on Decision and Control,* 2:2022–2028. Citeseer, December.

Parida, N.C., S. Raha, and A. Ramani. 2014. "Rollover-preventive force synthesis at active suspensions in a vehicle performing a severe maneuver with wheels lifted off." *IEEE Transactions on Intelligent Transportation Systems* 15 (6): 2583–2594.

Peng, Y., F. Wang, S. Gurumoorthy, Y. Chen, and M. Xin. 2019. "Experimental validations on vision-based path tracking with preview four-wheel steering control." In *Proceedings of the ASME 2019 Dynamic Systems and Control Conference,* DSCC2019–9159. October.

Potsaid, B., J.T. Wen, M. Unrath, D. Watt, and M. Alpay. 2007. "High performance motion tracking control for electronic manufacturing." *ASME Transactions Journal of Dynamic Systems, Measurement and Control, Transactions of the ASME* 129 (6): 767–776. doi:10.1115/1.2789467.

Rajamani, R. 2006. *Vehicle Dynamics and Control.* Springer Science / Business Media.

Reynolds, C.W. 1987. "Flocks, herds and schools: A distributed behavioral model." *ACM SIGGRAPH Computer Graphics* 21 (4). doi:10.1145/37402.37406.

Rios-Torres, J., and A.A. Malikopoulos. 2016. "A survey on the coordination of connected and automated vehicles at intersections and merging at highway on-ramps." *IEEE Transactions on Intelligent Transportation Systems* 18 (5): 1066–1077.

Schrank, D., B. Eisele, and T. Lomax. 2019. *2019 Urban mobility report.* Technical report. Texas A&M Transportation Institute, August.

Shibahata, Y., K. Shimada, and T. Tomari. 1993. "Improvement of vehicle maneuverability by direct yaw moment control." *Vehicle System Dynamics* 22 (5-6): 465–481.

Siciliano, B., and O. Khatib. 2016. "Springer handbook of robotics," 921–928. Springer.

Siegel, J.E., D.C. Erb, and S.E. Sarma. 2017. "A survey of the connected vehicle landscape—architectures, enabling technologies, applications, and development areas." *IEEE Transactions on Intelligent Transportation Systems* 19 (8): 2391–2406.

Sivaraman, S., and M.M. Trivedi. 2013. "Looking at vehicles on the road: A survey of vision-based vehicle detection, tracking, and behavior analysis." *IEEE Transactions on Intelligent Transportation Systems* 14 (4): 1773–1795. doi:10.1109/TITS. 2013.2266661.

Solmaz, S., M. Corless, and R. Shorten. 2007. "A methodology for the design of robust rollover prevention controllers for automotive vehicles with active steering." *International Journal of Control* 80 (11): 1763–1779.

Su, H., X. Wang, and Z. Lin. 2009. "Flocking of multi-agents with a virtual leader." *IEEE Transactions on Automatic Control* 54 (2): 293–307.

Su, H., X. Wang, and W. Yang. 2008. "Flocking in multi-agent systems with multiple virtual leaders." *Asian Journal of Control* 10 (2): 238–245.

Tamaki, Y. 1999. "Reserch into achieving a lightweight vehicle body utilizing structure optimizing analysis: aim for a lightweight and high and rigid vehicle body." *JSAE Review* 20 (4): 558–561.

Tanner, H.G. 2007. "Switched UAV-UGV cooperation scheme for target detection." In *Proceedings of IEEE International Conference on Robotics and Automation,* 3457–3462.

Tanner, H.G., A. Jadbabaie, and G.J. Pappas. 2003. "Stable flocking of mobile agents part II: Dynamic topology." In *Proceedings of the IEEE Conference on Decision and Control,* 2:2016–2021.

———. 2007. "Flocking in fixed and switching networks." *IEEE Transactions on Automatic Control* 52 (5): 863–868.

Tjonnas, J., and T.A. Johansen. 2009. "Stabilization of automotive vehicles using active steering and adaptive brake control allocation." *IEEE Transactions on Control Systems Technology* 18 (3): 545–558.

Toner, J., and Y. Tu. 1998. "Flocks, herds, and schools: A quantitative theory of flocking." *Physical Review E - Statistical Physics, Plasmas, Fluids, and Related Interdisciplinary Topics* 58 (4): 4828–4858.

Turgut, A.E., H. Çelikkanat, F. Gökçe, and E. Şahin. 2008. "Self-organized flocking in mobile robot swarms." *Swarm Intelligence* 2 (2-4): 97–120.

Vahidi, A., and A. Eskandarian. 2003. "Research advances in intelligent collision avoidance and adaptive cruise control." *IEEE Transactions on Intelligent Transportation Systems* 4 (3): 143–153.

Van Arem, B., C.J. Van Driel, and R. Visser. 2006. "The impact of cooperative adaptive cruise control on traffic-flow characteristics." *IEEE Transactions on Intelligent Transportation Systems* 7 (4): 429–436.

Vásárhelyi, Gábor, Csaba Virágh, Gergő Somorjai, Tamás Nepusz, Agoston E Eiben, and Tamás Vicsek. 2018. "Optimized flocking of autonomous drones in confined environments." *Science Robotics* 3 (20): eaat3536.

Vicsek, T., A. Czirók, E. Ben-Jacob, I. Cohen, and O. Shochet. 1995. "Novel type of phase transition in a system of self-driven particles." *Physical Review Letters* 75 (6): 1226.

Wada, M. 2009. "Research and development of electric vehicles for clean transportation." *Journal of Environmental Sciences* 21 (6): 745–749.

Wang, F., and Y. Chen. 2017a. "Detection of vehicle tripped and untripped rollovers by a novel index with mass-center-position estimations." In *Proceedings of the ASME 2017 Dynamic Systems and Control Conference,* DSCC2017–5149. October.

———. 2017b. "Vehicle rollover prevention through a novel active rollover preventer." In *Proceedings of the ASME 2017 Dynamic Systems and Control Conference,* DSCC2017–5146. October.

———. 2017c. "Vehicle safety enhancement through a novel active yaw moment stabilizer." In *Proceedings of the ASME 2017 Dynamic Systems and Control Conference,* 5556–5561. May.

———. 2018a. "A novel autonomous trajectory control for vehicular cyber-physical systems with flocking control algorithms." In *Proceedings of the 2018 American Control Conference,* 5076–5081. June.

———. 2018b. "Dynamics and control of a novel active yaw stabilizer to enhance vehicle lateral motion stability." *ASME Transactions Journal of Dynamic Systems, Measurement, and Control* 140 (8).

———. 2018c. "Hierarchical input-output decoupling control for vehicle rollover mitigation." In *Proceedings of the ASME 2018 Dynamic Systems and Control Conference,* DSCC2018–9166. October.

Wang, F., and Y. Chen. 2019a. "A novel active rollover prevention for ground vehicles based on continuous roll motion detection." *ASME Transactions Journal of Dynamic Systems, Measurement, and Control* 141 (1).

————. 2019b. "Energy-efficient flocking control: a distributed least-informed method." In *Proceedings of 2019 IEEE Conference on Control Technology and Applications,* 332–337. August.

————. 2019c. "Vehicle rollover propensity detection based on a mass-center-position metric: A continuous and completed method." *IEEE Transactions on Vehicular Technology* 68 (9): 8652–8662.

————. 2020a. "A novel hierarchical flocking control framework for vehicular cyber-physical systems." *IEEE Transactions on Intelligent Transportation Systems.* doi:10.1109/TITS.2020.2986436.

————. 2020b. "Fast-convergence flocking control for multi-agent systems with switching communication topology." In *Proceedings of the 2020 American Control Conference.* July.

Wang, F., P. Xu, A. Li, and Y. Chen. 2019. "Energy optimization of lateral motions for autonomous ground vehicles with four-wheel steering control." In *Proceedings of the ASME 2019 Dynamic Systems and Control Conference,* DSCC2019–9003. October.

Wang, H., H. Kong, Z. Man, D.M. Tuan, Z. Cao, and W. Shen. 2014. "Sliding mode control for steer-by-wire systems with AC motors in road vehicles." *IEEE Transactions on Industrial Electronics* 61 (3): 1596–1611.

Wang, W., and H. Peng. 2012. "Flocking control with communication noise based on second-order distributed consensus algorithm." In *Proceedings of Power Engineering and Automation Conference.*

Wang, X., J. Qin, and C. Yu. 2014. "ISS method for coordination control of nonlinear dynamical agents under directed topology." *IEEE Transactions on Cybernetics* 44 (10): 1832–1845.

World Health Organization. 2018. *Global status report on road safety 2018.* Technical report. World Health Organization.

Xiao, L., and S. Boyd. 2004. "Fast linear iterations for distributed averaging." *Systems and Control Letters* 53 (1): 65–78.

Xu, L., G. Yin, T. Liu, N. Zhang, J. Chen, and N. Chen. 2016. "The optimized flocking-based vehicle fleet control considering vehicular dynamic process." In *Proceedings of 2016 IEEE Vehicle Power and Propulsion Conference.*

Yim, S. 2011. "Design of a preview controller for vehicle rollover prevention." *IEEE Transactions on Vehicular Technology* 60 (9): 4217–4226.

Yim, S., Y. Park, and K. Yi. 2010. "Design of active suspension and electronic stability program for rollover prevention." *International Journal of Automotive Technology* 11 (2): 147–153.

Yoon, J., W. Cho, J. Kang, B. Koo, and K. Yi. 2010. "Design and evaluation of a unified chassis control system for rollover prevention and vehicle stability improvement on a virtual test track." *Control Engineering Practice* 18 (6): 585–597.

Yoon, J., D. Kim, and K. Yi. 2007. "Design of a rollover index-based vehicle stability control scheme." *Vehicle System Dynamics* 45 (5): 459–475.

Yu, W., G. Chen, and M. Cao. 2010. "Distributed leader-follower flocking control for multi-agent dynamical systems with time-varying velocities." *Systems & Control Letters* 59 (9): 543–552.

Zhang, Q., Z. Gong, Z. Yang, and Z. Chen. 2019. "Distributed convex optimization for flocking of nonlinear multi-agent systems." *International Journal of Control, Automation and Systems* 17 (5): 1177–1183.

Zheng, B., and S. Anwar. 2009. "Yaw stability control of a steer-by-wire equipped vehicle via active front wheel steering." *Mechatronics* 19 (6): 799–804.

APPENDIX A

VEHICLE DYNAMICS AND CONTROL WITH OVER-ACTUATED FEATURES

A.1 Overview

Benefited by the advancement of vehicular electrification, a set of redundant actuators can provide over-actuated features to further improve vehicle safety and efficiency via vehicle dynamics control. To promote the application of over-actuated vehicles, two main aspects of vehicle dynamics control are investigated in this chapter. On the one hand, an essential task for vehicle dynamics control is vehicle planar and roll motion stability maintenance under critical driving maneuvers. On the other hand, saving vehicle operation energy is also an essential task regarding vehicle both longitudinal and lateral motions. The detailed contributions of this chapter are summarized as follows [4].

1. A novel active yaw stabilizer (AYS) system is proposed for improving vehicle lateral stability control. The introduced AYS, inspired by the recent IWM technology, has two degrees-of-freedom with independent self-rotating and orbiting movements. The dynamic model of the AYS is first developed. The capability of the AYS is then investigated to show its maximum generation of corrective lateral forces and yaw moments, given a limited vehicle space. Utilizing the high-level Lyapunov-based control design and the low-level control allocation design, a hierarchical control architecture is established to integrate the AYS control with AFS and DYC. To demonstrate the advantages of the AYS, generating corrective lateral force and yaw moment without relying on tire-road interaction, double-lane change maneuvers are studied on road with various tire-road friction coefficients.

2. To give continuous and completed rollover information, this chapter presents a novel rollover index based on a mass-center-position (MCP) metric. The MCP is first determined by estimating the positions of the center of mass of the vehicle, which consists of one sprung mass and two unsprung masses with two switchable roll motion models, before and after tire liftoff. The roll motion information can then be provided through the MCP continuously without saturation for both tripped and untripped rollovers. Moreover, to describe the completed rollover status, different criteria are derived from D'Alembert's principle and the moment balance conditions based on the MCP. In addition to tire liftoff, three new rollover statuses, "rollover threshold," "rollover," and vehicle jumping "in the air," can be all identified by the proposed criteria.

3. To enhance the performance of vehicle rollover detection and prevention, a novel control strategy integrating the MCP metric and the active rollover preventer (ARPer) system is proposed. The applied MCP metric can provide completed

---

[4]The main content of this appendix is based on the author's works in (Wang and Chen 2017c, 2018b, 2019c, 2019a, 2017b, 2017a)

rollover information without saturation in the case of tire lift-off. Based on the continuous roll motion detection provided by the MCP metric, the proposed ARPer system can generate corrective control efforts independent to tire-road interactions. Moreover, the capability of the ARPer system is investigated for the given vehicle physical spatial constraints. A hierarchical control architecture is also designed for tracking desired accelerations derived from the MCP metric and allocating control efforts to the ARPer system and AFS control.

A.2 Lateral Stability Maintenance with Active Yaw Stabilizer

To achieve effective vehicle lateral/yaw stabilization, two categories of vehicle active control systems can be classified based on different principles to generate corrective lateral forces or yaw moments. The first category is based on the interaction between tire and road, which produces corrective lateral forces or yaw moment by directly changing the tire lateral friction forces, such as active steering control (ASC) (Zheng and Anwar 2009; Falcone et al. 2007), or by redistributing tire longitudinal friction forces, such as direct yaw moment control (DYC) (Shibahata, Shimada, and Tomari 1993; Geng et al. 2009). On a high friction coefficient (high-μ) or uniform friction coefficient road, ASC and DYC are effective and perform well. However, on a low-μ or split-μ road, ASC and DYC are not able to generate appropriate corrective lateral force or yaw moment under certain critical driving conditions.

To overcome the aforementioned disadvantages of ASC and DYC, the other category of control methods introduces extra corrective yaw moments and lateral forces independent to tire-road interaction by utilizing a controlled moving or rotating mass in vehicles, such as an active gyroscope (Mashadi and Gowdini 2015), a controlled momentum wheel system (Diba and Esmailzadeh 2012) and a stabilizer pendulum (Goodarzi, Diba, and Esmailzadeh 2014; Goodarzi et al. 2016). By controlling a moving or rotating mass, the interactions, a force and a moment, between a vehicle and the mass act as external corrective efforts for maintaining vehicle lateral/yaw stability. Although a moving or rotating mass can introduce forces and moments independent to tire-road friction conditions, the added extra mass requires certain rooms to hold an additional object, which does not benefit the lightweight and compact layout of modern vehicles (Tamaki 1999). Thus, the capabilities of these systems are limited by object masses and installation spaces.

Inspired by the latest electrical actuation and control technology for electric vehicles with IWMs, this section proposes a novel active yaw stabilizer (AYS) system, mainly consisting of an electric motor and an orbit, to produce corrective yaw moments and lateral forces within the available spaces of vehicles. For an electric vehicle driven by IWMs, a spare wheel utilizing an IWM can be applied as the electric motor in the proposed AYS system without additional space requirements. Moreover, the battery
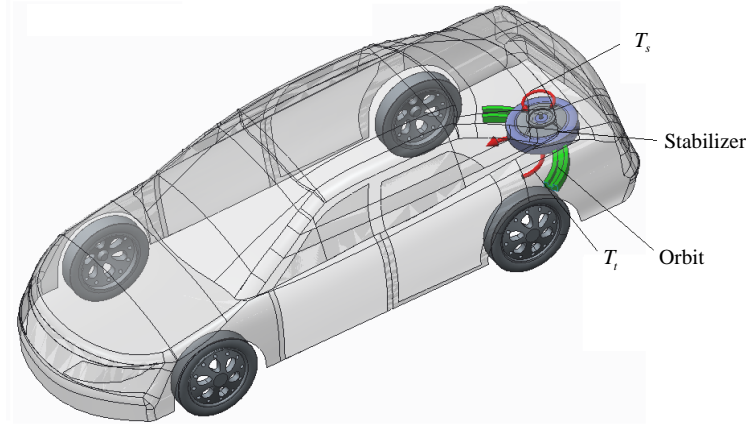
Figure 50. Illustration of the proposed AYS on a vehicle.

system in the electric vehicle can also be utilized to power the AYS to assist vehicle lateral dynamics stabilization without significantly increasing vehicle complexity and weight. The sketch of a vehicle equipped with the proposed AYS is shown in Fig. 50, where T_s and T_t are two driving torques that make the motor self-rotating and orbiting, respectively. Therefore, the electric motor in the proposed AYS can rotate and move along with the orbit simultaneously, which stands for two additional corrective yaw moment and lateral force sources.

A.2.1   Modeling of Vehicle Lateral and Yaw Motion with Active Yaw Stabilizer

A 4-wheel vehicle model for lateral dynamics is adopted in this section. Equipped with the proposed AYS system, the vehicle model with AYS is shown in Fig. 51. The local frame X-Y is fixed at the CG of the vehicle. Within Fig. 51, θ and γ denote two stabilizer position angles with respect to the centers of orbit and CG (they are not necessary at the same location), respectively; L_c is the distance from the middle point of the orbit to CG; ω_s and ω_t denote the orbiting angular speed and self-rotating angular speed, respectively; R denotes the radius of orbit; l_x and l_y represent the longitudinal and lateral distance from the stabilizer to the CG of the vehicle, respectively.

The vehicle state-space model can be written as (A.1).

$$\dot{x} = \begin{bmatrix} 0 & -1 \\ 0 & 0 \end{bmatrix} x + \begin{bmatrix} \frac{1}{Mv_x} & 0 \\ 0 & \frac{1}{I_z} \end{bmatrix} \tau_c + \begin{bmatrix} \frac{F_{fl}+F_{fr}+F_{rl}+F_{rr}}{Mv_x} \\ \frac{(F_{fl}+F_{fr})L_f-(F_{rl}+F_{rr})L_r}{I_z} \end{bmatrix}, \qquad (A.1)$$
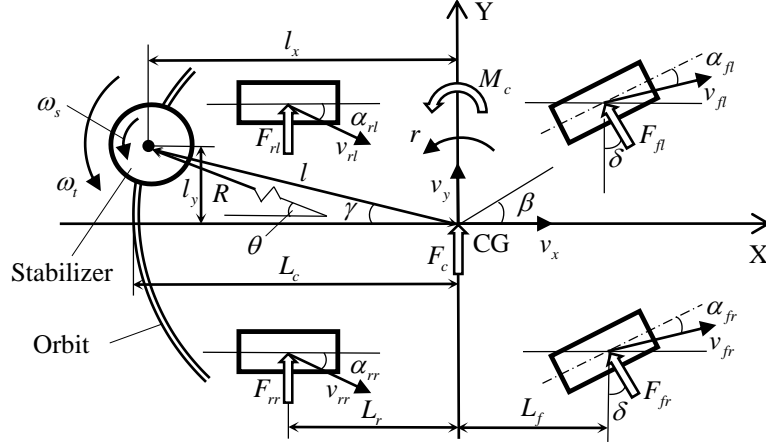
Figure 51. Four-wheel vehicle lateral motion model with the proposed AYS.

where $x = [\beta, r]^{\mathrm{T}}$ denotes vehicle states, and $\tau_c = [F_c, M_c]^{\mathrm{T}}$ denotes the virtual control inputs that are generated via AYS, DYC, or ASC systems. Moreover, lateral tire forces $F_{fl,fr,rl,rr}$ in (A.1) are determined by the Magic formula tire model, which integrates the effects of tire vertical load transfer, tire slip ratio, tire-road coefficient, and the coupling between lateral friction forces and longitudinal friction forces (Rajamani 2006).

From Fig. 51, the system of the vehicle equipped the AYS is a multibody dynamic system. Therefore, the corrective lateral force F_{AYS} and yaw moment M_{AYS} are introduced by the reaction force and moment resulted from the AYS, which are presented as (A.2).

$$\begin{cases} F_{AYS} = -ma_{sy} \\ M_{AYS} = -T_s + m(a_{sy}l_x + a_{sx}l_y) \end{cases}, \tag{A.2}$$

where m denotes the stabilizer mass; a_{sy} and a_{sx} denote the lateral and longitudinal acceleration of stabilizer with respect to the local frame fixed on the vehicle body.

Due to the rotation of the vehicle local frame, three accelerations, including transport acceleration a_e, relative acceleration a_r, and Coriolis acceleration a_c, are involved. The decomposition of these accelerations are presented in Fig. 52, where (a_{rt}, a_{rn}) and (a_{et}, a_{en}) are the tangential and normal decomposition of a_r and the rotational portion of a_e, respectively, and (a_{ex}, a_{ey}) is the orthogonal decomposition of the translational portion of a_e. Each acceleration decomposition could be determined
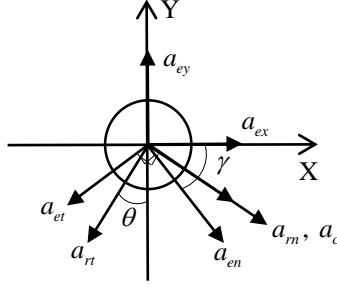
Figure 52. Stabilizer acceleration decomposition.

through the equation given below:

$$
\begin{cases}
a_{ex} = \dot{v}_x - v_y r \\
a_{ey} = \dot{v}_y - v_x r \\
a_{et} = \dot{r}l \\
a_{en} = \dot{r}^2 l \\
a_{rt} = \dot{\omega}_t R \\
a_{rn} = \dot{\omega}_t^2 R \\
a_c = 2r\omega_t R
\end{cases}
\qquad . \tag{A.3}
$$

Thus, a_{sy} and a_{sx} could be rewritten as (A.4) based on Fig. 52, and the corrective lateral force F_{AYS} and yaw moment M_{AYS} introduced by the AYS are obtained as (A.5) by substituting (A.3) and (A.4) into a_{sy} and a_{sx} in (A.2).

$$
\begin{cases}
a_{sx} = a_{ex} + a_{en} \cos\gamma + (a_{rn} + a_c)\cos\theta - a_{et}\sin\gamma - a_{rt}\sin\theta \\
a_{sy} = a_{ey} - a_{en}\sin\gamma - (a_{rn} + a_c)\sin\theta - a_{et}\cos\gamma - a_{rt}\cosh\theta
\end{cases}
\qquad . \tag{A.4}
$$

$$
\begin{cases}
F_{AYS} = \underbrace{-m(v_x(\dot{\beta} + r) - \dot{r}l\cos\gamma - r^2 l \sin\gamma)}_{f_1} \\[2ex]
\quad + \underbrace{-m(-\omega_t^2 R \sin\theta - \dot{\omega}_t R \cos\theta)}_{f_2} \\[2ex]
\quad + \underbrace{2mr\omega_t R \sin\theta}_{f_3} \\[1ex]
M_{AYS} = -\omega_s I_s \\[1ex]
\quad + \underbrace{\begin{aligned}&m(l_x(v_x(\dot{\beta}+r) - \dot{r}l\cos\gamma - r^2 l \sin\gamma) \\ &\quad + (-v_x\beta r - \dot{r}l\sin\gamma + r^2 l \sin\gamma)l_y)\end{aligned}}_{t_1} \\[3ex]
\quad + \underbrace{m(l_x(-\omega_t^2 R \sin\theta - \dot{\omega}_t R \cos\theta) + (\omega_t^2 R \cos\theta - \dot{\omega}_t R \sin\theta)l_y)}_{t_2} \\[2ex]
\quad + \underbrace{m((-2r\omega_t R \sin\theta)l_x + (2r\omega_t R \cos\theta)l_y)}_{t_3} \\[2ex]
\dot{\omega}_t = \dfrac{T_t}{I_t} \\[1.5ex]
\dot{\omega}_s = \dfrac{T_s}{I_s}
\end{cases}
\qquad , \qquad \text{(A.5)}
$$

where T_s and T_t represent two torques that drive the motor self-rotating and orbiting, respectively; I_s and I_t denote two moments of inertia of stabilizer when it rotates or orbits, respectively. Both FAYS and MAYS in (A.5) include three items: f_1 and t_1 describe the sum of efforts related to vehicle states; f_2 and t_2 represent efforts mainly related to the AYS orbiting states; f_3 and t_3 denote the sum of efforts related to the coupling of vehicle states and stabilizer orbiting states. Physically, these three items are all variables with respect to the mass and position of stabilizer.

A.2.2   Evaluation of the Capability of Active Yaw Stabilizer

Before applying the proposed AYS to enhance the vehicle lateral stability control, the capability of the novel AYS system needs to be first evaluated, considering the limited vehicle space for the proposed AYS design. Based on (A.5), various factors can influence the corrective lateral force and yaw moment introducedd by the AYS. For example, stabilizer states ω_s and ω_t, controlled by T_s and T_t, may influence the maximum values of the introduced force and moment. Vehicle states, including β and r, also have contributions in the production of F_{AYS} and M_{AYS}. Different from these time-varying variables interacted with the control efforts, the predefined design parameters of the proposed AYS system that influence the AYS capability, including R, m, $\max[l_x]$, and $\max[l_y]$, are mainly discussed to consider the limited space in vehicles. Within the design parameters, m, $\max[l_x]$, and $\max[l_y]$ are limited by the property

of the stabilizer and vehicle spare space, which have less ranges to be adjusted. As a result, only R is the main variable to determine the orbit shape that can largely influence F_{AYS} and M_{AYS}. One typical case is studied here to show the potential of F_{AYS} and M_{AYS} with respect to different values of R, given certain stabilizer and vehicle states and other design parameters.

Most variables and their values used in the capability study are listed in Table 5, where all values related to the vehicle are obtained from CarSim® B-class sports car examples. Based on characteristics of an electric motor, which was applied as an in-wheel motor (Geng et al. 2009), the maximum of T_s is assumed as large as 80 N·m. The actuator used to orbit the stabilizer is assumed to provide T_t as large as 100 N·m. Based on the maximum tangential propulsion and the mass of the stabilizer, the tangential acceleration along the orbit can reach as high as 4 m/s². While $\dot{\omega}_s$ is kept as zero for this evaluation because the effect of $\dot{\omega}_s$ could be simply considered by adding the maximum of T_s to M_{AYS}. Given each specific value of R and other parameters shown in Table 5, an open-loop simulation with a step steering angle at 5 degrees is applied to the vehicle. The maximum absolute values of F_{AYS} and M_{AYS} are recorded for each test value of R.

Table 5. Variables in capability study

Variable	Values
v_x	90 km/h
m	25 kg
δ_f	5 deg (step signal)
M	1,020 kg
I_z	1,020 kg·m²
L_f	1.165 m
L_r	1.165 m
$\max[l_x]$	1 m
$\max[l_y]$	1.5 m

The maximum absolute values of F_{AYS} and M_{AYS}, denoted by $\max[|F_{AYS}|]$ and $\max[|M_{AYS}|]$, with respect to varying are shown in Fig. 53. The signs of $\max[F_{AYS}]$ and $\max[M_{AYS}]$ may be changed by different directions of ω_s and $\dot{\omega}_s$, so that the absolute values are adopted to evaluate the AYS capability without considering moving directions of the AYS. In Fig. 53, plots (a) and (c) are obtained when the stabilizer moves towards the same direction as the steering angle, and plots (b) and (d) are obtained when the stabilizer moves towards the opposite direction of the steering angle to cover all situations with possible orbiting directions of the stabilizer.
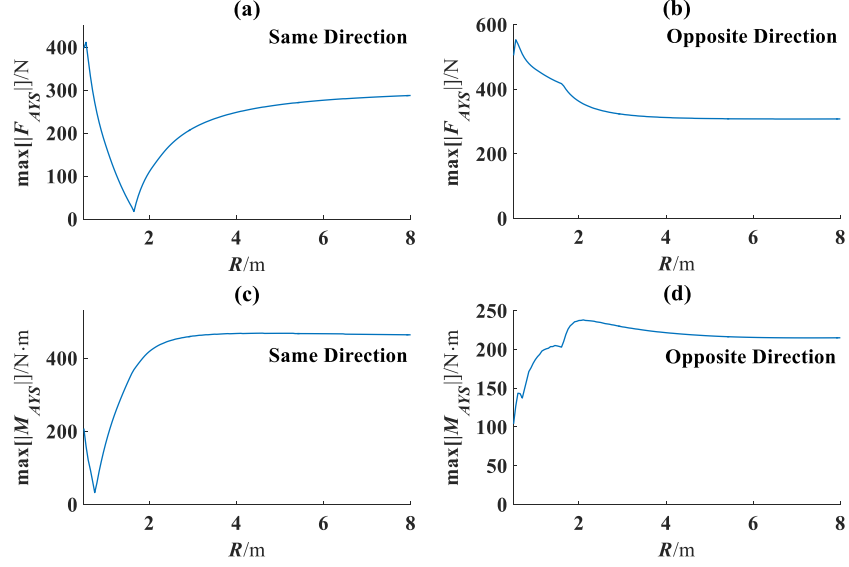
Figure 53. Maximum $|F_{AYS}|$ and $|M_{AYS}|$ curve with respect to variable R.

Considering achieving maximum values of F_{AYS} and M_{AYS} simultaneously (without scarifying one with the other maximized), when R is about 3 m, F_{AYS} and M_{AYS} can achieve their maximum values at 380 N and 470 N $\cdot$ m respectively in the same direction case, according to Fig. 53. Adding the maximum T_s to the moment, the overall capability of this novel AYS can provide the maximum correct lateral force at 380 N and yaw moment at 550 N $\cdot$ m. Based on the capability analyses, the achievable corrective lateral force and yaw moment of the proposed AYS system, within the available vehicle space, can provide considerable complementation to existing vehicle lateral dynamics control methods, such as ASC or DYC. Considering the fact that the introduced corrective lateral force and yaw moment are independent to tire-road friction forces, the AYS will provide significant support for vehicle lateral stabilization especially on low-μ or split-μ road.

A.2.3   Controller Design

With the evaluated capability of AYS, the control design used to integrate the proposed AYS system with existing vehicle lateral dynamics control methods is discussed in this section. The overview of the hierarchical control architecture of the vehicle lateral dynamics is presented in Fig. 54. Since the integration of AYS with AFS or DYC is considered to stabilize the vehicle lateral dynamics, the number of low-level control actuation u_d is more than that of required high-level virtual control
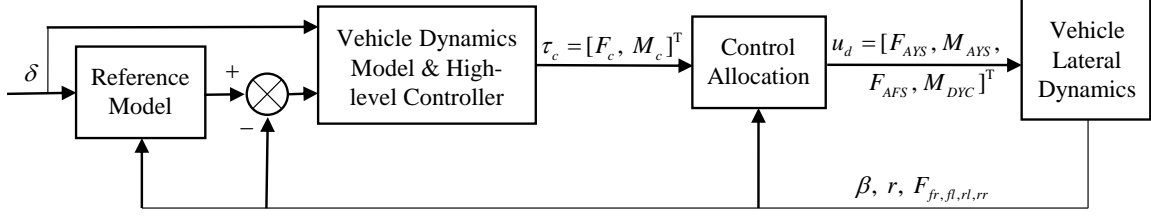
134

Figure 54. Hierarchical control architecture of over-actuated vehicle lateral dynamics.

τ_c. Thus, this control design is considered for an over-actuated system in which control allocation is necessary to distribute the high-level virtual control to the low-level real controls. In this section, the integration of AYS and AFS or DYC is considered to show the advantages brought by AYS when it works with AFS on low-μ road and with DYC on split-μ road.

Based on the control-oriented model of vehicle lateral dynamics (A.1), a nonlinear controller to track the references of vehicle states are designed based on Lyapunov theory, which is given by the following proposition.

Proposition A.2.1. *The following virtual control design $\tau_c = [F_c, M_c]^{\mathrm{T}}$ in (A.6) makes the tracking errors of two states in the system (A.1) asymptotically stable and the errors gradually go to zero.*

$$\tau_c = \begin{bmatrix} Mv_x & 0 \\ 0 & I_z \end{bmatrix} \left(\dot{x}_d + x_d - x - \begin{bmatrix} 0 & -1 \\ 0 & 0 \end{bmatrix} x - \begin{bmatrix} \frac{F_{fl}+F_{fr}+F_{rl}+F_{rr}}{Mv_x} \\ \frac{(F_{fl}+F_{fr})L_f-(F_{rl}+F_{rr})L_r}{I_z} \end{bmatrix} \right), \quad \text{(A.6)}$$

where $x_d = [\beta_d, r_d]^{\mathrm{T}}$, and the subscript $(\cdot)_d$ denotes the desired reference.

Proof. The proof of this proposition is omitted here for simplification since it follows the same method used in the proof of Proposition 4.5.1. $\square$

Based on the obtained high-level control design (A.6), the control allocation algorithm needs to be developed to distribute τ_c to low-level real controls. To incorporate all the applied vehicle lateral dynamics control together, namely AYS, DYC, and AFS, the relationship between the achievable values of τ_c from control allocation, τ, and the three real controls are developed as

$$\tau = \begin{bmatrix} F_c' \\ M_c' \end{bmatrix} = Su_d, \quad \text{(A.7)}$$

where

$$S = \begin{bmatrix} 1 & 0 & 1 & 0 \\ -l & 1 & L_f & 1 \end{bmatrix}, \quad \text{(A.8)}$$

135

and $u_d = \begin{bmatrix} F_{AYS} & M_{AYS} & F_{AFS} & M_{DYC} \end{bmatrix}^{\mathrm{T}}$, F_{AFS} denotes the corrective lateral force generated by AFS and M_{DYC} represents the corrective yaw moment generated by DYC. The relationship between the high-level control and the low-level control, through the control effectiveness matrix S, can be readily obtained for AFS and DYC. For the AYS, the relationship can be obtained from the dimension labeled in Fig. 51. Considering S has more columns than rows, infinite solutions theoretically exist for u_d to make τ close to τ_c. Therefore, the control allocation algorithm is designed to find the optimal solution u_d^* within all the solutions under constraints. The control allocation problem is formulated as

$$
\begin{aligned}
\min_{u_d} \quad & J = (\tau_c - \tau)^{\mathrm{T}} W_1 (\tau_c - \tau) + u_d^{\mathrm{T}} W_2 u_d \\
\text{s.t.} \quad & u_d \in U
\end{aligned}
, \tag{A.9}
$$

where J is the cost function, W_1 and W_2 are the weighting matrix, and U is the feasible region of u_d.

A.2.4 Simulation Results and Discussions

In this section, co-simulations integrating CarSim® with MATLAB/Simulink® are applied to verify the vehicle lateral dynamics control performance enhanced by the novel AYS system. In CarSim®, a B-class sports car with high-fidelity vehicle parameters, tire model and aerodynamic properties is selected as a simulation vehicle. The main vehicle parameter values in CarSim® are modified as shown in Table 5. The steering angle corresponding to a double lane change maneuver is commanded on a low-μ road and split-μ road simulation, respectively. Moreover, the rest of the components in simulation, including vehicle dynamics model, actuator models, and controller with control allocation, are all established in Simulink®. The reference signals of vehicle sideslip angle and yaw rate are obtained when the vehicle is driven on the consistent high-μ ($\mu = 1$) road, with keeping all other test conditions same.

Two cases are studied in this section. In the first case (low-μ road simulation), the tire-road friction coefficient μ is set as 0.5. The control performances are compared among the vehicle without control (as the baseline), the vehicle controlled by AFS, and the vehicle controlled by the integration of AFS and AYS. In the second case (split-μ road simulation), the tire-road friction coefficient μ is set as 0.3 on the right side and 0.85 on the left side. The control performances are compared with the vehicle without control (as the baseline), the vehicle controlled by DYC, and the vehicle controlled by the integration of DYC and AYS.

The simulation results of the first case are presented in Fig. 55, 56, 57. The sideslip angle and yaw rate response results are presented in Fig. 55. From Fig. 55, it is seen that the uncontrolled vehicle cannot track the sideslip angle and yaw rate references since the tire-road friction coefficient is reduced from 1 to 0.5. Similarly, the vehicle controlled by AFS also cannot track the references since the low-μ road
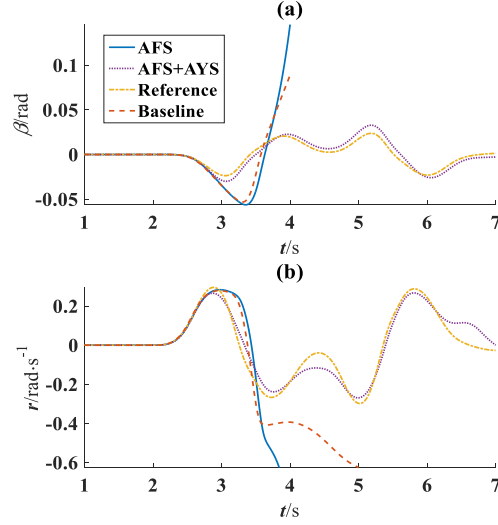
Figure 55. Side slip angle and yaw rate responses for a double lane change maneuver on the low-μ road.

condition does not support sufficient lateral friction forces production with respect to additional steering angles. However, the vehicle controlled by the integration of AFS and AYS can track the desired references to keep the lateral stability. This is because the proposed AYS introduces assisted corrective lateral forces and yaw moments, which are independent of road surface conditions. The simulation results display that the performance of AFS can be improved by introducing the AYS.

The control efforts of different control methods are shown in Fig. 56, where F_c' and M_c' are the control lateral force and yaw moment, respectively, provided by the AFS method in Fig. 56 (a) and the AFS+AYS method in Fig. 56 (b). From Fig. 56 (a), F_c' and M_c' generated by the AFS alone cannot satisfy F_c and M_c requirements from the high-level control. Therefore, AFS cannot provide reasonable control efforts to satisfy τ_c calculated from the high-level controller. The control efforts provided by the integration of AFS and AYS, however, follow the τ_c signal well, shown in Fig. 56 (b). That is because F_c' and M_c' produced by AYS is independent of road-tire interactions, and they can provide feasible additional corrective control efforts to help AFS achieve τ_c tracking. From the perspective of tire forces, contributions produced by AYS to F_c and M_c can help vehicle steering tires work in a linear stable region, as presented in Fig. 57. Thus, AYS helps AFS perform well through the introduction of additional F_{AYS} and M_{AYS} on the low-μ road.
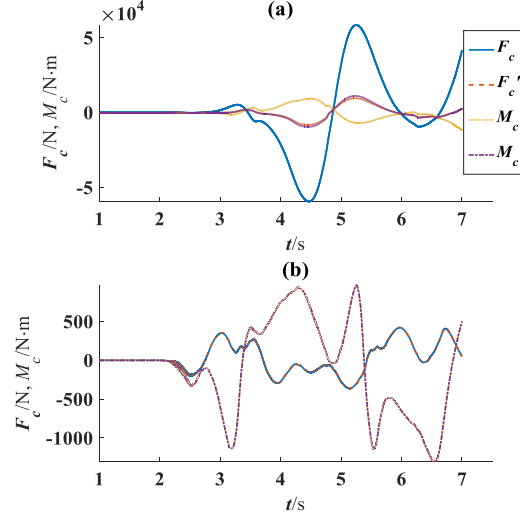
Figure 56. Virtual control tracking performance of the AFS and the AFS+AYS methods on the low-μ road.
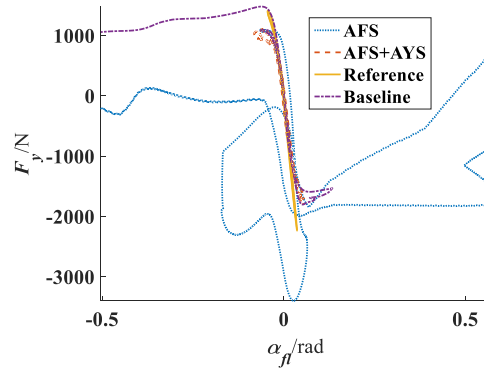

Figure 57. Front left tire lateral tire forces on the low-μ road.

The simulation results of the second case are presented in Fig. 58, 59, 60. The sideslip angle and yaw rate simulation results are presented in Fig. 58. From Fig. 58, the uncontrolled vehicle cannot track side slip angle and yaw rate references since the tire-road friction coefficient is changed from 1 to split-μ. Additionally, the vehicle controlled by DYC cannot track side slip angle and yaw rate references neither on the split-μ road. However, the vehicle controlled by the integration of DYC and AYS can track the references well, which means that AYS can help DYC improve vehicle lateral stability on the split-μ road.

The virtual control of different control methods is shown in Fig. 59. From Fig. 59 (a), it can be seen that although DYC follows the trend of M_c in τ_c, F_c is zero because DYC is based on the longitudinal friction force differences and cannot generate lateral forces. On the other hand, longitudinal tire friction forces cannot produce the required
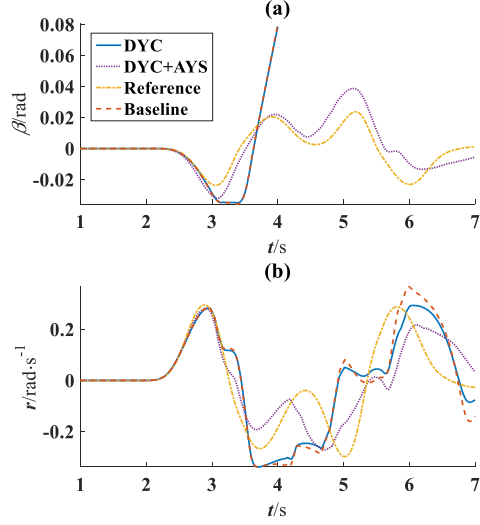
Figure 58. Side slip angle and yaw rate responses for a double lane change maneuver on the split-μ road.

corrective yaw moment due to the different friction coefficients between the left and right road surfaces. Similar to the analyses of the low-μ simulation, an additional F_{AYS} and M_{AYS} produced by AYS are independent of the road-tire interactions. This helps the control system provide large enough F_c and M_c to satisfy the virtual control requirements of high-level control design, as shown in Fig. 59 (b).

Fig. 60 presents the longitudinal forces $F_{xfl,xfr,xrl,xrr}$ of four tires with respect to wheel slip ratio κ, where the subscript $(\cdot)_{xfl,xfr,xrl,xrr}$ denotes front-left, front-right, rear-left, and rear-right tire, respectively. Fig. 60 also shows that the uncontrolled vehicle is not able to maintain a small κ for all four wheels, especially for two wheels driving on the low-μ side (right side). The same situation happens for the vehicle controlled by DYC. Thus, corrective yaw moment produced by DYC is not applicable and will not maintain vehicle lateral stability. However, for the vehicle controlled by the integration of AYS and DYC, all four wheels keep the small κ during the simulation.
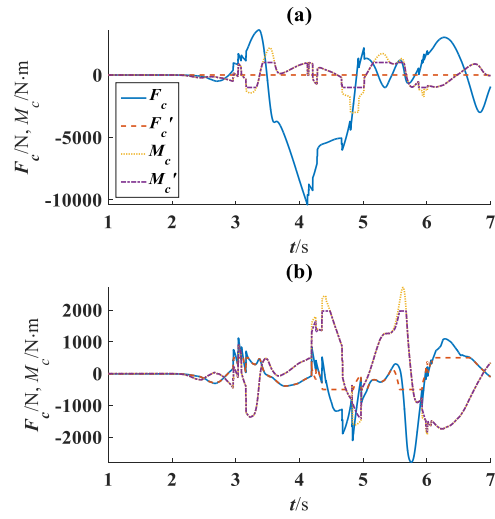
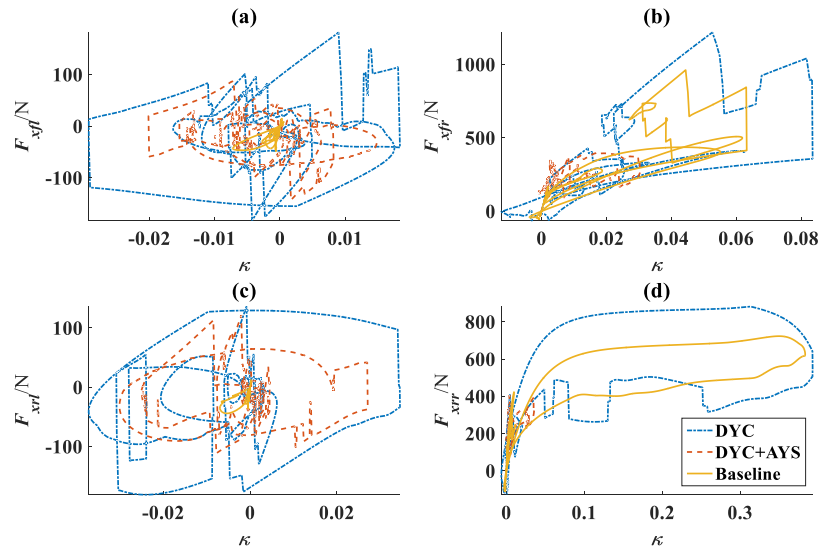Figure 59. Virtual control tracking performance of the DYC and the DYC+AYS methods on the split-μ road.

Figure 60. Longitudinal tire forces on the split-μ road.

A.2.5 Conclusions

The vehicle lateral dynamics stability is improved by using a novel AYS system and a corresponding control allocation algorithm design. On one hand, this proposed AYS has two degrees of freedom, which are exploited for corrective control efforts production. The AYS capability study shows that the corrective lateral force and yaw moment are as large as 380 N and 550 N · m. Thus, AYS can significantly complement and improve ASC or DYC performance without being affected by tire-road friction forces. On the other hand, AYS is integrated with the other vehicle lateral dynamics stability control methods—AFS or DYC. The simulation results demonstrate that AYS can effectively help AFS and DYC maintain vehicle lateral stability under critical driving conditions via independent assisted corrective lateral force and yaw moment.

A.3 Rollover Propensity Detection and Prevention

It is known that there is a higher risk of rollovers in vehicles with an increased height of the center of gravity (CG) and limited wheel track, such as sports utility vehicles, light trucks, and minivans. Statistically, nearly 33% of all traffic fatalities in car crashes result from rollovers (NHTSA's National Center for Statistics and Analysis 2016). In addition, in 2015, the annual percentage of fatalities in rollovers, 12.4%, increased most among various car crash types in the US (NHTSA's National Center for Statistics and Analysis 2016). Owing to such high fatalities of rollovers, the National Highway Traffic Safety Administration (NHTSA) launched rollover resistance ratings in the New Car Assessment Program (NCAP) from one star (the highest risk) to five stars (the lowest risk) to inform rollover risk (Rajamani 2006).

In recent years, electric anti-rollover technology emerges as a new vibrant research area to prevent rollover propensity. Generally, there are two classes of methods for anti-rollover in literature. The first category is passive warning-based systems (PWS) (Rajamani 2006). Within a PWS, the rollover propensity is detected or predicted throughout a rollover index (RI), and then a warning is provided to alert the driver to command corrective action. Powered by the advancement of onboard sensing and actuating technology, the other category is the active rollover prevention (ARP) systems, such as active steering control, differential braking, and active suspension (Yim 2011; Parida, Raha, and Ramani 2014; Goldman, El-Gindy, and Kulakowski 2001; Mashadi, Mokhtari-Alehashem, and Mostaghimi 2016). Triggered by a RI, an ARP system is able to automatically generate corrective control efforts to prevent the impending rollover. ARP techniques can be generally classified into two categories in literature, indirect and direct methods. The indirect approach is usually engaged with vehicle lateral or vertical dynamics control. For example, the rollover propensity was avoided by lateral acceleration mitigation through active steering control (ASC)

(Solmaz, Corless, and Shorten 2007) and differential braking (DB) (Yoon, Kim, and Yi 2007), or by adjusting vertical suspension forces through active or semi-active suspension technologies (Yim 2011; Parida, Raha, and Ramani 2014). One advantage of the indirect approach is that existing actuators for vehicle lateral and vertical dynamics control can be applied for roll motion control and no additional actuators are required. Two main issues, however, limit the application of indirect methods. On one hand, typical control effects through lateral acceleration mitigation and/or vertical suspension force adjustment tightly depend on the tire-road friction forces. The activated ARP, therefore, may not perform well when vehicles drive on the road with low or split friction coefficients. Additionally, when the tire lift-off (nearly) happens, which is a typical indicator for ARP activation (Yim 2011), the indirect approach may totally lose the rollover control capability since vertical loads and thus friction forces of lifted tires all become zero. On the other hand, few indirect methods can simultaneously maintain vehicle lateral performance and prevent vehicle rollovers. In the scenario with ARP activated, the control demands for lateral stability or ride comfort and those for rollover prevention may be contradictory. Thus, certain trade-offs between different vehicle dynamic performance are inevitable (Parida, Raha, and Ramani 2014; Yim, Park, and Yi 2010; Yoon et al. 2010).

Distinct from indirect methods, the direct approach resolves the rollover propensity independently without relying on tire vertical loads and friction forces. For instance, Mashadi et al. proposed a gyroscopic device to produce a corrective roll moment for the rollover prevention (Feng, Tan, and Tomizuka 1998). Similarly, Goodarzi et al. also tried to use a pendulum system to produce a moment to achieve the same control objective (Mashadi, Mokhtari-Alehashem, and Mostaghimi 2016). Nevertheless, one limitation of the existing direct methods is that the limited moving mass is mounted at a fixed position, which thus can only provide a limited corrective roll moment. Moreover, another limitation is that additional dedicated systems with relatively large dimensions are usually required and may not be feasible for the limited vehicle spaces. In other words, sufficient corrective roll moments for rollover prevention from an independent ARP system may be a heavy burden or even unachievable.

To overcome the aforementioned problems of existing ARP systems, the authors proposed a novel active rollover prevention method, called an active rollover preventer (ARPer). The ARPer, including a rotating motor and an orbit, locates at the back of the vehicle in the vertical plane, as shown in Fig. 61. The ARPer is inspired by the application of in-wheel motor technology, which can serve as the spare actuator/wheel of (hybrid) electric vehicles actuated by in-wheel motors (Chen and Wang 2013). This novel compact spare wheel configuration will have less dedicated space requirements. Moreover, the ARPer has two degrees of freedom (DOFs): moving along the orbit and self-rotating, which are driven by T_s and T_t, respectively. Both DOFs can introduce independent corrective roll moments without relying on tire-road friction forces. This section studies a novel vehicle rollover prevention control strategy by integrating the MCP metric with the ARPer to fully utilize its advantages. Once the rollover
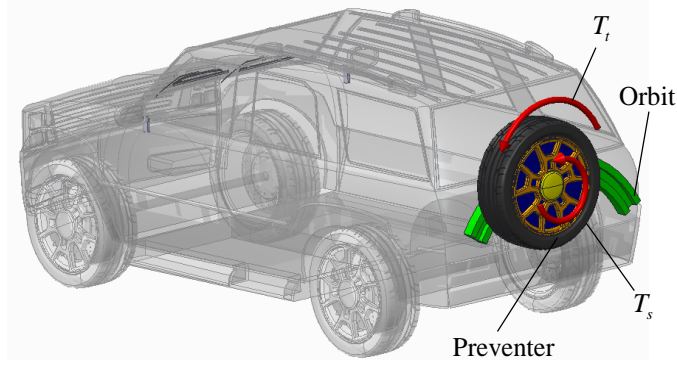
Figure 61. The schematic of the novel active rollover preventer system.

propensity is detected, continuous control efforts are determined through the MCP metric and applied through the proposed ARPer. In addition, a novel dynamic weighting method is employed to smooth chattering in control and vehicle states resulted from the strict ARPer activated threshold. Other contributions of this section also include the capability investigation of the ARPer subject to the limited vehicle space and driving torques.

A.3.1 Modeling of Vehicle Roll Dynamics with Active Rollover Preventer

The general schematic diagram of the vehicle roll dynamics model equipped with the ARPer is presented in Fig. 62. Since the roll dynamics is dominated in the impending rollover scenario, the vehicle in Fig. 62 is modeled as an inertial system for simplicity. Within Fig. 62, l_s is the vehicle track, h_c is the distance from the center of gravity (CG) to the center of roll (CR), h_s is the distance from the CG to the interaction point between the sprung mass and the unsprung mass, R is the radius of the orbit, l is the distance from the middle point of the orbit to the bottom of the sprung mass, z_s is the vertical translation of the sprung mass, φ is the roll angle of sprung mass, y_s is the lateral translation of the sprung mass, and ω_s and ω_t are the ARPer self-rotation angular speed and orbiting angular speed, respectively. Moreover, M is the vehicle sprung mass, g is the gravity acceleration, $F_{sl,sr}$ are two suspension forces and $\theta_{sl,sr}$ are suspension inclination angles, F_{cy} is the corrective lateral force, F_{cz} is the corrective vertical force, M_c is the corrective roll moment, and F_{lat} is the vehicle lateral force, which is described in (A.10),

$$F_{lat} = (M + m_u)(\ddot{y}_s + V_x r), \tag{A.10}$$

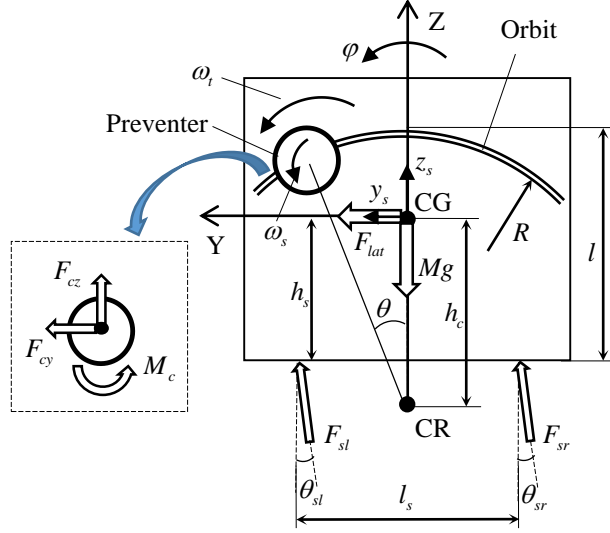where m_u is the unsprung mass.

143

Figure 62. Vehicle roll dynamic model with the active rollover preventer.

Considering F_{cy}, F_{cz} and M_c introduced by ARPer, the governing equations of the sprung mass are written in (A.11).

$$
\begin{cases}
M\ddot{z}_s = F_{sl}\cos\theta_{sl} + F_{sr}\cos\theta_{sr} - Mg + F_{cz} \\
M\ddot{y}_s = F_{sl}\sin\theta_{sl} + F_{sr}\sin\theta_{sr} - Mh_c\ddot{\varphi} + F_{cy} \\
(I_{xx} + Mh_c^2)\ddot{\varphi} = F_{lat}h_c\cos\varphi + Mgh_c\sin\varphi + \dfrac{l_s}{2}(F_{sr} - F_{sl}) \\
\qquad\qquad + (h_c + h_s)[F_{sr}\sin(\varphi - \theta_{sr}) + F_{sl}\sin(\varphi - \theta_{sl})] + M_c
\end{cases}
\tag{A.11}
$$

where I_{xx} is the moment of inertia of vehicle with respect to X axis, respectively. Within (A.11), F_{cy}, F_{cz} and M_c are determined in (A.12).

$$
\begin{cases}
F_{cy} = -ma_{sy} \\
F_{cz} = -ma_{sz} \\
M_c = -T_s + mR'(a_{sz}\sin\theta - a_{sy}\cos\theta)
\end{cases}
\tag{A.12}
$$

where m is the mass of the preventer, and θ is the orbiting angle between the orbit vertical central line and the line through CR and preventer. The reference position is defined as the intersection of the orbit and the vertical line passing the current CR. a_{sy} and a_{sz} are the equivalent lateral and vertical acceleration of the preventer, respectively, which will be further expanded in the following subsection. In addition, R' is the distance from the stabilizer to the current CR, which is determined in (A.13).

$$
R' = \sqrt{[l + h_c - h_s - R(1 - \cos\theta)]^2 + (R\sin\theta)^2}.
\tag{A.13}
$$

144

Remark A.3.1. Only the sprung mass is modeled in the vehicle rollover dynamics since the ARPer only interacts with the sprung mass directly. Moreover, for simplicity, the complex interaction or suspension forces between the sprung and unsprung mass are abstracted as two external forces by combining spring, damper, and suspension geometry forces together.

Considering the rolling of the sprung mass, three accelerations, including transport acceleration a_e, relative acceleration a_r, and Coriolis acceleration a_c, are involved in the preventer kinematics analysis under the global frame. The decompositions of these three accelerations are presented in Fig. 63. Within Fig. 63, γ is the orbiting angle between the orbit vertical central line and the line through the preventer and the orbit center; (a_{rt}, a_{rn}) and (a_{et}, a_{en}) are the tangential and normal decompositions of a_r and the rotational portion of a_e, respectively, and (a_{ex}, a_{ey}) is the orthogonal decompositions of the translational portion of a_e. Each acceleration decomposition is determined in (A.14).

$$
\begin{cases}
a_{ey} = \ddot{y}_s \\
a_{ez} = \ddot{z}_s \\
a_{et} = \ddot{\varphi} R' \\
a_{en} = \dot{\varphi}^2 R' \\
a_{rt} = \dot{\omega}_t R \\
a_{rn} = {\omega_t}^2 R \\
a_c = 2 \dot{\varphi} \omega_t R
\end{cases}
\quad , \tag{A.14}
$$

where $\dot{\omega}_t = T_t/J_{pt}$, and J_{pt} is the moment of inertia of the preventer with respect to the orbiting axle. Thus, a_{sy} and a_{sz} in (A.11) are described in (A.15) based on Fig. 63, and the corrective lateral force F_{cy}, vertical force F_{cz} and roll moment M_c introduced by the ARPer are obtained in (A.16) by substituting (A.14) and (A.15) into a_{sy} and a_{sz} in (A.11). Within (A.16), J_{pt} is the moment of inertia of the preventer with respect to the self-spinning axle.

$$
\begin{cases}
a_{sy} = a_{ey} + a_{et} \cos \gamma - a_{en} \sin \gamma - (a_{rn} + a_c) \sin \theta + a_{rt} \cos \theta \\
a_{sz} = a_{ez} - a_{et} \sin \gamma - a_{en} \cos \gamma - (a_{rn} + a_c) \cos \theta - a_{rt} \sin \theta
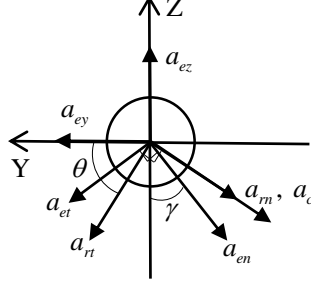\end{cases}
\quad . \tag{A.15}
$$

Figure 63. Decompositions of the preventer accelerations.

$$
\begin{cases}
F_{cy} = -m \left[\ddot{y}_s + \ddot{\varphi} R' \cos\gamma - \dot{\varphi}^2 R' \sin\gamma - (\omega_t{}^2 R + 2\dot{\varphi}\omega_t R)\sin\theta + \dot{\omega}_t R \cos\theta \right] \\
F_{cz} = -m \left[\ddot{z}_s - \ddot{\varphi} R' \sin\gamma - \dot{\varphi}^2 R' \cos\gamma - (\omega_t{}^2 R + 2\dot{\varphi}\omega_t R)\cos\theta - \dot{\omega}_t R \sin\theta \right] \\
M_c = -\dot{\omega}_s J_{ps} + mR' \left\{ \begin{bmatrix} \ddot{z}_s - \ddot{\varphi} R' \sin\gamma - \dot{\varphi}^2 R' \cos\gamma \\ -(\omega_t{}^2 R + 2\dot{\varphi}\omega_t R)\cos\theta - \dot{\omega}_t R \sin\theta \end{bmatrix} \sin\theta \right. \\
\qquad\qquad\qquad\quad \left. - \begin{bmatrix} \ddot{y}_s + \ddot{\varphi} R' \cos\gamma - \dot{\varphi}^2 R' \sin\gamma \\ -(\omega_t{}^2 R + 2\dot{\varphi}\omega_t R)\sin\theta + \dot{\omega}_t R \cos\theta \end{bmatrix} \cos\theta \right\}
\end{cases}
\tag{A.16}
$$

A.3.2 Mass-Center-Position Metric

A novel MCP metric is propped to provide provide the completed and continuous rollover information without saturation, even after tire lift-off. Using the MCP metric, both untripped and tripped rollovers are able to be detected via the estimation of the center of mass of vehicles. The general position vector of the CM of the vehicle system $\mathbf{r}_{sys}$ is written as the weighted average vector shown in (9).

$$
\mathbf{r}_{sys} = \begin{cases} \frac{M\mathbf{r}_s + m_u(\mathbf{r}_{ul} + \mathbf{r}_{ur})}{M + 2m_u} & \text{Before tire lift-off} \\ \frac{(M + m_u)\mathbf{r}_{Int} + m_u \mathbf{r}_u}{M + 2m_u} & \text{After Tire lift-off} \end{cases},
\tag{A.17}
$$

where $\mathbf{r}_s$ is position vector of the CM of the sprung mass, and $\mathbf{r}_{ul}$ and $\mathbf{r}_{ur}$ are two position vectors of the CM of unsprung masses for left and right sides, respectively; $\mathbf{r}_{Int}$ and $\mathbf{r}_u$ are the position vectors of the CM of the integrated mass and the unsprung mass without lift-off, respectively.

The MCP, represented as R_{sys}, is defined in the following equation,

$$R_{sys} = \begin{bmatrix} R_{sys\_y} \\ R_{sys\_z} \end{bmatrix} = \begin{bmatrix} \left([\mathbf{r}_{sys}]_{Y'-Z_l'} + [\mathbf{r}_{sys}]_{Y'-Z_r'}\right)_Y \\ \left(\frac{1}{2}[\mathbf{r}_{sys}]_{Y'-Z_l'} + [\mathbf{r}_{sys}]_{Y'-Z_r'}\right)_Z \end{bmatrix}, \qquad (A.18)$$

where $[\cdot]_{Y'-Z_l'}$ and $[\cdot]_{Y'-Z_r'}$ denote the vector coordinates under the frame $Y'-Z_l'$ and $Y'-Z_r'$. Different from the coordinate $Y-Z$ in Fig. 62, the frames $Y'-Z_l'$ and $Y'-Z_r'$ here are only used for the MCP estimation, which are fixed at the outer edges of the left and right side tire-ground contact patches, respectively. Adopting two different frames, $Y'-Z_l'$ and $Y'-Z_r'$, can help to keep the consistent manner of the MCP determination when either left-side or right-side rollover happens. Furthermore, $(\cdot)_Y$ and $(\cdot)_Z$ denote the lateral and vertical coordinate values of the vector, respectively. Physically, R_{sys_y}, the lateral coordinate value of R_{sys}, represents the lateral distance from the CM to the middle point of the vehicle track. A positive R_{sys_y} means the vehicle rolls to right side, otherwise the vehicle rolls to left side. Moreover, R_{sys_z} is the vertical coordinate value of R_{sys}, which represents the height of the CM.

For a driving vehicle, when one side tires (left or right) are lift-off or the rollover happens, the whole vehicle moment should be balanced with respect to the tire loads equivalent center of the contact patch, which is presented in (A.19) based on the d'Alembert principle. The d'Alembert principle, as a universal principle for dynamical system, can help to detect more rollover statuses in a dynamic manner, even vehicle jumping into the air.

$$\begin{cases} \Sigma_L \mathcal{M} = M \left[\ddot{R}_{sys\_y} R_{sys\_z} - \Delta_L(g - \ddot{R}_{sys\_z}) \right] \\ \Sigma_R \mathcal{M} = M \left[\ddot{R}_{sys\_y} R_{sys\_z} + \Delta_R(g - \ddot{R}_{sys\_z}) \right] \end{cases}, \qquad (A.19)$$

where $\Sigma_{L,r}\mathcal{M}$ denote the summations of left and right side moment balances, and Δ_L and Δ_R denote the distances from the estimated MCP to the left and right equivalent load center of the contact patch, respectively.

If tire lift-off on one side happens, either left or right side, only one equation in (A.19) will be satisfied. However, if both sides are lift-off, two equations in (A.19) are satisfied simultaneously, which implies vehicle rollover happening or vehicle jumping in the air. D'Alembert's principle, as a universal principle for the dynamic system, can help to detect more rollover statuses than those in literature, such as the aforementioned "vehicle jumping in the air". Moreover, the mass redistribution in vehicle dynamics resulted from tire lift-off does not influence the feasibility of D'Alembert's principle, which makes the MCP metric free of saturation.

Another new rollover status, called rollover threshold, could also be identified similarly from (A.19) based on the D'Alembert's principle. When the tire lift-off is detected by (A.19), the equivalent tire load center of the contact patch is assumed

at the middle point of the tire-road contact line in the roll plane. Because of tire deformation, when tires on one side are lift-off, the equivalent tire load center of the contact patch on the other side of the vehicle should move towards the outer edge of the tire if no effective prevention control is performed. In this situation, the rollover is going to happen immediately. This critical threshold, namely the equivalent tire load center moving from the middle point to the outer edge of the tire, is the most dangerous point before the rollover inevitably happens. In this case, the equivalent tire load center is assumed as the outer edge point of the tire-road contact line. Thus, $\Sigma_{L,r}\mathcal{M}$ and $\Delta_{L,R}$ should be updated as $\Sigma_{L,r}\mathcal{M}'$ and $\Delta'_{L,R}$, which are calculated similarly from (A.19) but the equivalent tire load centers are at left or right edges, respectively. To summarize, vehicle tire lift-off and rollover detection criteria are listed in Table 6. Several symbolic numbers in the last column are defined as indicators to represent different vehicle roll statuses in Table 6. These symbolic numbers are used to clearly represent the vehicle roll statuses in the simulation results for comparisons.

Table 6. Criteria for vehicle roll status detection

No.	Criteria	Roll Status Description	Indicator*
1	$\Sigma_L\mathcal{M} \neq 0$ and $\Sigma_R\mathcal{M} \neq 0$	Safe**	0
2	$\Sigma_L\mathcal{M} = 0$ and $\Sigma_R\mathcal{M} \neq 0$	Right side tire lift-off	+1
3	$\Sigma_L\mathcal{M} \neq 0$ and $\Sigma_R\mathcal{M} = 0$	Left side tire lift-off	−1
4	$\Sigma_L\mathcal{M}' = 0$ and $\Sigma_R\mathcal{M}' \neq 0$	Vehicle left side rollover threshold	+1.5
5	$\Sigma_L\mathcal{M}' \neq 0$ and $\Sigma_R\mathcal{M}' = 0$	Vehicle right side rollover threshold	−1.5
6	$\Sigma_L\mathcal{M}' = 0$ and $\Sigma_R\mathcal{M}' = 0$	One side rollover happening	±2
7	$\Sigma_{L,R}\mathcal{M} = 0$ and $\Sigma_{L,R}\mathcal{M}' = 0$	Vehicle jumping in the air	3

*: "±" represents the left-side rolling and right-side rolling, respectively.

**: it is also possible that vehicles are in the air if the criterion 7 satisfied in prior.

As implied in Table 6, criterion 7 represents the start or end of vehicle jumping in the air, which will not be held all the time during the vehicle in the air. That is because (A.19) is developed with respect to the tire-road contact patch defined by the frames $Y' - Z'_l$ and $Y' - Z'_r$ that are all fixed on the ground. Once the vehicle jumping in the air, the moment balance calculation will not represent the tire-road contact status. In this case, the moment balance values determined by (A.19) become non-zero, which are positively proportional to the vehicle jumping displacement with respect to the frames located on the ground. Therefore, criterion 1 also means the vehicle in the air if criterion 7 is satisfied in prior.

Remark A.3.2. For criterion 6, the vehicle rollover direction is decided by the rollover threshold in criterion 4 or 5 on which threshold is reached first. For example, the

vehicle is going to roll towards the left side when criterion 4 is first satisfied and then $\Sigma_R \mathcal{M}' = 0$ in criterion 6 is also reached. Moreover, the vehicle status of jumping in the air typically will not happen after the rollover. Thus, the vehicle jumping in the air should satisfy criterion 7 first and then satisfy criterion 1.

A.3.3   Evaluation of the Capability of Active Rollover Preventer

Based on pragmatic considerations, the capability of the novel ARPer system is investigated in this section under certain constrains of orbit dimension, preventer mass, and preventer driving torques. Specifically, three classes of variables can affect the capability of the ARPer system according to (A.16): geometry design parameters, driving torques, and vehicle states.

The geometry design parameters include R, m, l. Among these three parameters, R is the only parameter that can be largely varied, while the other two are all limited by vehicle physical spatial constrains. As the preventer driving torques, the maximum self-rotating T_s is assumed as large as 80 N · m, based on properties of an electric motor employed as an IWM [22]. Moreover, the tangential propulsion used to orbit the preventer is assumed as large as 100 N. Therefore, based on the mass of the preventer, 25 kg, the absolute tangential acceleration $\dot{\omega}_t$ along the orbit can reach 4 m/s^2. The self-rotating acceleration $\dot{\omega}_s$ is kept as zero for this evaluation because the effect of $\dot{\omega}_s$ could be simply considered by adding the maximum of T_s to M_c. Finally, vehicle states are varied for different driving maneuvers and speeds and also influenced by driving environments and vehicle design properties, such as road friction coefficient, vehicle mass, and dimension.

To evaluate the capability of the ARPer system, the open-loop simulations are conducted in CarSim$^{®}$ with an E-class SUV driving in a fishhook maneuver on the road with 0.85 road friction coefficient. The vehicle starting driving speed is 80 km/h. The steering wheel angle for the typical fishhook maneuver recommended in the NCAP. Physical vehicle spatial constraints and other vehicle parameters are summarized in Table 7. Within Table 7, max[l_w] and max[l_h] denotes the maximum orbit width and height. Given a certain value of R positive or negative constant $\dot{\omega}_t$ is commanded at different positions on the orbit. Then, the maximum absolute values of F_{cy}, F_{cz}, and M_c, denoted by max[$|F_{cy}|$], max[$|F_{cz}|$], and max[$|M_c|$], respectively, are obtained from the entire fishhook simulations. The results with respect to various R are presented in Fig. 64.

Table 7. Simulation variables and values in the ARPer capability study

Variable	Values
M	1590 kg
m_u	135 kg
m	25 kg
M	1,020 kg
I_{xx}	894.4 kg $\cdot$ m^2
max$[l_w]$	2 m
max$[l_h]$	1 m
l	1 m

The result presented in Fig. 64 for the corrective moment adds the maximum T_s in, 80 N $\cdot$ m. Intuitively, with the increasing of R, max$[||M_c||]$ also increases, while max$[||F_{cy}||]$ and max$[||F_{cz}||]$ decrease, where the minimum values of max$[||F_{cy}||]$ and max$[||F_{cz}||]$ approach 550 N and 200 N, respectively. Therefore, the ARPer system may not be able to prevent vehicle rollover independently due to the limited actuation and other vehicle physical spatial constrains. However, the ARPer system can still provide considerable complementation to the existing rollover prevention method. Considering the fact that the introduced corrective roll moment and forces are independent to tire-road friction forces, the ARPer system should offer significant supports for vehicle rollover prevention, especially after tire lift-off.

Remark A.3.3. The capability of the ARPer system may also be affected by the limited orbit constraints. When the preventer reaches two ends of the orbit, there is no orbiting movement to generate the corrective control efforts.

A.3.4 Controller Design

Based on the ARPer system capability investigation, the vehicle rollover prevention control could have a better performance to integrate the proposed ARPer system with some existing control methods, such as active front steering (AFS), which achieves rollover prevention through lateral acceleration mitigation. The overview of the control architecture of the vehicle rollover detection and prevention is presented in Fig. 65. Within Fig. 65, control efforts for rollover prevention through the dynamic weighting block provide adjustable control gains, which are aimed to resolve control chattering issues resulted from the ARP activated by a constant threshold.
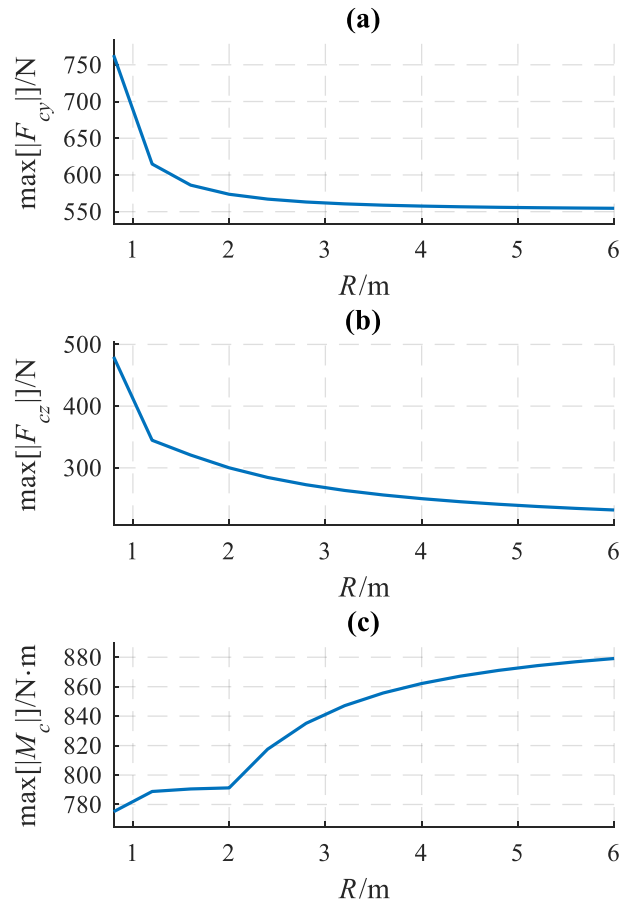
Figure 64. Active rollover preventer system capability evaluation results with respect to various orbit radii.
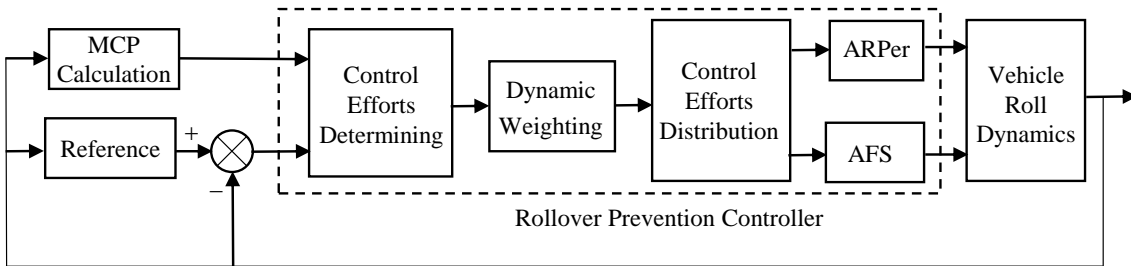

Figure 65. Control architecture for vehicle rollover detection and prevention with the ARPer.

According to Table 6, it is anticipated that both $\Sigma_L \mathcal{M} \neq 0$ and $\Sigma_R \mathcal{M} \neq 0$ are satisfied to mitigate vehicle rollover propensity. Therefore, assuming that the vehicle mass center does not move, the desired vehicle roll statuses, denoted as $\Sigma_L \mathcal{M}_0$ and $\Sigma_R \mathcal{M}_0$, are obtained in (A.20) by substituting zero accelerations of the MCP into (A.19).

$$
\begin{cases}
\Sigma_L \mathcal{M}_0 = -\Delta_L (M + 2m_u)g \\
\Sigma_R \mathcal{M}_0 = -\Delta_R (M + 2m_u)g
\end{cases}
. \tag{A.20}
$$

When $\Sigma_L \mathcal{M}_0$ and $\Sigma_R \mathcal{M}_0$ are achieved when the vehicle mass center moves, the desired acceleration value of the MCP, denoted as $[\ddot{R}_{sys}]_d$, is determined in (A.21) by using (A.20).

$$
[\ddot{R}_{sys}]_d = \begin{bmatrix} (\ddot{R}_{sys\_y})_d \\ (\ddot{R}_{sys\_z})_d \end{bmatrix} = \begin{bmatrix} R_{sys\_z} & \Delta_L \\ R_{sys\_z} & -\Delta_R \end{bmatrix}^{-1} \begin{bmatrix} \frac{\Sigma_L \mathcal{M}_0}{M+2m_u} + g\Delta_L \\ \frac{\Sigma_R \mathcal{M}_0}{M+2m_u} - g\Delta_R \end{bmatrix}. \tag{A.21}
$$

Given $[\ddot{R}_{sys}]_d$, a nonlinear controller for tracking the references is designed based on the Lyapunov theory. The nonlinear controller is given by the following proposition.

Proposition A.3.1. *Control inputs* $u = [F_{cy}, F_{cz}]^T$ *in the following equation will achieve asymptotic tracking on the given reference in (A.21) and prevent vehicle impending rollover.*

$$
u = (M + 2m_u)\left([\ddot{R}_{sys}]_d + [\dot{R}_{sys}]_d - \dot{R}_{sys}\right). \tag{A.22}
$$

Proof. The proof of this proposition is omitted here for simplification since it follows the same method used in the proof of Proposition 4.5.1. □

A constant rollover index threshold is usually required to trigger the ARP control. Nevertheless, the ARP control may be turned on and off frequently due to some aggressive vehicle driving maneuvers, such as a fishhook with relatively high speed. Frequently enabling and disabling the ARP control not only provide discontinuous control efforts but also cause unnecessary chattering of roll states. Thus, in order to avoid the chattering of control efforts and roll states caused by the ARP control frequent switching, a dynamic weighting is applied to smooth the control efforts. The design of dynamic weighting function, shown in (A.23), is based on an upper normal distribution function and values of the lateral load transfer ratio (LTR) for tire lift-off detection. The LTR is a prevalent dynamic RI defined by the difference of vertical tire loads between the left and right sides, which is constrained from -1 to 1 by tire lift-off.

$$
w(|LTR|) = \begin{cases} 0 & |LTR| \leq \xi \\ 1 - \exp{-(\frac{|LTR|-\xi}{\sigma})^2} & |LTR| > \xi \end{cases}, \tag{A.23}
$$

where σ and ξ two small constants. Using (A.23), the rollover prevention control can work through a continuous weighting function, instead of a constant threshold, and chattering is also mitigated.
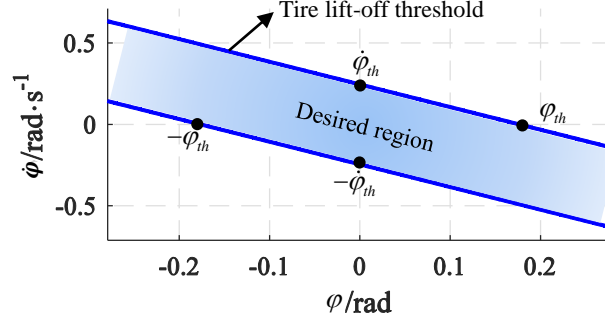
Figure 66. Stable region in the phase portrait of roll angles.

A.3.5　Simulation Results and Discussions

In this section, co-simulation between CarSim® and MATLAB/Simulink® is used to demonstrate the vehicle rollover prevention performance enhanced by the novel ARPer system. In CarSim®, the same E-class SUV and fishhook maneuver as those utilized in ARPer capability study are applied in simulations. Based on the capability study, the orbit radius R is selected at 3 m to make trade-offs among $\max[\|F_{cy}\|]$, $\max[\|F_{cz}\|]$, and $\max[\|M_c\|]$. Moreover, all simulations have an initial entrance speed at 46 km/h and are on the road with a 0.85 friction coefficient. The ARPer system is assumed to be mounted at the rear of the SUV as shown in Fig. 61. Furthermore, this SUV is also equipped with a roof cargo box to raise the CG position. Keeping all the aforementioned conditions the same, when the mass of the roof cargo box increases to 250 kg, the LTR result shows that the uncontrolled vehicle rolls over. Thus, a 250 kg roof cargo box is added to obtain the baseline of the rollover vehicle without control.

To further compare and evaluate the control performance, a roll angle phase portrait is also used. In the phase portrait of roll angles, a desired region for the vehicle roll motion is defined in Fig. 66, based on the tire lift-off threshold. Within Fig. 66, the thresholds of $\dot{\varphi}$ and φ lie on two straight lines at zeros. The corresponding intersections, denoted by $\dot{\varphi}_{th}$ and φ_{th}, are defined in (A.24).

$$\begin{cases} \dot{\varphi}_{th} = \frac{Mgl_s}{c_{\mathrm{roll}}} & \varphi = 0 \\ \varphi_{th} = \arctan(\frac{m_u l_s}{Mh_c}) & \dot{\varphi} = 0 \end{cases}, \tag{A.24}$$

where c_{roll} is the roll damping, which is set as 100 kN/rad.

Remark A.3.4. The tire lift-up of different wheels may not happen simultaneously in practice. Hence, the average values of tire forces and unsprung masses states of front and rear wheels are used in the simulations.
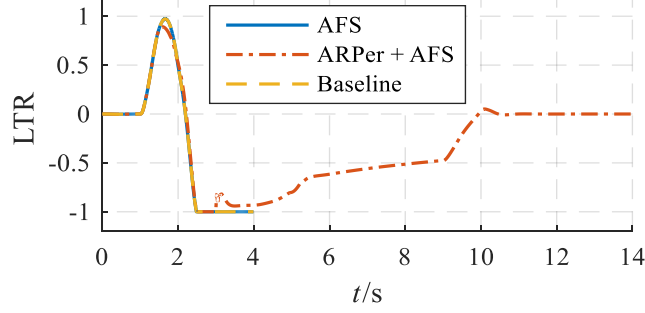
Figure 67. LTR responses for rollover prevention control.

The simulation results of the LTR, the moment balance, and the roll angle phase portrait are presented in Fig. 67, 68, and 69. Within Fig. 67, 68, and 69, the baseline is the uncontrolled vehicle with a 250 kg roof cargo box.

From Fig. 67 and 68, due to zero steering angle at the beginning of simulations, LTR keeps at zero, and $\Sigma_L \mathcal{M}$ and $\Sigma_R \mathcal{M}$ are the same as $\Sigma_L \mathcal{M}_0$ and $\Sigma_R \mathcal{M}_0$, respectively. With the increasing of steering angle, $\Sigma_L \mathcal{M}$ and $\Sigma_R \mathcal{M}$ start to depart from their desired values, and LTR also simultaneously increases close to 1, which indicates that rollover is going to happen. Then, for baseline and vehicle controlled only by AFS, simulations stop around 4 seconds since vehicle rollovers are not prevented successfully. However, vehicle controlled by both AFS and ARPer can go through the whole simulation and $\Sigma_L \mathcal{M}$, $\Sigma_R \mathcal{M}$ and LTR finally can come back to their desired values. Thus, it is demonstrated that with the assistance of the ARPer, the total vehicle ability for rollover prevention is improved. From the roll angle phase portrait, shown in Fig. 69, neither baseline nor vehicle controlled by AFS can keep roll angles trajectories within the desired region. Again, vehicle controlled by both AFS and the ARPer can achieve that.

Front tire lateral forces, presented in Fig. 70, can explain more on the working principle of the ARPer. Within Fig. 70, F_{yfl} and F_{yfr} denote front left and right tire forces, respectively. From Fig. 70 (a), before rollover happens, F_{yfr} in the case of AFS control is zero since the right-side tires are lifted off. Consequently, AFS fails to provide enough lateral forces for rollover prevention. In Fig. 70 (b), both F_{yfl} and F_{yfr} do not become zero, because the ARPer prevents rollover by offering significant
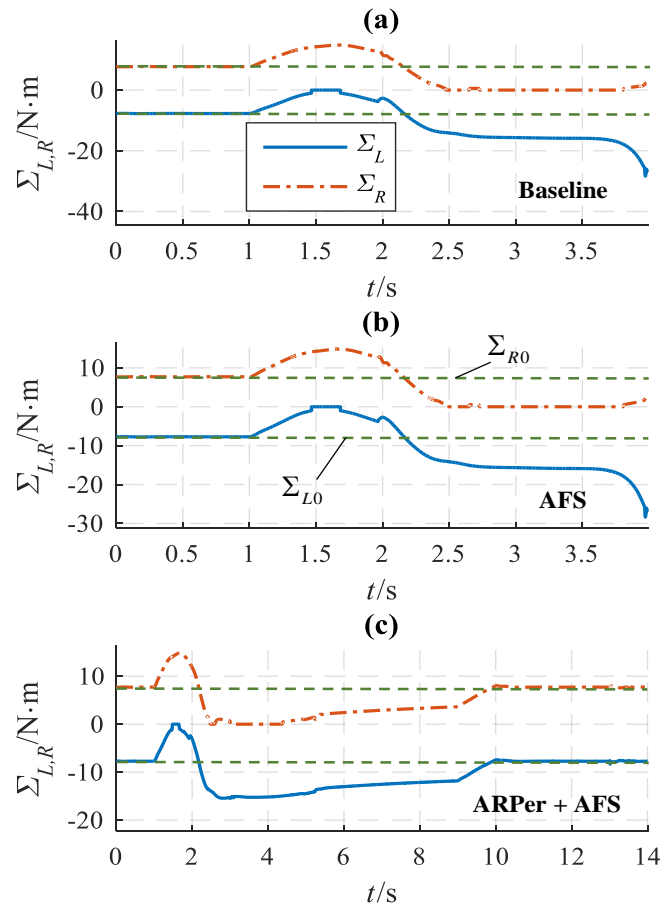
154

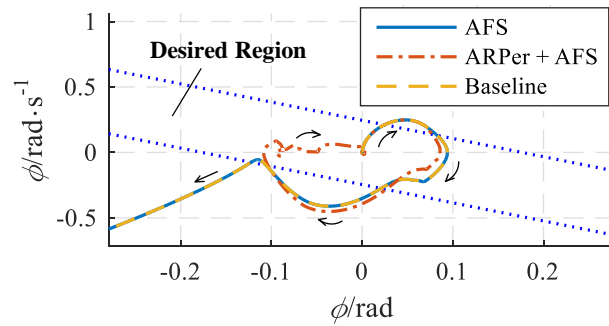Figure 68. Responses of moment balances.

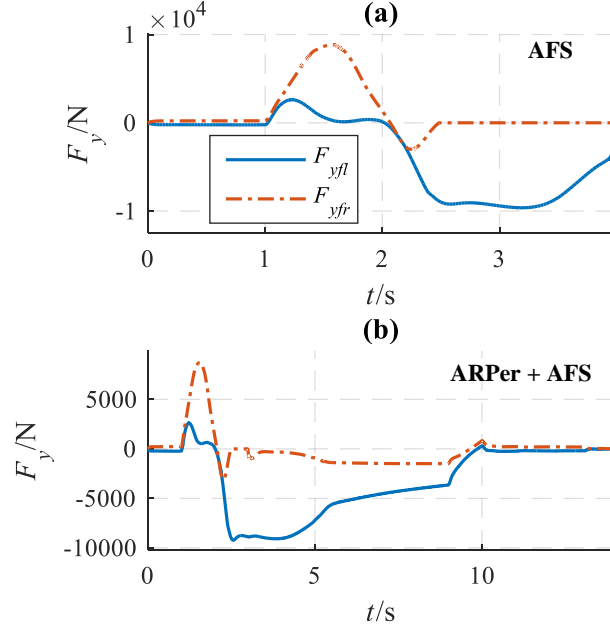Figure 69. Roll angle phase portrait.

155

Figure 70. Lateral tire force responses for rollover prevention control.

control efforts, including lateral forces, without being affected by tire lift-off. On the other hand, non-zero lateral tire forces feedback also helps AFS to perform better.

Since the ARPer system is mounted at the rear of the SUV, an additional yaw moment is introduced, and the yaw stability may be affected. Nevertheless, the ARPer system is not trigged until the impending hazardous rollover is detected. Since the ARPer system does not work all the time, it has limited influences on yaw stability.

A.3.6   Conclusions

This section proposes a novel vehicle rollover prevention methodology by utilizing the ARPer. Demonstrated by the fishhook maneuver through the co-simulation between CarSim® and MATLAB/Simulink®, three conclusions are summarized. First, the ARPer capability study shows that the corrective control efforts generated by the preventer can provide significant complementation for vehicle rollover prevention. Second, the integration of the MCP metric and the ARPer can successfully complete rollover detection and prevention through continuous roll motion information without saturated by tire lift-off. Third, the ARPer can not only successfully assist AFS to prevent the rollover propensity, but also be robust to tire-road contact situations, even when tires are lifted off.

BIOGRAPHICAL SKETCH

Fengchen Wang was born in Xuancheng, China, on November 1991. He received his B.S. and M.S. degree (with honors) in automotive engineering from China Agricultural University, Beijing, China, in 2014 and 2016, respectively. In August 2016, he entered the Polytechnic School at Arizona State University to pursuit the Ph.D. degree in systems engineering. Meanwhile, he has been a graduate research associate with the Dynamic Systems and Control Laboratory, Arizona State University, Mesa, USA. His research interests include vehicle dynamics and control, automated vehicle technology, and vehicular cyber-physical system. Mr. Wang is the author or co-author of more than 20 peer-reviewed publications. He was also a recipient of the University Graduate Completion Fellowship, the University Graduate Block Fellowship, the National Scholarship, and Beijing Outstanding Graduate.